UNIVERSITY OF CALIFORNIA IRVINE

Nonlinear Microscopy with Surface Plasmon Polaritons

THESIS

submitted in partial satisfaction of the requirements

for the degree of

Doctor of Philosophy

in Chemical and Materials Physics

by

John Kenison

THESIS COMMITTEE:

PROFESSOR ERIC O. POTMA, CHAIR

PROFESSOR MICHELLE DIGMAN

PROFESSOR WILSON HO

2018

Contents

List of Figures

Curriculum Vitae

EDUCATION

University of California, Irvine — December 2018
Ph.D., Physics

California State University, East Bay — June 2008
M.S., Mathematics

University of California, Santa Barbara — September 2004
B.S. Mathematics

RESEARCH EXPERIENCE

University of California, Irvine — Jan 2016-Dec 2018
Potma Lab

PUBLICATIONS

- Kenison, J. P., Fast, A., Matthews, B. M., Corn, R. M., & Potma, E. O. (2018). Particle sensing with confined optical field enhanced fluorescence emission (Cofefe). Optics express, 26(10), 12959-12969.
- Kenison, J. P., Fast, A., Guo, F., LeBon, A., Jiang, W., & Potma, E. O. (2017). Imaging properties of surface-enhanced coherent anti-Stokes Raman scattering microscopy on thin gold films. JOSA B, 34(10), 2104-2114.
- Fast, A., Kenison, J. P., Syme, C. D., & Potma, E. O. (2016). Surface-enhanced coherent antiStokes Raman imaging of lipids. Applied optics, 55(22), 5994-6000.
- Feinblum, D. V., Kenison, J., & Burke, K. (2014). Communication: Testing and using the LewinLieb bounds in density functional theory.

WORK EXPERIENCE

- Graduate Student Researcher/ Teaching Asssistant — June 2014-Dec 2018

University of California, Irvine

- Adjunct Math Instructor — January 2010-June 2014

Cabrillo College/ Monterey Peninsula College
Aptos, CA

- Math Instructor — June 2009-September 2009

United States Coast Guard
USCGC Sherman

ABSTRACT OF THE DISSERTATION

Nonlinear Microscopy with Surface Plasmon Polaritons

By

John Kenison

Doctor of Philosophy, Physics

University of California Irvine, 2018

Professor Eric Potma , Chair

Nonlinear light-matter interactions have been key to advances in biological imaging and sensing. Naturally, customized light fields have been deployed to draw out and target these nonlinear phenomenon. In the case of Surface Plasmon Polaritons, electro-magnetic fields are confined to a nearly two dimensional region on a supporting metallic thin film. Here we explore consequences and applications of using gold films to support these propagating surface modes. The presence of sub-μm-sized particles in the excitation area distorts and confines the surface field, resulting in nonlinear electron-hole pair generation in the gold followed by radiative recombination. This mechanism, in which the gold film is both the source of strong near-fields as well as the antenna for coupling radiation to the far-field, holds promise as a label-free sensing mechanism of small particles near the surface. In addition, the ability to simultaneously support multiple SPP fields with well defined momenta allows for an unconventional method of generating four-wave mixing signals at the film surface. SPP mediated coherent anti-Stokes Raman scatterig (CARS) signals from biological samples are demonstrated, revealing unconventional imaging properties.

Chapter 1

Introduction

1.1 Label Free Microscopy

Early uses of light fields in microscopy represented a minimally invasive probe for examining biological samples. Variations in light propagation within a sample, due to refractive changes, provided a spatial contrast representative of the structure of the sample. The first advances in microscopy centered around the ability to bring this response from the micro scale to a visually perceptible range through various lens systems.

The early twentieth century benefited from a more sophisticated model of the probing light fields as electromagnetic waves. Phase contrast microscopes were developed to exploit minute variations of the phase component of propagating waves, induced even by transparent samples, generating a contrast mechanism by controlling conditions for constructive interference. Employing the polarization dependent propagation of light through birefringent materials resulted in microscopes with the ability to view complex biological processes in real time. (Inoue', 1953),(Schmidt, 1939) The inherent birefringence of cellular spindle fibers illuminated their structure as well as their morphological changes during mitosis, demonstrating that previous

observations of spindles were not an artifact of cell staining. Polarization, and phase contrast microscopes benefit from an optical interaction that can be characterized by the intrinsic refractive properties of the sample.

Predictions of increased resolution with shorter wavelength excitation resulted in the development of the UV microscope by August Kohler in 1904, nearly doubling the resolution possible with white light. Observations of red shifted luminescence under UV excitation, however, required understanding of new interaction mechanisms. Early fluorescence microscopes utilized the autofluorescence of cells and bacteria to produce a red shifted signal derived from an interaction with intrinsic electronic properties of the sample. The use of fluorescent labels along with the development of coherent light sources gave rise to a dramatic series of advances in microscopy. Scanning confocal microscopes became practical fluorescence imaging tools with the incorporation of laser illumination, revealing clear images within tissue and opening up the possibility of *in vivo* biological imaging. The intense peak fields introduced by pulsed lasers made nonlinear signal generation possible, with two-photon excited fluorescence as an early example of nonlinear optical microscopy. The ability to confine the fluorescence response to a localized focal volume, where the excitation field intensity is drastically enhanced, lead to the ability to view living cells buried deep within living tissue with greatly reduced out of focus contributions. Distinct from previous modalities, fluorescence techniques made use of a light field generated at the location of the sample. The associated advantages afforded to fluorescence have inspired efforts to produce label free imaging techniques with comparable properties. Often these efforts begin with customized light fields that optimize specific interactions.

1.2 Surface Plasmon Polaritons

Surface Plasmon Polaritons (SPP's) are formed through a light-matter interaction, coupling collective electron oscillations at a metallic surface to a propagating electromagnetic wave in an adjacent dielectric medium. Upon coupling freely propagating radiation to the SPP mode, the incident radiation is converted to an elliptically polarized plane wave that decays exponentially away from the metal/dielectric interface ($\sim$200nm).

The utility of evanescent fields as a probe field for investigating biological systems at surfaces has been realized with total internal reflection fluorescence (TIRF) microscopy, where the supporting surface of relevance is formed by a glass/water interface. Imaging of cell membranes adhered to a glass coverslip was achieved over a wide field of view by exciting fluorescent labels and avoiding out of focus contributions from the sample bulk (Axelrod, 1981). While geometrically similar to a TIRF microscope configuration, the addition of an SPP supporting gold film produces additional enhancement of the evanescent fields. For uniform layered planar media, this requires precise momentum matching between the in-plane component of a p-polarized light field and the associated out of plane electron oscillation of the same energy.

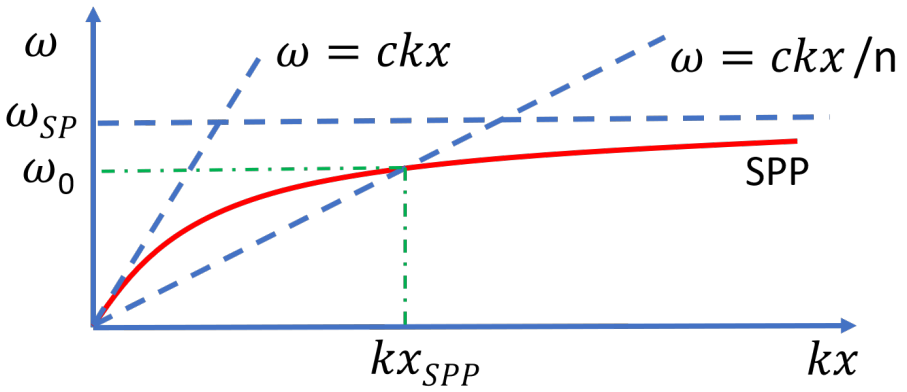

FIGURE 1.1: SPP dispersion curve

For a given frequency, a freely propagating beam has insufficient momenta to excite an SPP. A strategy for overcoming this obstacle is to use the evanescent field generated beyond the critical angle at a planar interface as a driving field. The in-plane component of the evanescent field is greater than the corresponding propagating beam in the second half space, and is capable of driving SPP's at a near-by interface(Green et al., 2000; Zayats, Smolyaninov, and Maradudin, 2005). This mechanism is employed in both Kretschmann and Otto configurations.

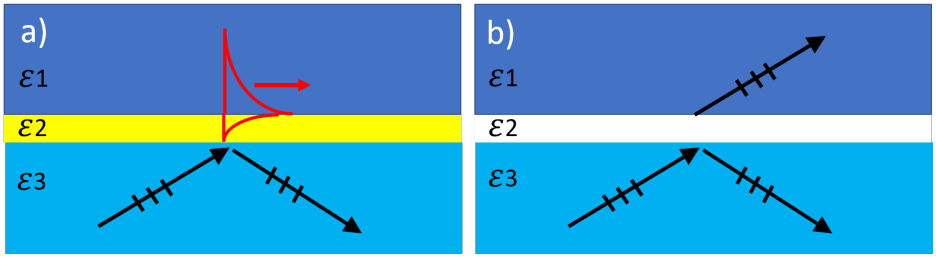

FIGURE 1.2: Three layered system. From bottom to top, the layers are glass/gold/air. In a Kretschmann configuration, light is incident from the glass side at the angle of incidence corresponding to SPP resonance.

In the case of a Kretschmann configuration, we can imagine a three layer system. A

thin gold film is sandwiched by a glass layer in the form of a prism or objective lens along with an opposing dielectric halfspace, typically water. Solutions to Maxwell's equations in the illuminated area of the film must satisfy boundary conditions at two closely spaced interfaces of the film with the surrounding environment. Beyond the critical angle for a glass-gold interface, the resulting evanescent field can have sufficient momenta along the interface to support SPP oscillations in the gold-dielectric boundary. When the incident beam is tuned to the Kretschmann angle, a noticeable decrease in the reflectance of the illuminated gold film is observed as energy is coupled into SPP modes.

Surface plasmon polaritons also have the ability to redirect near-field radiation to the far-field. The ability for an evanescent wave to couple to freely propagating modes is not unfamiliar even without the presence of plasmonic effects. Replacement of the gold film with an air gap allows for frustrated total internal reflection where evanescent fields at the 2-3 interface penetrate the 1-2 interface and emerge as freely propagating waves in medium 1. This optical tunneling effect forms the basis for leakage radiation (Hohenau et al., 2011), where evanescent fields associated with SPP waves extend into and through the metal side of the interface. This provides a far-field radiative channel for SPP waves propagating on a metallic film thin enough to allow an optical tunneling effect to occur. In the bottom half space, a freely propagating wave at the Kretschmann angle emerges and can be collected by a high NA objective. Surface plasmon coupled emission microscopy (SPCEM) relies on the coupling of the large momenta of evanescent fields from excited fluorophores near the metallic interface to propagating SPP modes. The resulting SPP fields radiate symmetrically on the gold film, emitting leakage radiation as they travel outward from the source. This illustrates the ability of a thin gold film to not only support an SPP excitation field but also act as a near field antenna. Gold

films used for this purpose may benefit from a thinner film than what is typically used in SPR imaging applications (45 nm)(Chiu et al., 2011). Efficient excitation of SPP modes in a Kretschmann geometry is more of a concern in the latter while a decreased barrier for radiation generated near the interface must also be considered in the former. The ability for the gold film to fulfill these roles is critically dependent on its thickness and surface quality.

1.3 Gold Thin Films

Theoretical descriptions of SPP's often involve an idealized representation of the metallic films that support them. Typically, film's surface is described as a perfectly smooth infinite plane of arbitrary constant thickness containing a free electron gas. In reality, specific film deposition methods impose distinct deviations from uniformity. The band structure of the metal layer is also an important factor in describing optical properties of the film which extend beyond an electron gas model.

Thin metal films stand at the boundary between familiar bulk metallic properties and an ultra thin regime where the optical and electrical properties become highly dependent on the geometry of the film, and its inhomogeneities. Many optical properties of bulk metals can be attributed to a large density of electrons which are nearly free to move throughout the interior of the metal. The responsiveness of these charges to electromagnetic fields near the surface allows efficient re-radiation of incident light, resulting in highly reflective surfaces as incident fields decay rapidly in the metal due to losses in the material. As the thickness of a bulk metal slab decreases to length scales comparable to the skin depth of the metal (25nm for gold in near and mid IR,(Olmon et al., 2012)), the film becomes increasingly transparent as exponentially decaying fields generated at the incident face are able to reemerge

as propagating waves on the opposing side. Gold films transmitting a noticeable amount of light are less than 40 nm. The penetration depth of 1000nm light is about 13 nm while 500nm light has a penetration depth of 70nm (Loebich, 1972). This notion led to early use of gold films as a cold-coating for plate glass windows, as it reflects heat from IR wavelengths while transmitting visible light.

Observations of photoluminescence from gold films under visible illumination point to optical properties that cannot be attributed to a free electron model.(Mooradian, 1969) The broad spectrum observed does not depend on excitation wavelength, suggesting a recombination of holes and electrons via interband transition between the d-valence band and sp-conduction band of gold.(Beversluis, Bouhelier, and Novotny, 2003) The X and L symmetry points in the Brillouin zone of bulk gold show a high density of states, facilitating transitions from the d band to the sp-conduction band. Energies of 1.8 eV and 2.4 eV respectively separate d holes from the Fermi surface. (Beversluis, Bouhelier, and Novotny, 2003) For near-IR sources (780nm), the surface morphology of the gold film has a strong effect on the observed spectrum, as only roughened films show a strong visible emission from two photon absorption.(Boyd, Lu, and Shen, 1986)

In the regime of negligible photon momentum, interband transition rules place constrictions on electron hole recombination that translate to inefficient emission. The efficiency of these transitions increases as photon modes of greater momenta are introduced, providing a mechanism for momentum matching additional electron-hole pairs. Modes of sufficient momentum to allow efficient two photon absorption require enhanced and spatially confined fields generated by inhomogeneities in the gold film. The range of potential sources for this film inhomogeneity naturally appeals to sensing applications, and while wide field illumination of a gold film with SPP's is not uncommon, the visible two photon fluorescence of the film itself as an

indicator of the presence of surface bound analytes has not been fully utilized.

1.4 Cofefe

Interferometric sensors have a wide range of applications, but their utility is ultimately limited by a detectable interference against a large background of the light field. An alternative strategy is the surface plasmon resonance (SPR) sensor, a refractometer that senses minute changes in the refractive index by monitoring variations in the coupling angle of a propagating light field to a surface plasmon polariton wave supported by a metal film.(Homola, 2008; Matsubara, Kawata, and Minami, 1988; Zhang and Uttamchandani, 1988) This class of refractive sensors benefits from the unique properties of surface plasmon waves at metal-dielectric interfaces, which display exquisite sensitivity to small refractive changes in the immediate vicinity of the interface. SPR sensors do not require interferometric stability, which makes this approach robust and relatively simple. The fact that the technology has been commercialized by several manufacturers, including GE Healthcare Life Sciences (Biacore), Pioneer and Conductive Technologies, is testament to the reliability of the SPR approach. SPR biosensors have been used in a wide area of applications,(Homola, 2008; Boozer et al., 2006; Phillips and Cheng, 2007; Homola, Yee, and Gauglitz, 1999), ranging from detection of pathogens, toxins, pesticides, drugs, allergy markers, cancer markers, antibodies and more. As such, SPR based technologies have impacted the fields of medical diagnostics, food safety and environmental monitoring.

Recent developments have shown the utility of spatially resolving the SPR response,

offering the possibility to probe many individual binding/detection events simultaneously.(Jordan et al., 1997; Brockman, Nelson, and Corn, 2000) Because SPR imaging (SPRI) devices are essentially multiplexed sensors, they enable high throughput detection of target analytes at high speed. When adopted into a microscope, the SPRI signal can also be obtained as an image with a high numerical objective lens, providing a high-resolution assessment of binding and adsorption events near the metal surface.(Huang, Yu, and Zare, 2007; Kano and Knoll, 2000; Weichert et al., 2010) The SPRI microscopy technology has been successfully used to probe cells(Wang et al., 2012), bacteria and viruses(Syal et al., 2015; Wang et al., 2010), DNA(Yu et al., 2014; Halpern et al., 2014), protein structures(Maley et al., 2017), to name just a few.

Despite the attractive sensing capabilities of SPRI microscopes, their high potential for multiplexed detection is somewhat overshadowed by the compromised spatial resolution of the device. The pointspread function of the SPR imaging system shows wide diffractive tails, making a nanoscopic binding/adsorption event appear as a feature that extends over tens of micrometers. Because of the extended pointspread function, spatially separated events may show up as overlapping and interfering features, complicating their individual identification. To increase the spatial resolution, special algorithms have been developed that improve the performance of the SPRI device, achieving an effective resolution on the sub-micrometer scale.(Yu et al., 2017) Nonetheless, the restored pointspread function is non-symmetric and exhibits unpredictable flares. Hence, a high-resolution alternative to SPRI would enable more confident detection of multiple proximal events, improving the throughput and utility of the device.

This has inspired the development of a new type of optical sensor suitable for registering the binding/dissociation of nanoscopic particles near a gold sensing surface. The method shares similarities with surface plasmon resonance microscopy but uses a completely different optical signature for reading out binding events. This new optical read-out mechanism, called confined optical field enhanced fluorescence emission (Cofefe), uses pulsed surface plasmon polariton fields at the gold/liquid interface that give rise to confined optical fields upon binding of the target particle to the gold surface. The confined near-fields are sufficient to induce two-photon absorption in the gold sensor surface near the binding site. Subsequent radiative recombination of the electron-hole pairs in the gold produces fluorescence emission, which can be captured by a camera in the far-field. Bound nanoparticles show up as bright confined spots against a dark background on the camera. The Cofefe sensor is capable of detecting gold and silicon nanoparticles, as well as polymer nanospheres and lipid droplets in a label-free manner. In this thesis, a sensor based on Cofefe is demonstrated and discussed in Chapter 3.

1.5 Coherent Raman Scattering

Molecular vibrational responses provide a label free alternative to fluorescence for a distinct signal generated at the sample location. Fluorescent labels have the potential to perturb biological functions and the delivery of labels to targets may be challenging. Raman signals are produced by inelastic light scattering from the molecular vibrational modes of the sample. By probing the vibrational resonances of chemical bonds within the sample, Raman imaging provides a label free contrast method with chemical sensitivity. A drawback of Raman scattering is that it is a relatively weak interaction.

Coherent Raman Scattering (CRS) uses a redistribution of energy between the sample and two incident light fields to convey information about molecular vibrational modes within the sample. In coherent anti-stokes raman scattering (CARS), the signal has the form of a new blue shifted light field, generated at the sample, with an intensity that increases as the difference frequency of the input beams approaches a vibrational resonance. The response boosts the spontaneous Raman effect as the number of molecular reporters within the focal volume increases and contribute coherently to the detected signal. Simultaneously, an energy gain or loss corresponding to the energy of the excited mode can be registered in the incident beams as is the case in stimulated Raman scattering (SRS). In imaging mode CRS is often implemented in a point scanning configuration and can achieve sub-micron lateral resolution with a $\sim$1 micron axial sectioning capability.

Rapid electronic oscillations induced by the two incident light fields can develop oscillations at additional frequencies. Raman active modes give rise to electron oscillations at the difference frequency of the two incident fields. These difference frequencies can be probed as sidebands of the incident frequencies. By tuning the difference frequency to distinct resonances, a contrast mechanism based on the molecular bonds present in the sample results. A common target for CARS and SRS are lipid droplets that compose micrometer-sized intracellular organelles. The methylene rich lipid within the focal volume can reach 10^{10} CH2 units, producing a strong vibrational signature.

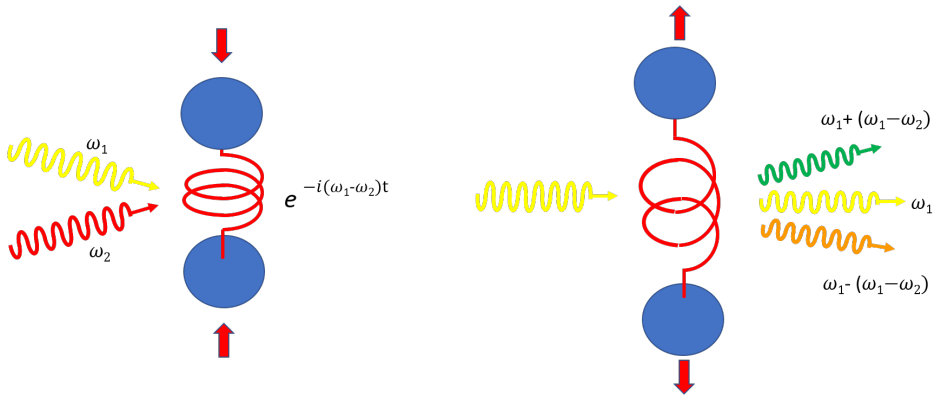

FIGURE 1.3: Classical picture of CRS

CRS techniques typically utilize pulsed near-IR laser sources with high peak field intensities to induce a nonlinear response from molecules within the focal volume. This results in better lateral resolution and tissue penetration than linear IR methods due to the shorter wavelengths involved and the strong absorption of water in the IR. Near-IR sources also scatter less in tissue than visible light that may be used in a spontaneous Raman microscope (Benninger and Piston, 2013; Jacques, 2013; Tang et al., 2018).

To observe dynamic biological processes, pixel dwell times on the order of microseconds are required for a scanning microscope (Cheng and Xie, 2015) Raman systems based on a spontaneous interaction may require tens of minutes to acquire an image. CW SRS was demonstrated in 1977 (Owyoung and Jones, 1977) and later used as an imaging method by Hu et al. but the resulting signal was three orders of magnitude less than what is observed for picosecond pulsed lasers (Hu et al., 2013), and is limited to pixel dwell times on the order of milliseconds. CARS and SRS using pulsed lasers have achieved video rate imaging with sub microsecond dwell times (Saar et al., 2010; Evans et al., 2005) with imaging depths on the order of 100 microns (Cheng and Xie, 2015). Video rate CARS imaging of lipids in the skin of living mice

are one demonstration of its *in vivo* capabilities (Evans et al., 2005). Increasing the imaging depth by an order of magnitude would greatly increase the utility of CRS for medical applications.

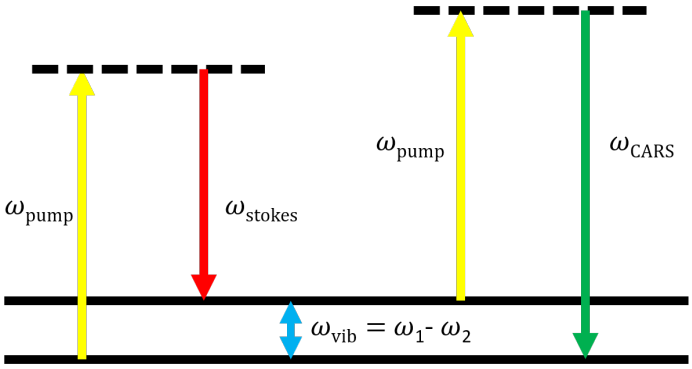

FIGURE 1.4: CARS

CARS creates a parametric exchange of energy between the sample and incident light fields in which the sample remains in the ground state after the interaction. A pump photon and a probe photon establish a coherence between the ground state and a vibrational excited state which is then probed by another pump photon. The resulting CARS photon at $2\omega_{pump} - \omega_{stokes}$ is spontaneously emitted and is blue shifted relative to the input beams, allowing for simple discrimination from the input fields with optical filters. The energy contained in the anti-stokes photon is derived from the changes in energy of the incident light fields, enabling the detection of a CARS signal without depositing an energy quantum in the material. While the presence of an vibrationally excited state enhances the energy exchange between the light fields, even in the absence of such a state electron motions can mediate the CARS interaction, thus producing a $2\omega_{pump} - \omega_{stokes}$ photon without the involvement of a vibrational resonance. This contribution is called the non-resonant background. Its presence can overwhelm the vibrational contribution and

thus constitutes an unwanted background. Models of signal generation in CARS within the focal volume point to methods of reducing non-resonant effects.

The coherent nature of CARS requires consideration of phase matching conditions for all the light fields involved. The simplest geometry is a collinear arrangement where incident beams and the signal field are all aligned to one spatial direction. For spatially extended samples, CARS signal generation involves a buildup over a characteristic coherence length where the propagating signal field stays in phase with signal generated further along the propagation direction. The phase mismatch for CARS may be expressed as a difference in the momentum k-vector of the signal at the anti-stokes frequency and the k-vectors of the photons that prepare the CARS photon, $\Delta k = k_{as} - (2k_{pump} - k_{stokes})$. Under the tight focusing conditions created by a high N.A. objective, the wave vector mismatch does not significantly effect emission strength resulting from a focal length on the order of microns (Potma, Boeij, and Wiersma, 2000).

1.6 SECARS

Although the Raman effect is a weak light-matter interaction, strong signals can nonetheless be generated with the help of the enhanced optical properties of nano-structured metals (Jeanmaire and Duyne, 1977; Schatz, 1984). The concentration of the excitation field and the enhancement of radiative rates mediated by the metal's plasmonic modes can raise the otherwise imperceptible Raman signal from single molecules to detectable levels (Nie and Emory, 1997; Kneipp et al., 1997; Dieringer et al., 2007). The amplifying qualities of metallic nano-structures are ideally suited for detecting and identifying molecular species at low concentration, spurring the development of chemical sensors based on surface-enhanced Raman scattering (SERS)

into a burgeoning field. The principle of SERS, however, has not yet been successfully translated to improved Raman imaging and microscopy. Because the optical enhancement in SERS substrates is confined to nano-sized hot-spots, signal amplification is generally not uniform across the entire field of view, rendering this approach unsuitable for detailed imaging applications (Steuwe et al., 2011).

To achieve uniform amplification of optical signals, flat metal films can be used as the plasmonic material. Compared to the localized surface plasmon modes utilized in most SERS substrates, the optical enhancement at flat films is facilitated by surface plasmon polariton (SPP) excitations, which generally offer lower field enhancement but provide amplifying qualities that are constant within the two-dimensional sample plane.

SPP-based Raman spectroscopy has been used in various sensor applications (Giergiel et al., 1988; Meyer, Le Ru, and Etchegoin, 2011; Meyer et al., 2012; Li et al., 2012), and has also been employed to boost the signals in imaging mode Yoo et al., 2012. For instance, the SPP-Raman microscope has been used to visualize micro-structured films of organic materials (Zerulla et al., 2003). Application of SPP-based Raman microscopy to biological samples remains, however, a challenge. To raise the weak Raman signals from the endogenous compounds in biological specimens, further amplification is desired. The latter can be achieved, in principle, by combining SPP excitations with coherent Raman scattering (CRS) microscopy.

While the enhancement factor associated with an individual SPP field is generally less than an order of magnitude over the incident, SPP mediated 4WM experiments benefit from a multiplicative enhancement in the detected signal. 4WM experiments of liquid benzene on a silver film established that the SPP enhanced peak fields are capable of exciting a CARS signal in a surface bound sample, opening up

the possibility of biological applications (Chen et al., 1979)

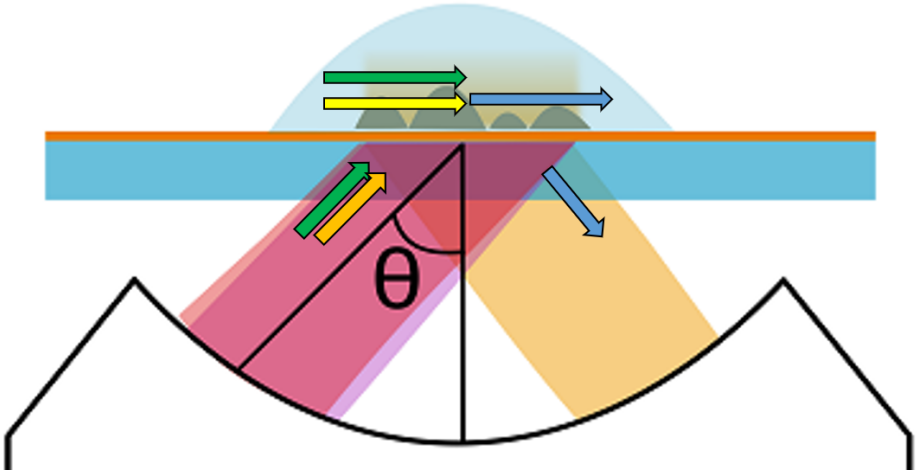

FIGURE 1.5: SECARS

In an SECARS microscope, a pump and Stokes beam are individually coupled to co-propagating SPP fields on the gold film by tuning the incidence angles to their respective Kretschmann angles. This allows matching of the in-plane momentum of the incident field to the SPP momentum. Phase matching conditions for the CARS signal beam result in an anti-stokes SPP, propagating in the same direction as the incident SPP fields, leaking detectable radiation to the far field in the process. As with conventional point scanning CARS, the signal intensity increases as the difference frequency of the input beams approaches a vibrational resonance of the sample. We have previously demonstrated that signals from lipid structures carry a spectral dependence expected for excitation of CH_2 vibrational modes(Fast et al., 2016).

The important role of the gold film in SECARS is apparent in the imaging properties of the microscope. The coherent CARS signal produces diffractive tails and flares that are not familiar in conventional point scanning CARS systems. Instead

these imaging artifacts bare similarities to what is observed in plasmonic imaging techniques. To better understand these effects, a Green's function approach can be used to model the electric field response induced by a point dipole oscillating under the influence of the excitation fields. The epi-detected radiation collected in the far field is modified by the optical properties of the gold film through generalized Fresnel coefficients. By mimicking the sample volume as a discrete collection of point dipoles, the coherent image formation process shows clear interference effects that resemble those seen in the SECARS microscope.

In spite of the imaging artifacts encountered in SECARS, applications requiring low illumination densities may benefit from this method. In Chapter 5, the capabilities of the microscope are discussed and a model for the imaging properties of the system are presented. As demonstrated by techniques such as SPCE and Cofefe, gold films are multi-functional, suggesting that future advancements may stem from a more synergistic use of these properties.

Chapter 2

Wide field excitation of SPP's on gold films

2.1 Introduction

The complex dielectric function of gold provides an analytical quantity for describing the electrical and optical properties of thin films ($\varepsilon \sim -25.6 + 1.6i$ at 817 nm). In the case of propagating electromagnetic waves along the x direction at a metal/dielectric interface, the dispersion relation may be expressed in terms of the wavelength dependent dielectric constants of the materials at the interface. Quantities such as the SPP coupling angle in a Kretschmann configuration, which matches the in-plane component of the incident field momentum to the in-plane SPP momentum for a given frequency, may also be expressed in terms of the dielectric constants of the corresponding three layer system.

$$k_x = \frac{\omega}{c}\sqrt{\frac{\varepsilon_1 \varepsilon_2}{\varepsilon_1 + \varepsilon_2}} \tag{2.1}$$

$$\theta_{SPP} = \sin^{-1}\left(\frac{1}{n_3}\sqrt{\frac{\varepsilon_1\varepsilon_2}{\varepsilon_1+\varepsilon_2}}\right) \tag{2.2}$$

In terms of the real and imaginary components of the in-plane momentum, k_x, we obtain the following expression.

$$k_x = k_x' + ik_x'' = \left[\frac{\omega}{c}\left(\frac{\varepsilon_1\varepsilon_2'}{\varepsilon_1+\varepsilon_2'}\right)^{\frac{1}{2}}\right] + i\left[\frac{\omega}{c}\left(\frac{\varepsilon_1\varepsilon_2'}{\varepsilon_1+\varepsilon_2'}\right)^{\frac{3}{2}}\frac{\varepsilon_2''}{2\left(\varepsilon_2'\right)^2}\right] \tag{2.3}$$

As the SPP propagates along the film, energy is lost due to ohmic losses in the film. The characteristic propagation length, L, of an SPP is associated with the imaginary component of the dispersion relation ($\sim 50\mu$m for 817 nm with an air interface).

$$L = \frac{1}{2k_x''} \tag{2.4}$$

The decay of the field away from the interface into the dielectric material determines the effective probing volume in SPP based microscopes. The penetration depth of the SPP into the metallic surface is generally smaller due to the lossiness of the film and effects the degree of leakage radiation that is detected in a Kretschmann configuration. In the equation below, the index i refers to the metallic side ($i = 1$) of the interface or the dielectric side ($i = 2$).

$$z_i = \frac{\lambda}{2\pi}\left(\frac{|\varepsilon_2'| + \varepsilon_1}{\varepsilon_i^2}\right)^{\frac{1}{2}} \tag{2.5}$$

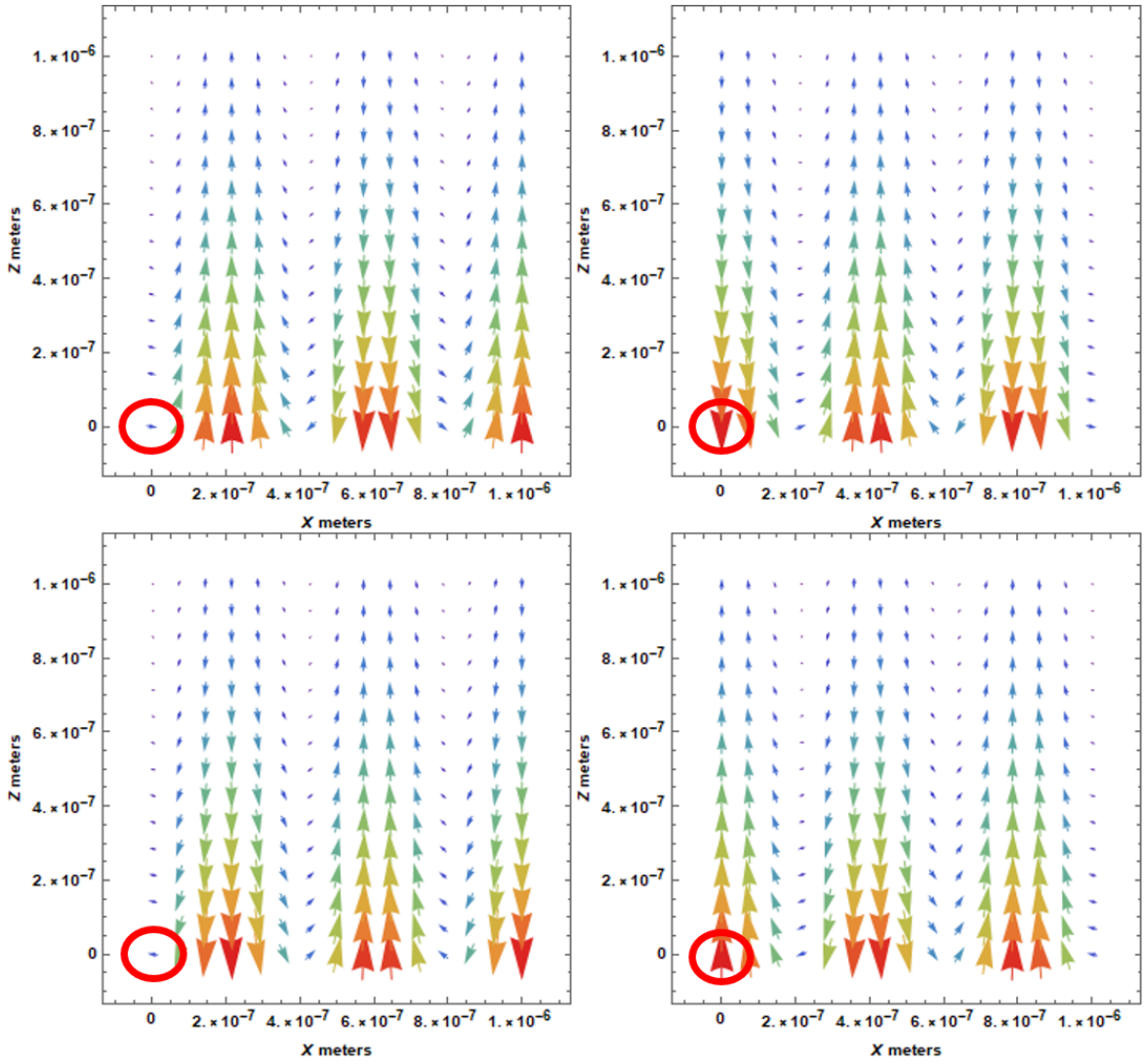

FIGURE 2.1: SPP field at time intervals of T/4 displaying an elliptically polarized field with greatest magnitude in the direction away from the interface

The full time dependent expression for the propagating SPP field, neglecting losses in the film, may be expressed in the form in eq. 2.6. As seen in Fig. 2.1, the field propagates in the positive x-direction and decays in magnitude away from the interface. Four equally spaced time intervals over one period T are displayed. Focusing on a single spatial coordinate demonstrates the elliptical nature of the field. The ellipticity of the field depends on both wavelength and the dielectric constants of

the materials at the interface. In the case of gold excited by 817 nm light, the field can be seen to be nearly polarized perpendicular to the interface.

$$E[x,z,t] = \left(1, 0, -\frac{k_x}{k_z}\right) e^{i(k_x x - \omega t + k_z z)} \tag{2.6}$$

Numerous experimental measurements of dielectric constants across thickness, and incident wavelength reveal a complicated material response dependent on the band structure of gold as well as the preparation dependent inhomogeneities across films. Ellipsometry measurements by Olmon et al on thermally evaporated 200nm thick gold films safely fall within the bulk regime and point to intraband transitions at lower energies and an onset of interband contributions in the visible region(Olmon et al., 2012). Measurements on thin films ∼25-50nm show a characteristic thickness above which dielectric constants of gold do not change drastically from their bulk values(Johnson and Christy, 1972a). In the ultra-thin regime, measurements of dielectric properties become inconsistent and begin to deviate from their bulk values.

This is in part due to the difficulty in producing homogeneous and uniform thin films. Vapor deposition is a common method for producing metallic films for microscopy applications. The simplest way to incorporate SPP's into a microscope is to add a negligible amount of evaporated gold to a standard BK-7 glass coverslip. Typically an adhesion layer (∼1–2nm Cr) is required to bind the gold layer to the substrate. Substrate material, preparatory cleaning procedures, temperature during evaporation, film thickness, all can effect the resulting surface morphology. Ultra-thin films often consist of disconnected islands as opposed to a two dimensional film. Unsurprisingly, these films are highly transmissive and have very low electrical conductivity. Continuous gold films down to thicknesses of ∼5nm have

been achieved on fused silica activated with mercapto-silane to promote Au adhesion along with high deposition rates,$\sim$10 Angstroms/sec. The optical constants of these films still show deviations from bulk values that are difficult to assign to morphological properties of the film however(Kossoy et al., 2014). Silicon substrates offer a more uniform substrate than BK7 coverslips but the lack of transparency limits their use in many microscope configurations. Mica also provides a flatter surface than glass and is ultra clean after removal of a thin layer of mica before deposition. The benefit of a freshly cleaved surface, however, complicates quantification and repeatability due to the uncertainty in substrate thickness. Template stripped films have been shown to produce high quality gold thin films but involves a mechanically robust transparent substrate with an adhesive layer to peel a gold film from an atomically flat opaque surface. The mechanical strain involved in peeling the substrate requires a thick glass layer that can be outside of the working distance of high NA objectives, and the necessary addition of an epoxy layer complicates interpretation of the optical properties of the entire three layer structure. Practical applications of SPP's not only require a careful consideration of the particular surface morphology for a given production method but also how SPP's interact with characteristic surface features.

2.2 Methods

Two laser sources are used in the experiments described in this chapter. The first consists of a 76 MHz Nd-Vanadate amplified oscillator (PicoTrain, High-Q), which produces 7 ps pulses at a center wavelength of 1064 nm. A portion of the output is frequency doubled and used to synchronously pump an optical parametric

oscillator (OPO, Levante Emerald, APE-Berlin). The latter delivers tunable radiation in the 750–950 nm range. The second light source is a Titanium:sapphire laser (Mira900, Coherent), which produces a 76 MHz pulse train of ∼150 fs pulses. For the experiments discussed here, the picosecond source is tuned to 817 nm, and the femtosecond wavelength is set to 810 nm.

The near-IR beams are conditioned with a spatial filter and expanded to a ∼7 mm beam diameter, exhibiting a Gaussian transverse profile that is linearly polarized. A 200 mm achromatic lens (Edmund Optics) focuses the beam on the back focal plane (BFP) of a 60x 1.49 NA oil immersion objective, (APON60XOTIRF, Olympus) providing wide-field illumination

The focusing lens is attached to a movable mirror that translates the lateral position of the focused spot on the BFP, resulting in an angular adjustment of the collimated beam incident on the coverslip. In this configuration, the diameter d of the illuminated field of view (FOV) can be estimated from the following ratio:

$$d_{FOV} = d_{beam} \frac{FL_{\text{objective lens}}}{FL_{\text{focusing lens}}} \tag{2.7}$$

where FL denotes focal length. In the picosecond experiments described here, the FOV is set as 105x105 μm^2.

Sample substrates consist of borosilicate glass coverslips (BK-7, VWR) coated with gold. Gold thin films are evaporated to a thickness of 30 nm on borosilicate glass coverslips (BK-7, VWR), which are pretreated with a 2 nm Cr adhesion layer. For patterned Au films, lithographic masks are used for depositing S1808 photoresist (Shipley) onto the surface, followed by chemical etching, creating patterns consisting of 20 μm wide Au stripes, with a spacing of 20 μm between the stripes.

2.3 Results

2.3.1 Wide-field excitation of SPP modes

To generate the surface-bound SPP excitation field, the freely propagating near-IR beam has to be coupled to the surface plasmon mode. We have chosen an objective-based Kretschmann configuration, in which the beam is incident on the gold/air interface at the SPP coupling angle of $\theta = 42.3^o$.

The alignment of the beams is facilitated by monitoring the backreflection of the excitation beams onto the CCD camera. Figure shows the backreflection of the beam at 817 nm incident on a striped gold film. In Fig 2.2 , the coupling angle is below the Kretschmann angle, resulting in a strong reflection at the gold stripe (bright) and a weak reflection from the bare glass (dark). When the incident angle is tuned to $\theta_{pump} = 42.3^o$, phasematching with the SPP mode occurs and energy is transferred from the freely propagating mode to the surface-bound mode. The latter can be inferred from Fig 2.2 , which shows greatly reduced reflection at the gold stripe, whereas the signal from the exposed glass is elevated due to total internal reflection. As in previous surface plasmon resonance microscopy studies (Halpern et al., 2014), efficient SPP coupling is achieved over the entire FOV.

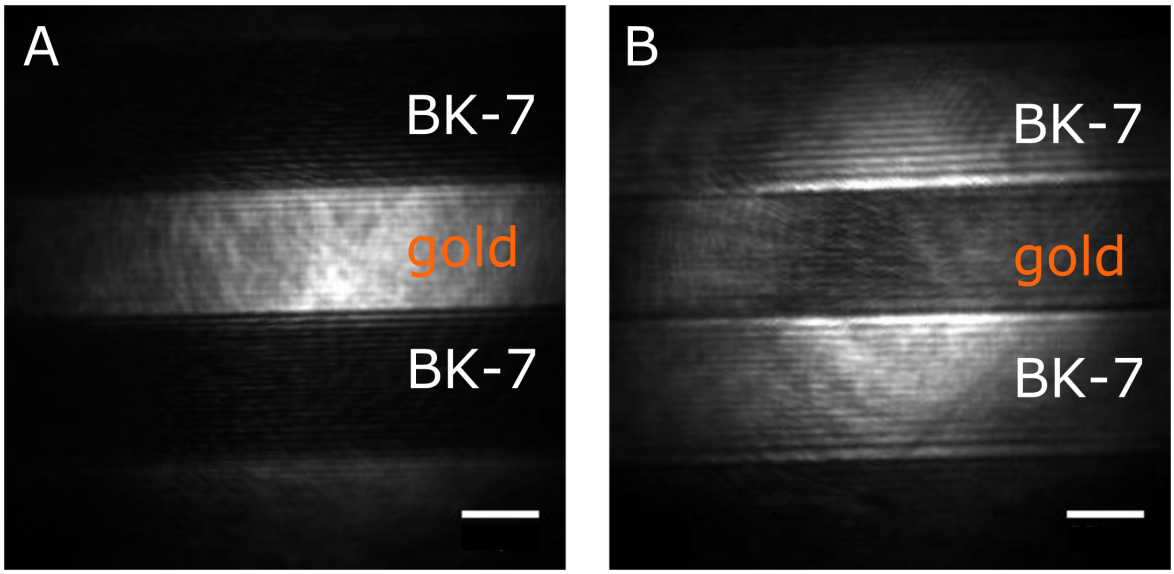

FIGURE 2.2: Coupling of light to SPP at the gold film-air interface. Reflection image of the beam at 41^o, before light couples (A) and at 42.3^o when energy transfer to the SPP mode occurs (B). Scale bars are 20 μm.

The field enhancement generated relative to the incident field is far less than what is observed in SERS and TERS where electromagnetic fields are confined to a nanoscopic volume which may provide enhancement factors on the order of 10^{10}(Le Ru et al., 2007). Field confinement in the axial dimension alone is expected to produce a more modest enhancement at any given point on the film. In the FDTD simulations depicted in Fig. 2.3 , the enhancement of a near-IR beam at an metal/water interface is $\sim$ 5-7. It is important to note that this does not predict the full enhancement achievable with flat metallic films as SPR experiments typically use thicker films than the 30 nm thickness used in these experiments. Numerical arguments show that for a gold film excited in a Kretschmann configuration, optimal enhancement is achieved with films that are near 50-70 nm thick.(Fontana, 2006)

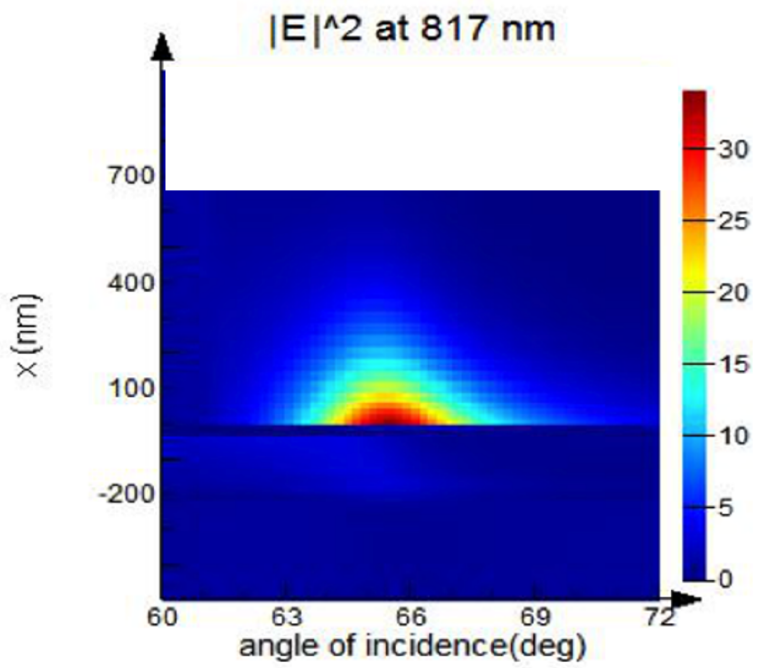

FIGURE 2.3: Field intensity above the gold film as a function of indidence angle for a 30nm Au film

While a thicker film may couple more efficiently to SPP modes, thinner films may experience greater leakage radiation which is more desirable for certain applications such as SPCE. Field enhancement in a Kretschmann configuration with a 50nm gold film has been theoretically estimated as $\sim 10^2$(Meyer et al., 2012). It is also worth noting that reports of SERS enhancement on flat films are typically $\sim 10^3$-10^4 (Meyer et al., 2012). Reciprocity arguments suggest that the same mechanism that enhances the incident field will also enhance the detected raman signal. Evidence of this effect may also be present in the experiments described below.

2.3.2 Gold film fluorescence

Interestingly, the addition of non-fluorescent biological materials to the gold surface surface results in an unexpected emission. The figure below demonstrates that a clear signal can be obtained from lipid droplets. The image is free from diffraction patterns that are often associated with SPRI where changes in refractive index at the surface produce interference effects with the reflected incident beam. In fact the signal persists even with the presence of a band pass filter centered at 660 nm which blocks the incident wavelength, excluding the SPRI mechanism as the source of the signal. The broadband nature of the signal and the absence of interference artifacts suggest a fluorescence process, and yet it is still observed for samples that are incapable of autofluroescence. Further studies suggested that the signal originates from the film itself in the vicinity of the sample.(Fast et al., 2016)

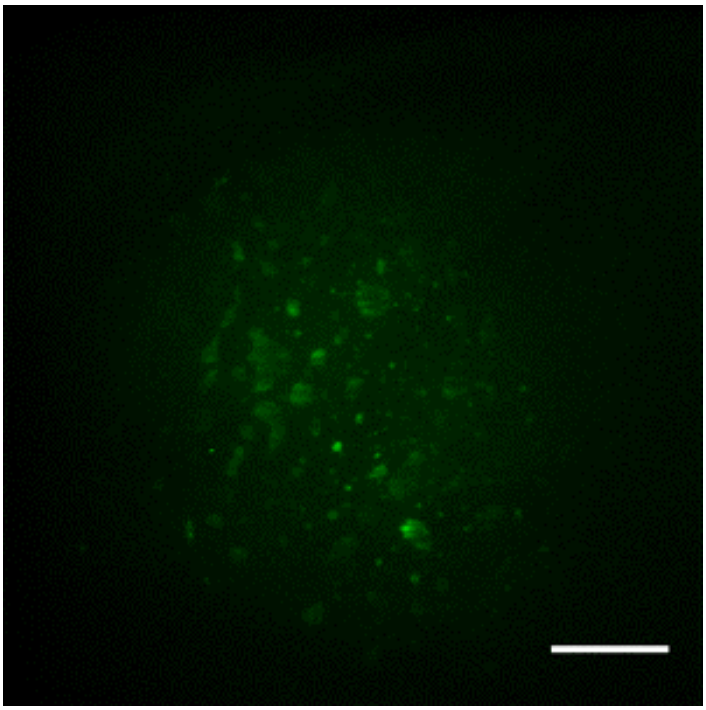

FIGURE 2.4: Lipid droplets on the surface of a gold film illuminated by 817nm picosecond light incident at the SPP resonance angle. A bandpass filter 660/40, is used to isolate the fluorescence signal from the incident light field

Fig. 2.5 shows another example of lipid droplets adhered to the surface, illuminated with an 800nm fs source, and the corresponding back focal plane image. By placing a Bertrand lens in the detection path, the distribution of emitted photon momentum can be projected onto the CCD. The bright ring apparent in the BFP image is characteristic of leakage radiation from SPP fields, corresponding to a specific k-vector(Drezet et al., 2008; Bharadwaj, Bouhelier, and Novotny, 2011). The rings appearance through the bandpass filter suggests that the detected emission couples to SPP modes before outcoupling to the far field, as opposed to leakage of the incident SPP.

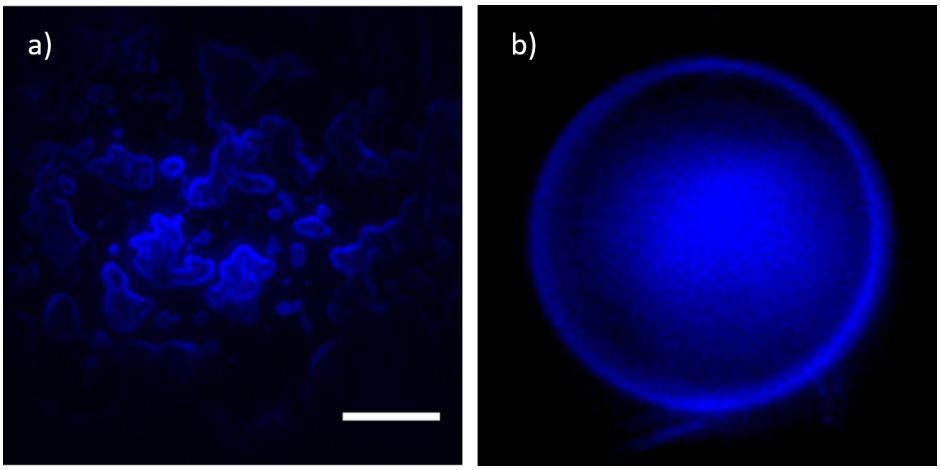

FIGURE 2.5: a) Cholestorol Oleate adhered to the surface. b) Back focal plane image corresponding to a).

In SPP based microscopes this signal may be considered an undesirable background effect.(Fast et al., 2016) The ability to localize particles at the surface with high signal to noise raises the possibility of label free sensing applications. In able to translate this effect to practical sensing methods, a better understanding of the sensing surface itself is required. Another prominent observation from gold films is the strong outcoupling of light from seemingly random locations on a bare sensor surface. SEM images reveal that the source of this emission is from inhomogenites in the film.

2.3.3 Film defects and hotspots

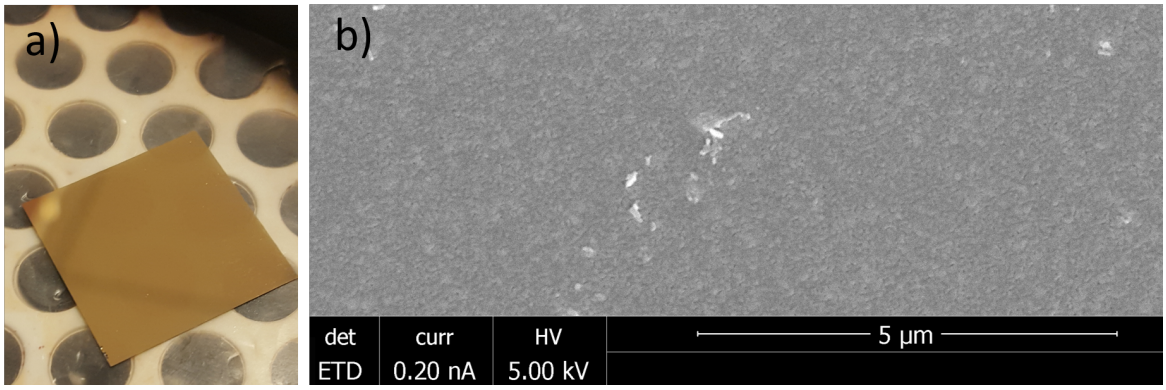

FIGURE 2.6: a)Typical gold coated coverslip produced by vapor deposition. b) SEM image of a gold coverslip surface with high density of defects

Exciting SPP fields over a wide field of view presents challenges in terms of film quality. Instead of film smoothness on the grain level of the film, the concern is uniformity of the film over large areas (100μm x 100μm). Gold protrusions and pinholes in thin films have been well documented across multiple film production techniques, and many methods of minimizing their presence have been suggested. Defects in the film result in "hotspots" that strongly out-couple light from the SPP fields. Even high quality films can not completely exclude these inhomogeneities, highlighting the importance of quantifying their emission properties. Fig. 2.6 shows an example of a typical surface feature. Under thermal vapor deposition, the surface quality varies greatly with preparation method and may not be uniform within the same batch or even within different areas of a single coverslip. Isolated gold defects react strongly with SPP fields on the surface, and can dominate the entire field of view for surfaces with a high density of defects. The ability to consistently produce films with minimal defects over large areas will be key to distinguishing effects

observed in surface bound samples from emission associated with inherent surface features.

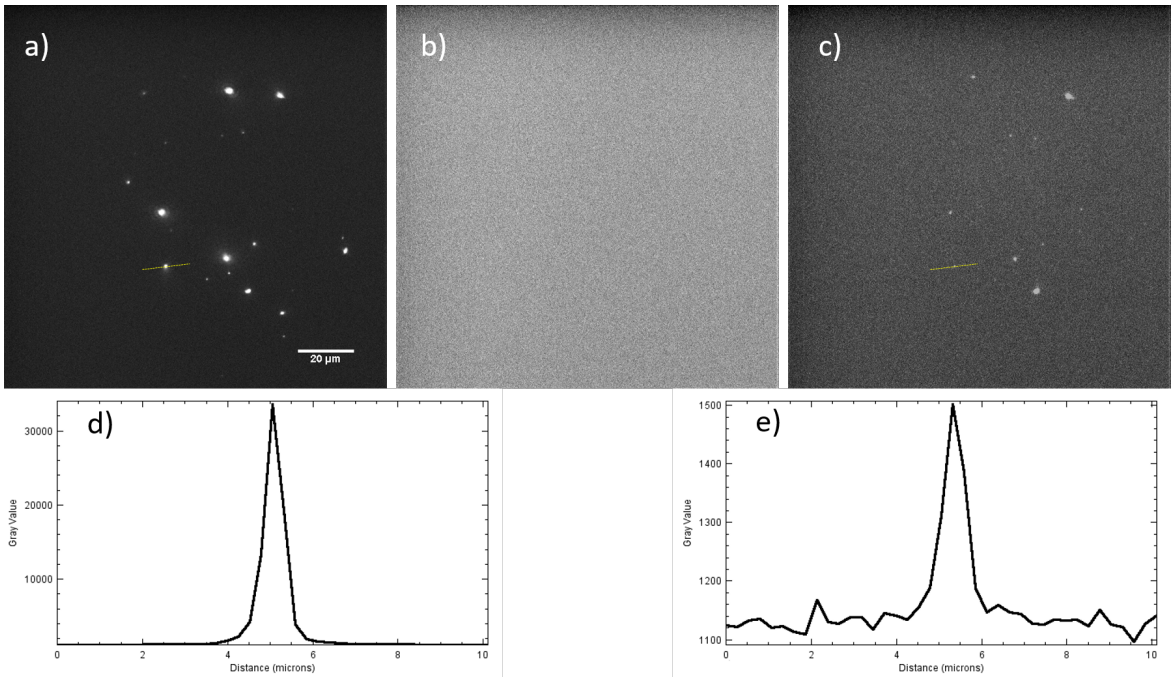

FIGURE 2.7: a) Outcoupling of light from surface defects under SPP illumination from 150 fs, 50 mW pulses b) Same region as in a), illuminated with 50 mW of CW light. c) Outcoupling produced by 360 mW of CW light

The low powers used in typical SPRI microscopes along with difference imaging schemes and a small detection window around the excitation wavelength, limits the broadband response of hotspots. For comparison, a bare gold film was illuminated with both a CW and 200 fs pulsed laser to demonstrate the effects of high peak fields on emission from surface defects. A bandpass filter (625/90) is included in the CCD detection path to filter out incident light from the image. With a pulsed source at 50 mW surface defects appear as very bright spots, registering ∼30,000 counts on a CCD camera over a 1 second exposure, accumulated over ten frames. In CW mode, 50 mW produces no detectable signal. Increasing the CW power to 360 mW results in clear emission from the same surface defects but only registers

$\sim$1500 counts, nearly 20 times less than the pulsed beam at much lower average power. Clearly, excitation of SPP fields with pulsed sources requires a high degree of surface uniformity to allow for easy distinction between emission from film hotspots and signals originating from the position of sample material at the surface.

Emission from defects also show irregular behavior in time. Occasional blinking effects are observed but the most common observation is an intense emission that appears directly after illumination which then decays on the timescale of seconds. The equilibrium intensity for hotspots shows a great deal of variability with higher equilibrium values corresponding to higher initial peak intensity, potentially reflecting the relative size of the defects. Similar effects are observed when gold nanoparticles are adhered to the gold surface, which provide a more uniform source for studying decaying and intermittent emission properties.

2.3.4 Gold particles in air

Both gold nanospheres and surface protrusions contain a large number of free electrons and have the potential to support localized surface plasmons, generating intense fields in highly confined spaces. Gold nanospheres and their plasmonic behavior have been well documented and can potentially provide some insight into the observed time profile from surface defects.

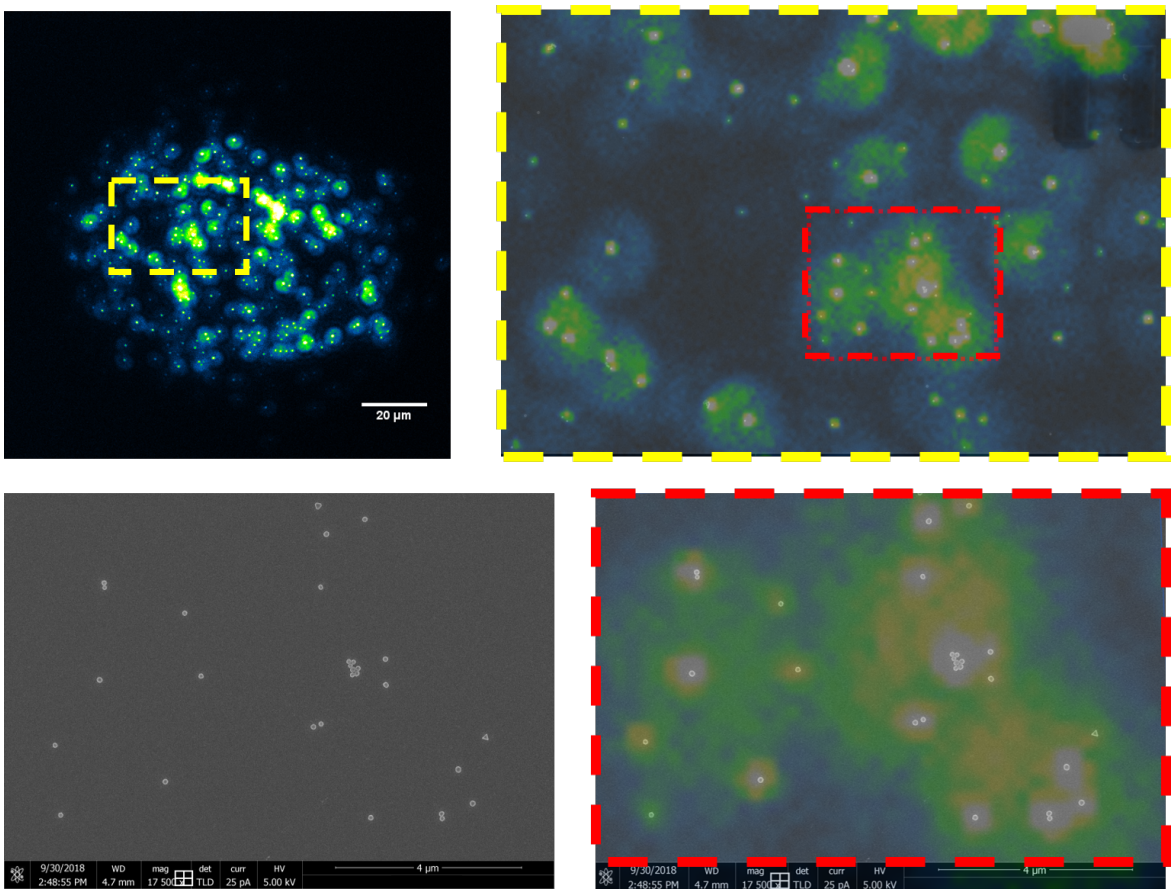

FIGURE 2.8: a) Signal image from 100nm Au in air adhered to the film surface. b)d) Overlay of signal with SEM image. c) SEM image of region of interest.

Temperature effects are an important factor in the spectra of metallic nanoparticles. A temperature increase in the solution surrounding a gold nanoparticle will alter the refractive properties of the solution, resulting in a decrease in the intensity of the plasmon resonance (Link and El-Sayed, 1999). To limit the effects of solution temperature in the observed decays, 100 nm gold spheres excited in air were recorded in time. Gold particles embedded in a glass matrix demonstrate a decrease in intensity of the plasmon absorption spectra with increasing temperature as well as a redshifting of the peak (Link and El-Sayed, 1999). This behavior can be

rationalized through temperature dependent Mie scattering (Kreibig, 1977). Similar observations have also been attributed to a decreased electron concentration at higher temperature, resulting in a modified spectrum (Doremus, 1964). Studies have shown that significant alteration of the spectrum requires a change of several hundred degrees (Link and El-Sayed, 1999).

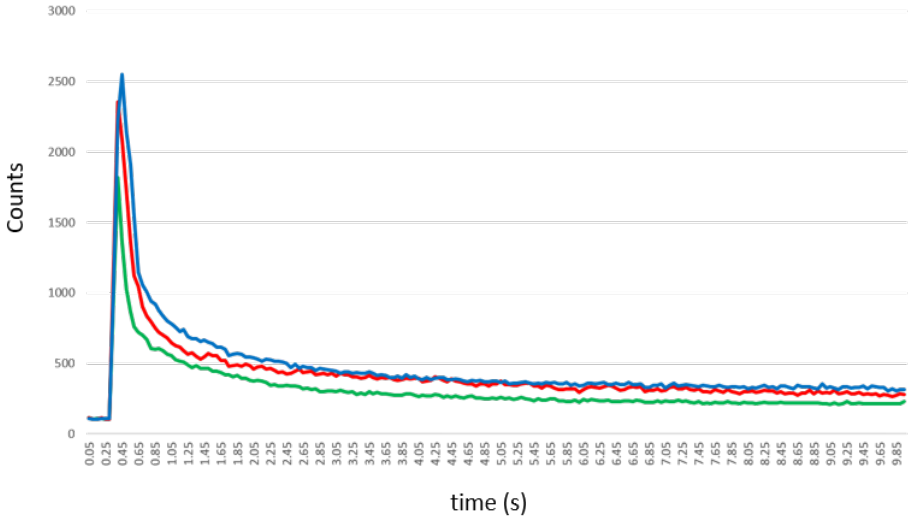

FIGURE 2.9: Counts from three representative 100nm Au spheres in air adhered to the film surface. With high illumination intensities (100 mW), signals typically display an intense initial flash which rapidly decays but remains visible. SEM images show no obvious morphological changes associated with modifications to emission intensity.

The long decay times observed for 100 nm Au spheres contrasts with the ultrafast thermal relaxation times associated with gold nanoparticles. If an individual laser pulse is sufficient to induce a small degree of melting, heating may gradually alter the spheres shape, changing its plasmonic spectrum(Kuhlicke et al., 2013). Melting a spherical particle could potentially form a flatter shape on the gold film where a largely p-polarized SPP field on the film surface would be applied along a shorter axis of the particle, resulting in reduced scattering intensity.

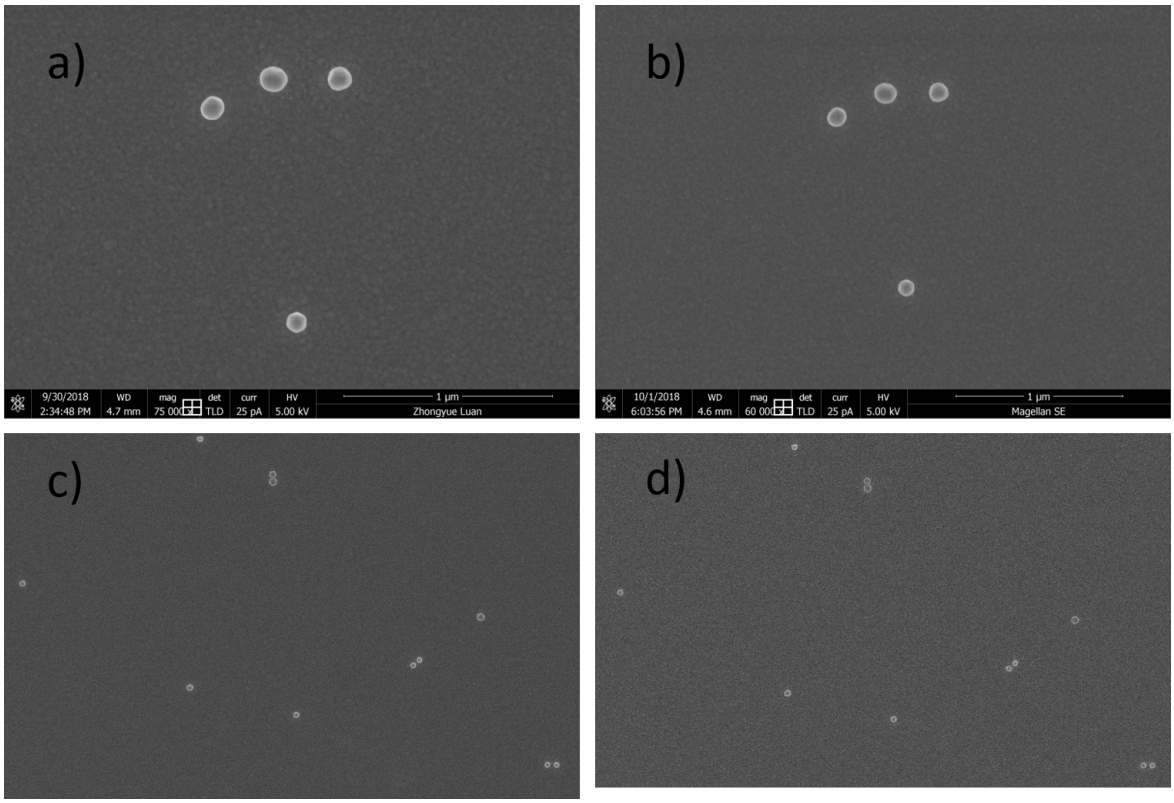

FIGURE 2.10: a)b) Before and after images of 100nm Au particles illuminated with 10mW for 100 seconds c)d) Before and after images of 100nm Au particles illuminated with 160mW for 100 seconds.

To investigate this possibility, SEM images of 100 nm Au particles adhered to the gold surface were taken before and after illumination at various powers. Even after high levels of SPP irradiation, the gold particles do not show any obvious signs of morphological changes due to heating. Temperature modifications to the particle can not be excluded entirely due to the limited resolution of the SEM images taken. Unresolvable features that are too small or are on the underside of the sphere are likely to experience the largest localized field enhancements and thus are more likely to be modified by heating effects. In general, temperature induced shifts in the emission spectrum may exaggerate reduction in intensity due to signal collection through a fixed band pass filter.

Another curious observation is the intermittent emission from a small subset of the gold particles. At high illumination intensities, very few particles display this behavior and tend to appear near the edge of the illumination area where excitation fields may be reduced. At lower excitation energies, blinking effects become much more common.

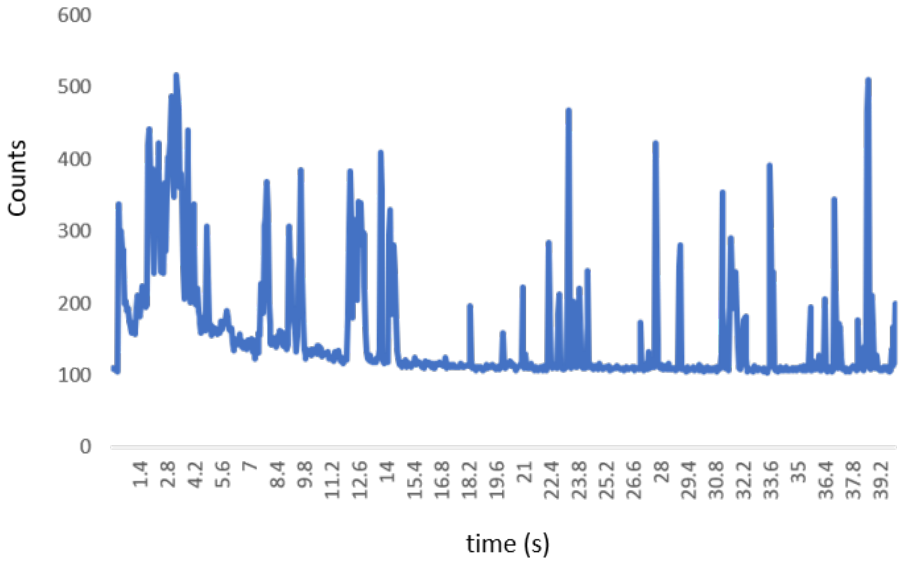

FIGURE 2.11: Counts from a 100nm Au sphere in air adhered to the film surface. At high illumination intensities, a small subset of particles show blinking behavior. At lower illumination powers (25mW), blinking becomes a much more common effect among the illuminated particles.

Photo-blinking of gold nanostructures under CW illumination have been previously reported in the literature. Photo-bleaching effects have been documented as well(Li et al., 2017; Yuan et al., 2016), though not in all reports involving blinking effects. Sinlgle photon luminescence experiments on nano-sea-urchins (NSU) using CW sources have shown that the enhanced fields generated by surface plasmon resonances confined to the sharp spine features of the nanostructure result in blinking effects(Su et al., 2010). Similar observations have been made on gold nanospheres ($\sim$ 15-20 nm) and individual nanoclusters ($\sim$ 2 nm)(Li et al., 2017; Yuan et al., 2016).

The proposed emission mechanism begins with a recombination of d-valence band holes with sp-conduction electrons, excited by a single photon. In some instances, the excited hole may recombine with another electron before the excited electron is scattered near the Fermi surface. The energy released in this Auger process is lost as heat energy as opposed to photon energy, leading to a "dark" state observed in blinking.

Intensity decay over long periods of time have been reported from ensembles of nano-clusters under ambient environmental conditions(Yuan et al., 2016). Interestingly, the decay was not observed while nano-cluster ensembles were immersed in solution. Individual nano-clusters on the other hand do not decay but blink and eventually bleach. TEM images have demonstrated that Au nanospheres contain crystaline domains that may act as separate emitters, contributing to the same diffraction limited spot on the camera (Li et al., 2017). This further relates emission from a nano-cluster ensemble to 100nm spheres, although the set of domains within the particle is expected to form a rather small ensemble. The long blinking lifetimes observed here however appear to be much longer than the decay time of the proposed ensemble of emitters.

While an Auger process may play a role in the emission from SPP excited Au spheres, a simple ensemble picture is insufficient to describe the rapid intensity decay at high powers. Small points and edges of Au spheres are expected to generate high field enhancement and are correspondingly expected to experience the greatest rearrangement due to local heating. The lack of rapid decay behavior at lower incident powers further supports local heating of the particle as a primary factor in its emission characteristics.

2.4 Conclusion

SPP fields can be efficiently driven over a wide area of a thin gold film using high N.A. objectives and near-IR sources. Coupling to the SPP resonance angle becomes more challenging as the index of refraction of the dielectric layer increases. As the coupling angle increases, the incident beam must be displaced farther from the optical axis of the objective. For samples in solution this imposes precise alignment requirements but remains within reach of high NA objectives. The resulting excitation field provides a novel method for probing the region just above the film with intensities that are expected to produce nonlinear light-matter interactions that may be detectable when light fields with sufficient peak intensities are used. The film itself can become a source of fluorescence emission in regions where SPP fields become locally enhanced and may be induced by a target particle adhered to the film or inherent surface features of the film. Both contributions must be accounted for in further applications of this setup.

Chapter 3

COFEFE

3.1 Introduction

Surface plasmon resonance (SPR) sensing is a technology used for measuring binding and dissociation kinetics of biomolecules at a gold sensor surface.(Zhang and Uttamchandani, 1988; Homola, Yee, and Gauglitz, 1999; Boozer et al., 2006; Homola, 2008; Phillips and Cheng, 2007) Such biomolecular interactions include interactions among proteins, peptides, nucleotides, sugars and other molecules. In pharmaceutical, clinical and biotechnological research, for instance, knowledge of biomolecular interactions is key in determining efficacy of a drug, understanding immunological responses or discovering new therapeutic targets, to name just a few.

Whereas the SPR technique is very sensitive, its common implementation is unable to detect individual binding and dissociation events. Kinetic SPR data is typically the result of ensemble averaging over many events, integrated over both space and time. Consequently, rapid on/off events at particular sites on the sensor surface are not registered, as they are averaged out by the slower dynamics of the ensemble. Other unexpected binding patterns at particular sites also go unnoticed. Such

outlier behavior can be important, as these events may signify functional aspects of the molecular interaction, related to particular conformations, density related binding kinetics or other effects of direct relevance. The ability to see all binding/dissociation events in parallel would significantly enhance the analytical capabilities of the SPR sensor.

Individual binding/dissociation events can be studied with a microscopic imaging version of SPR, namely surface plasmon resonance microscopy (SPRM).(Jordan et al., 1997; Brockman, Nelson, and Corn, 2000; Kano and Knoll, 2000; Huang, Yu, and Zare, 2007; Weichert et al., 2010) The latter technique makes it possible to visualize individual events in parallel with a camera, thus enabling multiplex detection of particles interacting at the sensor surface. SPRM has been successfully employed to probe individual cells(Wang et al., 2012), bacteria and viruses(Syal et al., 2015; Wang et al., 2010), DNA(Yu et al., 2014; Halpern et al., 2014), and protein structures.(Maley et al., 2017) The ultimate sensitivity of SPRM is limited by various factors.(Raether, 1977; Kooyman et al., 1988; Yu et al., 2017) One limitation is related to the fact that SPR methods are not background-free, as small changes in the light intensity need to be discriminated against a bright background. Another limiting factor is the non-ideal pointspread function of SPRM, which is characterized by long diffractive tails that affect the spatial resolution of the technique. To increase the spatial resolution, special algorithms have been developed that improve the performance of the SPRM device, achieving an effective resolution on the sub-micrometer scale.(Yu et al., 2017) Nonetheless, the restored pointspread function is non-symmetric and may exhibit residual flaring.

The SPRM technology would benefit from an optical signaling mechanism that is associated with a well-behaved pointspread function and that produces a positive signal relative to a low background. In this work, we present an optical signature at

the gold sensor surface that addresses the aforementioned issues. The signal, which we attribute to two-photon excited fluorescence in the gold film, is triggered by binding of particles to the surface. The pointspread function, which appears against a dark background, is incoherent and thus devoid of interferences among detected spots. The resulting technique is related to two-photon surface plasmon-coupled emission (SPCE) microscopy(Gryczynski et al., 2005; He et al., 2009), but without the need to incorporate fluorophores and thus allowing label-free probing of targets. We discuss the optical layout of this new approach and present its capabilities for detecting individual particles in the vicinity of the sensor surface.

3.2 Materials and Methods

A schematic of the sensor device is shown in Fig. 3.1. The light source is a Titanium:sapphire laser (Mira900, Coherent), which produces a 76 MHz pulse train of $\sim$150 fs pulses. In the experiments the center wavelength is set to 810 nm. The linearly polarized source is conditioned with a spatial filter to generate a clean Gaussian transverse profile of 10 mm diameter. The collimated beam is then focused by a f = 250 mm lens onto the back focal plane of a high numerical aperture objective (NA 1.49 oil, Olympus). The resulting collimated beam emerging from the objective corresponds to a circular illumination spot with a diameter of $\sim$ 120 μm on the sensor surface. The sensor surface consists of a borosilicate coverslip coated with a 30 nm thick gold film. By translating the beam in the back focal plane, the incidence angle of the collimated beam at the surface can be tuned to the Kretschmann angle for excitation of a surface plasmon polariton (SPP) mode at the gold/water interface ($\sim 65^o$). The resulting two-photon luminescence from the gold film is collected in the epi-direction by the objective and separated from the incident beam by a 700 nm

short wave pass dichroic mirror. The signal is subsequently filtered by a 625 nm±45 nm band pass filter and 750 nm short wave pass filter. In some of the experiments, a 1.6× telescope is incorporated in the detection path for increased magnification, resulting in an image distance of 169.5 nm per pixel with a $\sim$ 60 μm diameter field of view (FOV). Average illumination powers, determined before the objective lens, are between 12 mW and 150 mW, depending on the FOV and the sample. For each of the experiments that follow, the illumination dose is specified in $\mu W/\mu m^2$, which is independent of the FOV. Note that the actual dose at the sample is lower because of losses in the objective lens and specimen. The signal is recorded on an EM-CCD camera (iXon3, Andor) as stacks of images (512 × 512 pixels) with a frame rate of 1 fps. Higher acquisition rates may be obtained with a reduced region of interest (ROI). For instance, for a ROI of 256 × 256 pixels, the signal can be recorded at 68 fps.

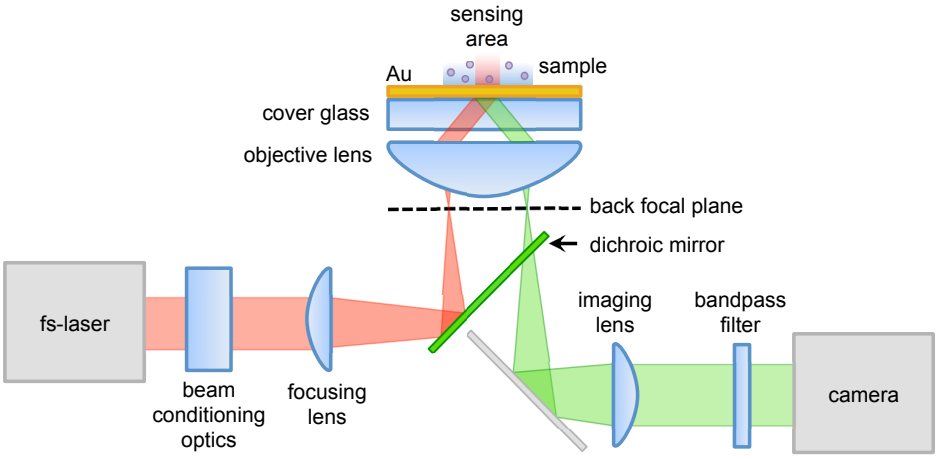

FIGURE 3.1: Schematic of the sensor device. A fs-laser beam is focused on the back focal plane of a high NA objective lens, launching an SPP field at the sensor surface. Particle binding gives rise to local two-photon excited fluorescence in the gold film, which is captured by an imaging camera.

Sensor surfaces consist of borosilicate glass coverslips (BK-7, VWR) coated with gold. Gold thin films are evaporated to a thickness of 30 nm on the coverslips, which

are pretreated with a 2 nm Cr adhesion layer. Analytes used in this experiment included gold spheres (10 nm, 20 nm, 30 nm), cholesteryl oleate droplets (Sigma Aldrich), polystyrene spheres (350 nm from Thermo Fisher), and silicon nanoparticles (30 nm, Melorium Technologies). All particle suspensions are diluted in milli-Q filtered water and sonicated before use. Lipid droplets are formed by preparing an emulsion of cholesteryl oleate with phosphatidylcholine in phosphate-buffered saline (PBS). Using $\sim$ 50 μL of a stock solution, the emulsion is subsequently drop cast on the Au-covered microscope coverslips, resulting in air-dried droplets and micrometer-sized polymorphous crystals of cholesteryl oleate on the surface. The structures were re-immersed in milli-Q filtered water before inspection with the imaging sensor. Si particles, gold spheres, and PS spheres were all diluted with deionized water and drop cast onto gold-coated coverslips.

3.3 Results

3.3.1 Detection of gold nanoparticles

We first examine the signal from a bare gold film on glass, using milli-Q filtered water as the sample. For smooth, freshly prepared films, the background signal is near or at the dark count rate of the camera, approximately 100 counts/s. This latter observation indicates that the signal from the bare gold film is very small. However, for older sensor surfaces and at higher illumination doses (up to 28 $\mu W/\mu m^2$), the signal from the bare sensor can reach 370 counts/s.

When gold nanoparticles are deposited on the sensor surface, bright spots are detected that are well above the background. A representative result is depicted in Fig. 3.2 , which shows the detected image on the camera after 20 nm gold particles are

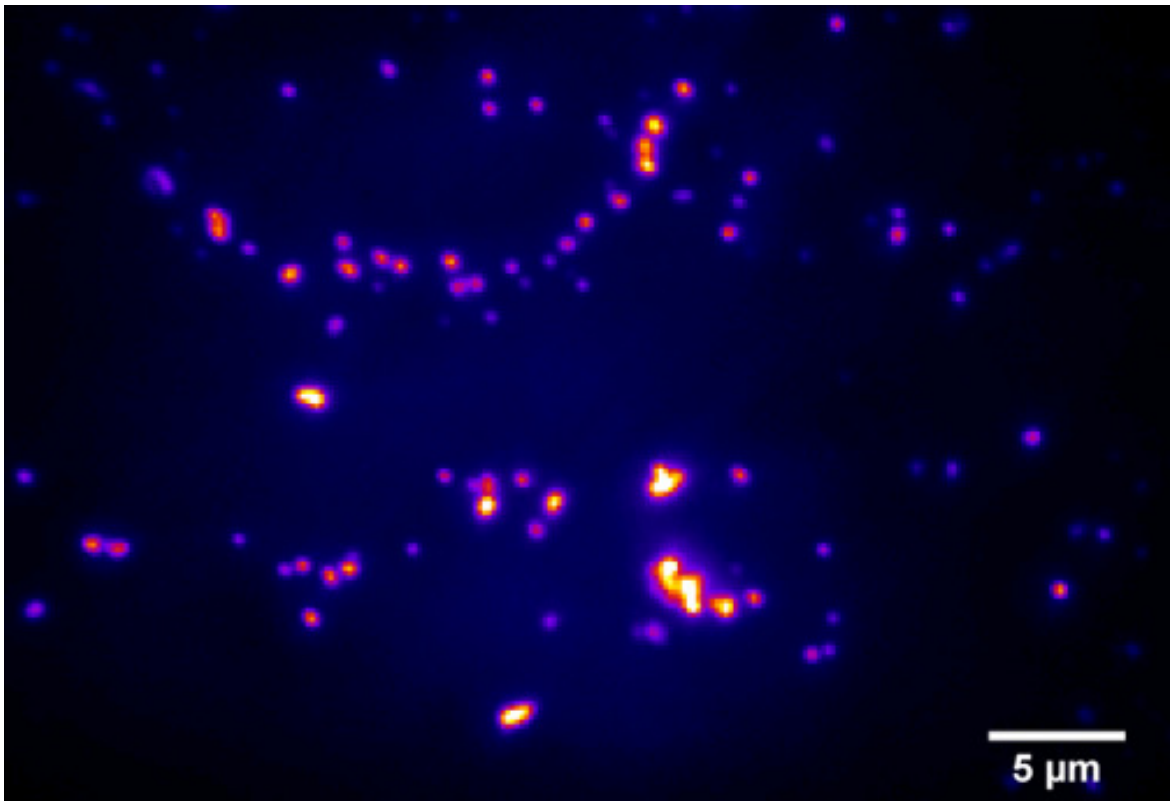

FIGURE 3.2: Gold nanospheres (20nm) adhered to the sensor surface in an aqueous medium. Average power of the illuminating beam before the objective lens is 15 mW.

physisorbed to the sensor surface from solution. The image is only visible when the incident beam is coupled to the gold film at the Kretschmann angle. Small detuning away from the coupling angle results in the disappearance of the signal. Signal is only observed when particles are adhered to the surface, particles suspended in the bulk remain invisible. We observe similar results for gold nanospheres of diameters of 10 and 30 nm.

In Fig. 3.2, the signal is accumulated over 100 raw frames taken at 68 fps by using a 256×256 ROI of the camera chip (60 μm diameter on the sensor surface) with a 15 mW beam incident on back aperture of the objective lens, corresponding to 5.3 $\mu W/\mu m^2$ average power or less than 78 $nJ/\mu m^2$ average energy for each raw frame. Signals clearly distinguishable from the background are still observed when

the illumination power is lowered. For instance, at 68 fps, average illumination powers of 5–10 mW (1.8–3.5 $\mu W/\mu m^2$) produce images with detected spots well above the background counts in each frame. When the electron-multiplying (EM) gain is used, with a gain between 25 and 300, illumination powers can be lowered to 1–2 mW (0.36–0.71 $\mu W/\mu m^2$) at the same acquisition speed.

Gold nanoparticles, which are commonly used in SPRM experiments as contrast enhancers, support localized surface plasmons. The enhanced fields associated with the surface plasmon mode can give rise to two-photon excitation of electron-hole pairs in the gold particle, followed by fluorescence emission upon electron-hole recombination.(Mooradian, 1969; Boyd, Lu, and Shen, 1986; Beversluis, Bouhelier, and Novotny, 2003) Whenever a gold nanoparticle lands on the sensor surface, the local fields are even more enhanced by the nanocavity formed between the particle and the gold layer. It is, therefore, perhaps not surprising that strong fluorescent signals from the location of the particles are observed. The results shown in Fig. 3.2 demonstrate that the nanocavities between the analyte (particle) and the gold film are efficiently excited by the SPP modes on the sensor surface, and that the resulting incoherent emission is conveniently detected by the far-field camera. Next, we examine whether similar results can be obtained for particles that do not support localized surface plasmon modes themselves.

3.3.2 Detection of semi-conducting nanoparticles

We use 30 nm silicon nanoparticles as non-metallic particles for examining the sensitivity of the sensor to nanoparticles that do not support localized surface plasmon modes. As a consequence, we expect signals that are weaker compared to the case of Au nanoparticles. Figure 3.3 shows an image of Si nanoparticles physisorbed to

the gold surface in an aqueous suspension. At power levels of 4.4 $\mu W/\mu m^2$, the particles are clearly seen. Panel 3.3 b) shows the logarithm of the fluorescence signal in the indicated region of interest, showing well resolved spots . Panel 3.3 (c) depicts the corresponding transmission image, obtained by illuminating the sample with a halogen lamp and detecting the image plane with the same camera. Although smaller ($<$ 10 nm) silicon nanoparticles and porous silicon are known to exhibit strong luminescent properties of their own(Cullis and Canham, 1991; Wilson, Szajowski, and Brus, 1993; Dubertret et al., 2002), the fluorescence from 30 nm sized Si nanoparticles is rather weak. Indeed, we did not observe any fluorescence from the Si particles when dispersed on plain glass coverslips in total internal reflection fluorescence mode under similar excitation conditions, underlining that the signal is only observed when the gold film is present. We note that the fluorescence signal is stable and does not show blinking effects characteristic of semi-conducting quantum dots.

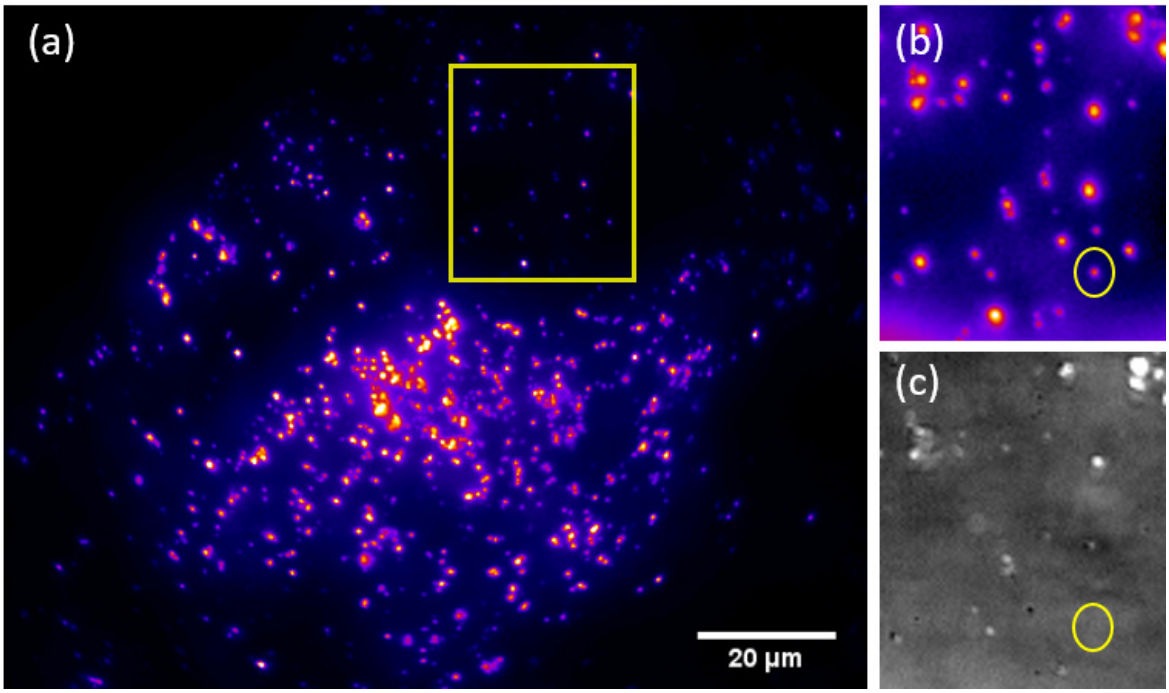

FIGURE 3.3: (a) Sensor image of 30 nm Si nanoparticles in water under illumination of $4.4\mu W/\mu m^2$. (b) Zoom of the region of interest indicated in (a). The logarithm of the signal is taken to reveal weaker emitters. (c) Transmission image of the same region of interest as in (b).

There remains the possibility that some of the bright spots observed in the signal correspond to defects in the film instead of Si particles. One method of determining the origin of the emission is to image the bare surface before introducing sample particles. The challenges in doing so is that hotspots can be very sensitive to adjustments in coupling angle, focus, and other variables that may have to be adjusted to optimize signal from particles. Meticulously monitoring of the bare film certainly complicates the usability of the sensor device. A more appealing option is to minimize the number of surface defects. One method of doing so is to use freshly cleaved mica surfaces as a substrate for the gold film. An image obtained with a mica coverslip are shown in Fig. 3.4. Clear signals are obtained with $\sim$6.9 $\mu W/\mu m^2$ incident before the objective with a sparse set of hotspots prior to the addition of

particles. The film is not mechanically robust however compared to a BK7 substrate. The mica films are easily bent and are permeated by water after a few hours of use. In future attempts with mica, the addition of a dielectric layer to the gold coating may produce more water resistant films.

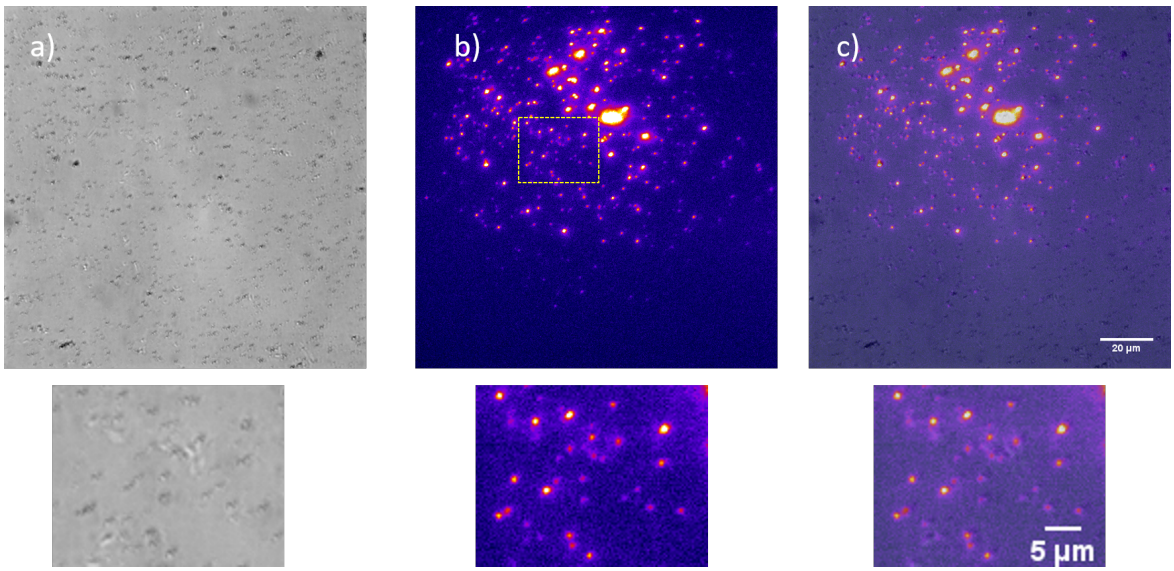

FIGURE 3.4: a) Transmission image of Si particles adhered to a 30nm Au film wiht a mica substrate. b) Signal image obtained with 100mW incident before the objective and 1 second exposures. c) An overlay of a) and b)

Another observation is the occasional appearance of interference effects which bare resemblance to artifacts seen in SPRI. The high powers used in the microscope present a challenge in filtering out excitation fields from the final image. Fig. 3.5 shows examples of how filter sets must be carefully chosen to minimize diffraction patterns. In panel a) a band pass filter centered around 540nm is placed before the camera, resulting in no interference patterns as expected for a fluorescence signal. As the band pass approaches the incident wavelength of 800nm (716/43nm), streaking patterns become visible. Presumably, the broadband femtosecond source

may have spectral tails that are able to escape filtering by the dichroic and band-pass filters resulting in interference in the far field. It is critical to limit the effects of these tails by using a long wave pass in the excitation path. This can be done with a thick glass 780 long pass filter. When the cleanup filter is removed, the interference effects become extreme as can be seen in panel c).

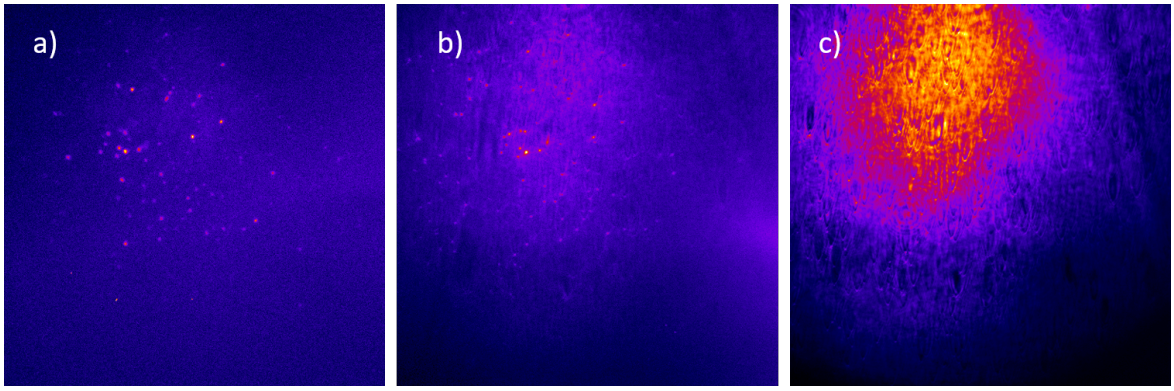

FIGURE 3.5: a) Signal image with a 540nm band pass in the emission path. b) Signal image with a 716nm band pass. c) Signal image without 780nm long pass filter in the excitation path

3.3.3 Detection of polymer particles and organic matter

Gold and silicon nanoparticles have relatively high dielectric constants, translating in strong refractive properties even when suspended in water. It is more challenging to detect objects with a refractive index closer to that of water. We perform measurements with cholesteryl oleate droplets in an aqueous medium, shown in Fig. 3.4 using $\sim$2.4 $\mu W/\mu m^2$ over an $\sim$70μm x 70μm field of view. Again, fluorescence signals are observed against a low background. The strength of the fluorescence signal can vary from film to film at similar illumination intensities, potentially due to inconsistent film quality.

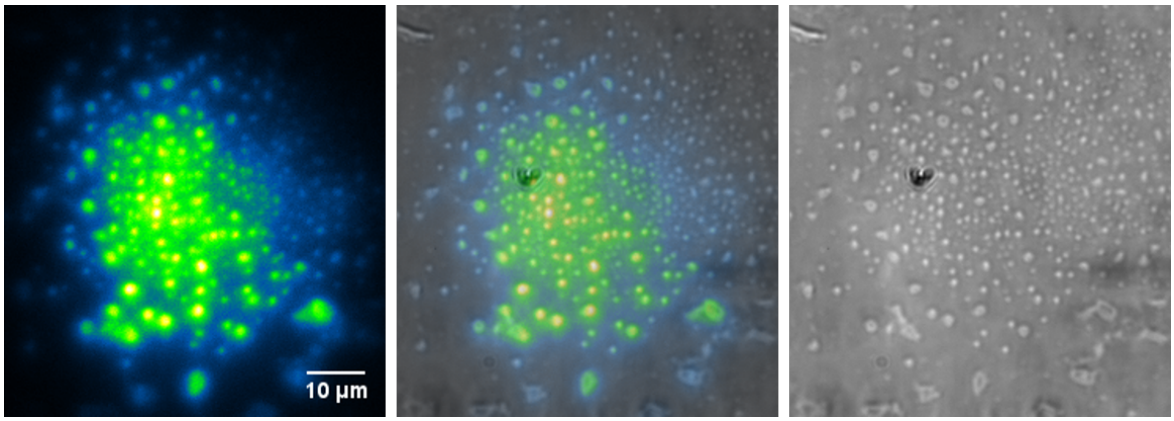

FIGURE 3.6: Cholesteryl oleate droplets adhered to the sensor surface.

We utilize polystyrene beads (350 nm) as another example of a non-fluorescent sample with a relatively low refractive index ($n \approx 1.60$). Figure 3.5 shows a two-photon excited fluorescence image of polystyrene beads adhered to the sensor surface obtained when using 150 mW of average illumination power before the objective with 1 second exposures accumulated over 20 frames ($\sim 10\ \mu W/\mu m^2$). Beads are more readily recognized in the transmission image and reveal that the signal from beads is accompanied by signal from film defects which can be brighter than the beads themselves. With lower signal to noise ratios than signals from gold particles or silicon, images more noticeably suffer from nonuniform excitation as some areas of the film do not yield a clear signal from visibly adhered beads. The power needed to generate these images are near the damage threshold for typical 30 nm gold films ($\sim$200 mW for a femtosecond source), and the weak signal that results suggests that this sample is near the current limits of the sensors detection abilities.

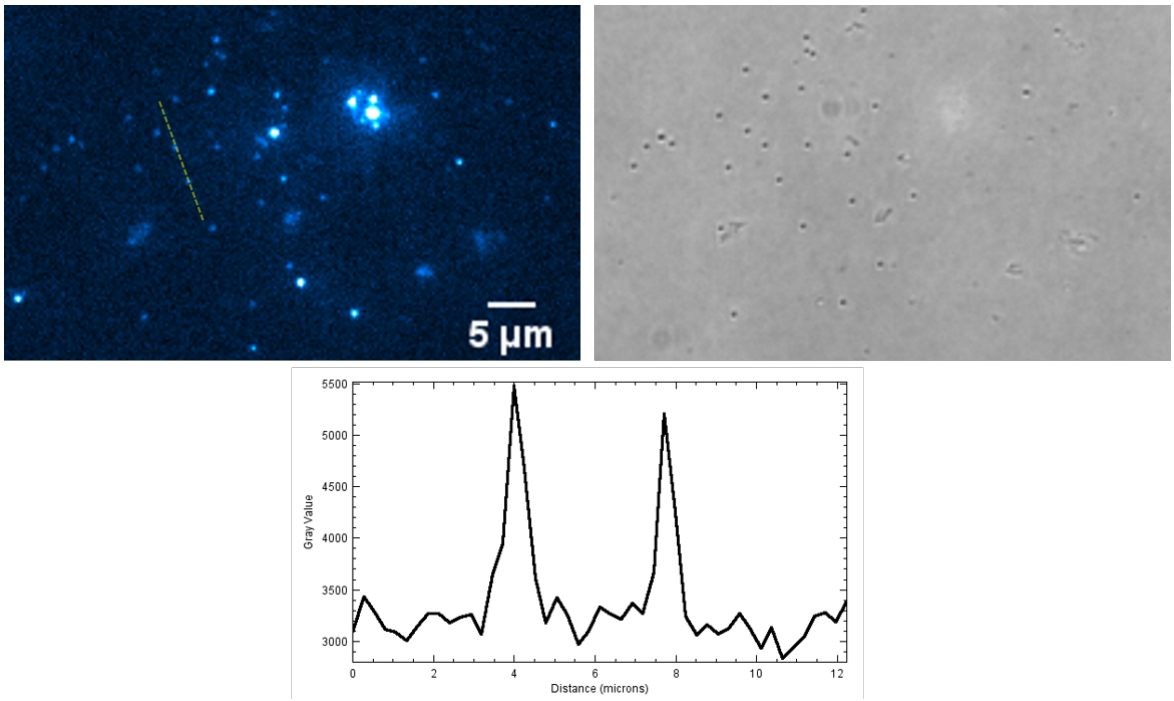

FIGURE 3.7: (a) Polystyrene beads (350 nm) suspended in water.

Fig. 3.8 shows another image of polystyrene beads. The brighter regions of the image correspond to clusters of particles while dimmer spots largely correspond to individual beads in the transmission image. Curiously, the power needed to clearly illuminate the sample was $\sim 5.2\ \mu W/\mu m^2$, nearly half of what was used in the previous PS image. The images obtained with this specific batch of coverslips display common features that are not always observed with other gold films. A patchy background luminescence is more prominent than in other films and is more noticeable in the center region of the film. A number of low intensity bright spots that do not correspond to beads in the transmission image is also observed. One difference with this particular batch of coverslips is the cleaning procedure used for the glass substrates as a sulfuric acid based cleaning detergent was used prior to deposition. Further experiments are required to determine how different cleaning methods effect the efficiency of signal generation and how they translate to the

surface properties of the gold layer.

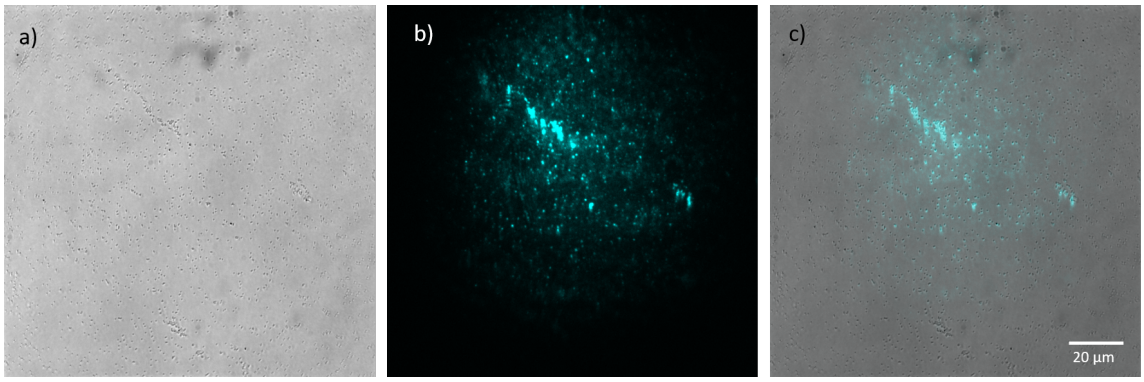

FIGURE 3.8: (a) Polystyrene beads (350 nm) suspended in water illuminated with 5.2 $\mu W/\mu m^2$

Figure 3.9 shows the dependence of the signal generated at the locations of the cholesteryl oleate droplets as the illumination power is increased. We find a power dependence close to 2, suggesting that the process responsible for the signal is indeed a two-photon excited fluorescence process. Since both polystyrene and cholesteryl oleate are non-fluorescent, the origin of the signal is not likely the particles themselves. Rather, the experiments suggest that two-photon excited fluorescence originates from the gold sensor surface itself.

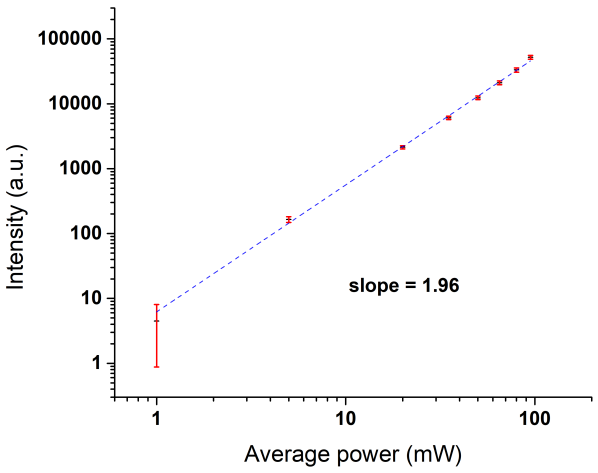

FIGURE 3.9: Magnitude of the fluorescence signal obtained from the locations of cholesteryl oleate droplets as the average power of the illuminating beam is increased. Power is measured at the back aperture of the objective lens.

3.3.4 DNA binding

One potential application for Cofefe is the detection of binding events of single strands of DNA (30A) functionalized to the sensor surface with their complementary strands (30T) bound to gold nanoparticles (40 nm Au spheres, 100 pM concentration) in solution. Real time SPRI measurements apply $\sim$1 mW to a comparable field of view and typically apply a time differencing scheme such that only diffraction patterns associated with binding events within the last exposure are displayed in a given frame. Binding events can be clearly observed in the Cofefe microscope with 25mW incident on the film and display a symmetric spot at the location of the event that is registered continuously in time. The frames below represent time steps of two minutes.

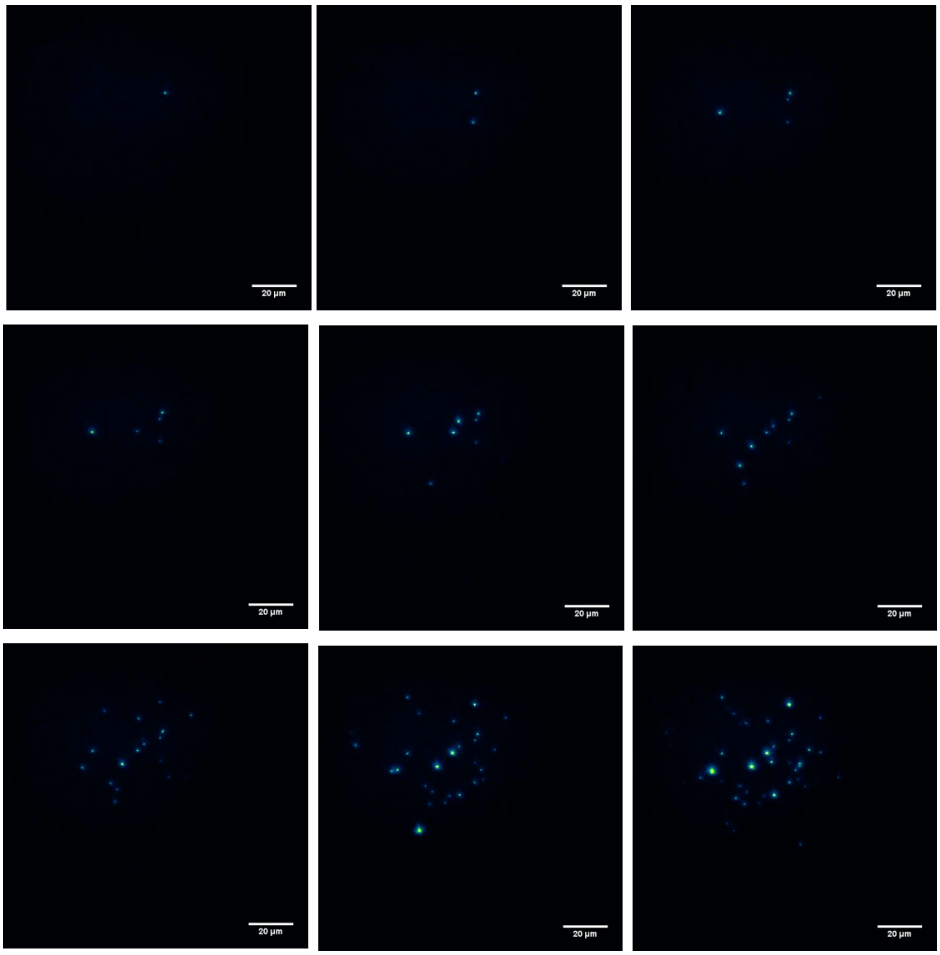

FIGURE 3.10: Binding events in time. Each frame represents a time interval of two minutes

Heat induced convection currents have been observed in the sample solution and effect the observed binding rates which occur at much longer time intervals than in SPRI with similar particle concentrations. The low powers used in SPRI produce small enough heating effects that binding rates may be attributed to the diffusion of particles through solution. In contrast, binding rates in Cofefe show a great deal of variability and occasionally results in little to no observations of binding events. Successful development of this application will require additional control and modeling of the fluid flow at the surface. The incorporation of a flow cell to the sensor surface is one potential method of mitigating heating effects. A laminar flow of

analytes over the surface would provide a clearer dependence of binding rates on particle concentration.

3.3.5 SRRF

For a sparse set of isolated emitters fitting methods can estimate fluorophore position with a single frame with high precision. For imaging applications, high spatial resolution requires a dense labeling of the sample with fluorophores which also results in a much more convoluted and often intractable fitting procedure. The multiplexing ability of optical detectors is similarly limited by the ability to spatially resolve the emission from neighboring emitters in a short period of time. A fully utilized multiplexed sensor should not only be able to localize a signal spatially but have the ability to simultaneously detect adjacent events just outside of the spatial resolution limit, yielding maximum throughput. To enhance this ability in the Cofefe microscope, improvements in spatial accuracy must be accompanied by the ability to register events with high spatial density. The incoherent radially symmetric emission pattern observed in Cofefe lends itself to existing fluorescence methods for improving spatial resolution.

Super resolution methods generally rely on the ability of a series of low resolution images to implicitly carry higher frequency information than is present in any individual low resolution frame. Super resolution methods such as PALM and STORM rely on the intermittent emission of fluorophores to localize spatial features, but the effective fluorophore in Cofefe is a spatially localized region of the gold film which radiates continuously. The Cofefe signal from nearby emitters is analogous to the high emitter density limit in conventional fluorescence microscopy, where the high density of emitters limits the ability to resolve blinking statistics from a large

background. SRRF has shown the ability to improve spatial resolution in this high density limit across a wide range of data sets by analyzing the intensity gradient fields of a series of wide field images. Assuming that the signal represents a collection of point emitters with a radially symmetric point spread function, SRRF can detect regions of higher local radial symmetry than their surroundings.(Gustafsson et al., 2016) By correlating radial symmetry maps from a sequence of raw frames, in time, SRRF provides a rapid evaluation of likely emitter positions with a single super resolution image.

The strength of the Cofefe signal allows meaningful data to be collected over very short exposure times. The high frame rates achievable in EMCCD cameras, along with the short computation time needed for SRRF analysis, can be used to generate high resolution emitter mappings with high temporal resolution. A series of 100 raw wide field frames have been used in Andor's SRRF Stream camera to produce enhanced live imaging at 1fps, suggesting that live enhanced contrast sensing may be possible for gold particles in solution.(Gustafsson et al., 2016) Figure 3.10 shows a single super resolution image of 20 nm Au particles, generated from 100 raw frames acquired at 68 fps. The SRRF algorithm was run through the nanoj SRRF plugin for ImageJ. For comparison, the SRRF signal is overlayed on the raw accumulated Cofefe image acquired over the same interval of time. Isolated emitters show a reduced FWHM of $\sim$120-140 nm and increased discrimination can be seen in regions of high density, suggesting that the inherent multiplexing ability in Cofefe may be enhanced through computational methods and displayed rapidly in time.

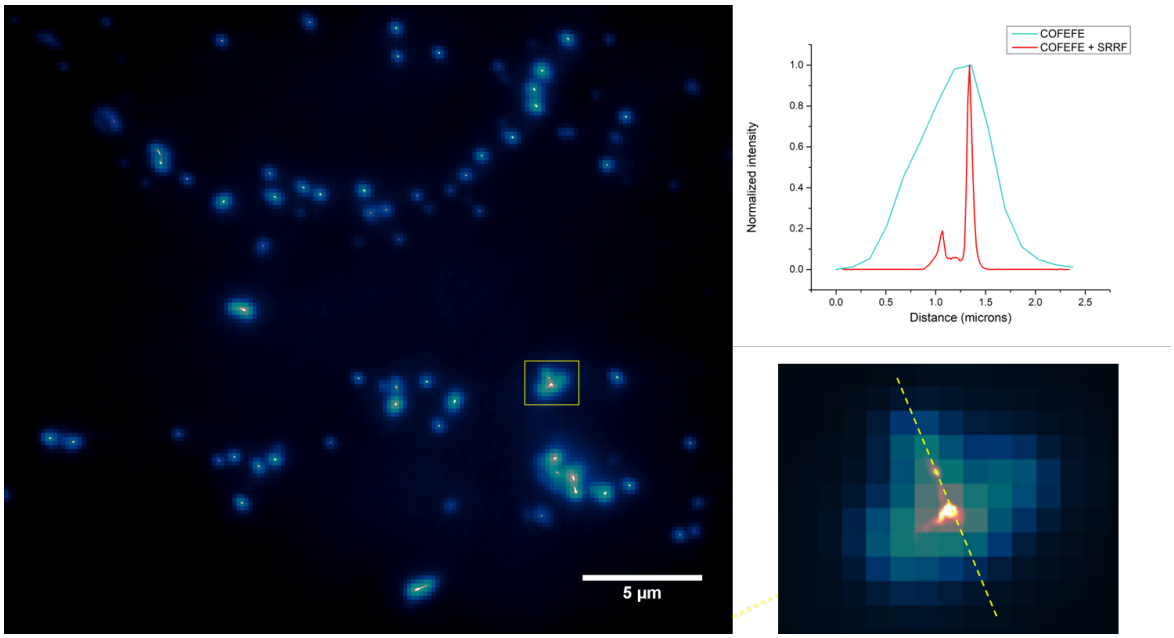

FIGURE 3.11: Overlay of Cofefe image with result after applying SRRF

3.4 Discussion

In this work, we have constructed a sensor based on the excitation of SPP modes in a thin gold film by a femtosecond laser beam. When the radiation from the film is projected onto a camera, we observe clear signals from locations where particles are in close proximity to the gold film. This radiation appears in the spectral window where we expect the two-photon excited fluorescence from gold to be prominent. The experiments described above demonstrate that this signal does not only appear for plasmonically active gold nanoparticles, but also for silicon nanoparticles, polymer beads and lipid droplets. These observations strongly suggest that the gold layer itself contributes to the detected radiation. In case of non-fluorescent particles such as polystyrene nanospheres and lipid droplets, the gold layer is expected to be the sole origin of two-photon excited fluorescence.

It is well known that electron-hole pairs can be excited by the process of two-photon absorption in gold.(Boyd, Lu, and Shen, 1986; Beversluis, Bouhelier, and Novotny, 2003) Using a near-infrared laser, electrons are excited from the d-band to the sp-band conduction band, see Fig.(a). Radiative electron-hole recombination is expected around symmetry points in the Brillouin zone where the density of states in the conduction band is high. Such a condition is found near the Fermi level of the X and L symmetry points, which correspond to radiative energies of 1.8 eV and 2.4 eV, respectively, upon recombination of momentum-matched electrons in the conduction band and holes in the valence band. In case of confined and enhanced local fields near the gold surface, both the absorption and emission rates are expected to increase, producing efficient two-photon excited fluorescence from gold.(Boyd, Lu, and Shen, 1986; Beversluis, Bouhelier, and Novotny, 2003) The formation of nano-cavities can furthermore relax the photon-momenta, enabling transitions in a broader region near the X and L symmetry points and resulting in a spectrally broadened emission.

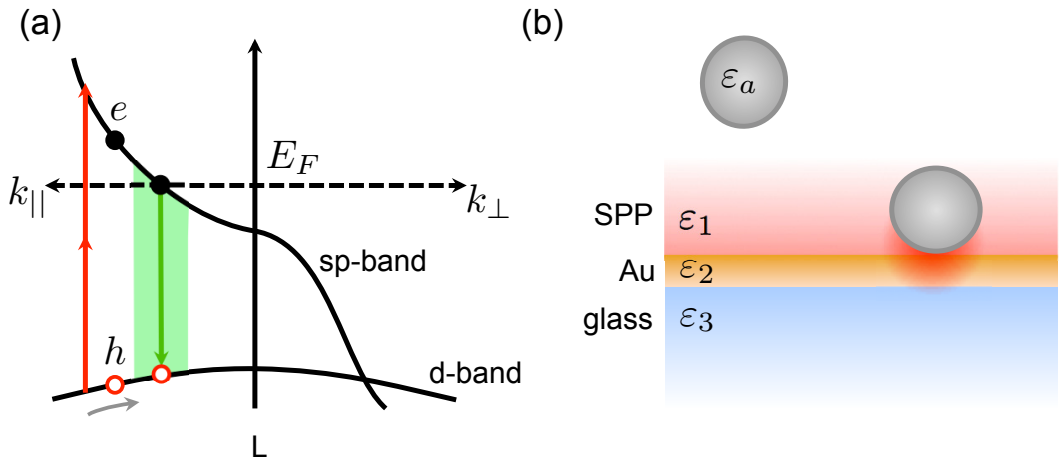

FIGURE 3.12: (a) Band structure of gold and the proposed electron-hole pair generation induced by two-photon absorption (red arrows), followed by radiative recombination (green shaded area). Dashed line denotes the Fermi level. (b) Proposed mechanism of the sensor. A particle of dielectric constant ε_a moves in an aqueous solution of dielectric constant ε_1. Upon illumination through the glass medium (ε_3), SPP modes are excited at the gold/liquid interface. Adsorption of the particle to the gold surface produces confined fields near the binding site, inducing two-photon absorption in the gold layer. Radiative electron-hole recombination is facilitated by the field confinement and the antenna properties of the gold film.

Our results confirm that the two-photon excited fluorescence of the bare smooth gold is very inefficient.(Beversluis, Bouhelier, and Novotny, 2003) Under SPP illumination conditions, the gold film itself produces a negligible amount of emission which is near the noise floor of our camera. However, whenever a nanoparticle is in the vicinity of the film, fluorescence emission is observed. This observation suggests that the confinement of the field between the gold and the particle yields local fields sufficient for two-photon excitation of electron-hole pairs in the gold, as schematically depicted in Fig. (b). This process is evidently efficient if the nanoparticle is gold, giving rise to strongly enhanced fields, but our experiments show that polymer particles or lipid droplets yield confined fields that are also capable of triggering two-photon absorption.

The subsequent emission process is furthermore enhanced by the gold film. The emission pattern observed in the back focal plane shows that the majority of the radiation couples out at the Kretschmann angle, indicating that the local polarization near the particle excites surface plasmon polaritons in the film, which subsequently couple to the far field as leakage radiation. (Gryczynski et al., 2005; Kenison et al., 2017) This latter mechanism is similar to the enhanced emission seen in SPCE microscopy. (Lakowicz et al., 2003; Gryczynski et al., 2004; Stefani et al., 2005; Borejdo et al., 2006; He et al., 2009; Lin et al., 2010; Cao et al., 2012) Previous work in SPCE microscopy has shown the utility of confined local fields to boost the optical signal generated at the gold/sample interface.(Cao et al., 2014; Cao et al., 2017) Our work extends some of the principles developed for SPCE microscopy to include signal generation in the absence of fluorophores, thus constituting a completely label-free approach. In our sensor, the gold film plays a dual role: it is the site of the optical excitation and it acts as an antenna to couple the local polarization in the form of radiation to the far-field.

The mechanism described above is consistent with our observations. We will call this mechanism confined optical field enhanced fluorescence emission, or Cofefe. The Cofefe sensor enables detection of non-fluorescent particles that physisorb to the gold sensor surface. In its current version, the sensor largely reproduces the capabilities of SPRM. However, the detected signal in Cofefe appears relative to a dark background and the detected spot exhibits a pointspread function that is based on incoherent emission and thus does not display interferences among different detected spots. In addition, the performance of the device can be improved, for instance by optimizing the pulse parameters, detection filters and quality of the gold sensing surface.

3.5 Conclusion

We have constructed a sensor that enables the detection of particles near a gold sensing surface. The optical signal is based on the two-photon excited fluorescence from the gold, enabled by the formation of confined optical fields upon binding/adsorption of the particle to the substrate. We have shown that this sensor, called Cofefe, is capable of registering non-fluorescent particles through the process of gold fluorescence. Unlike SPR-based sensors, the Cofefe method produces background-free signals and yields non-interfering and highly confined spots on the camera detector. These attributes make the Cofefe sensor an attractive candidate for label-free binding and sensing studies.

Chapter 4

Modeling coherent signals

4.1 Introduction

CARS is often implemented in a point scanning configuration where two collinear pump and Stokes beams are tightly focused on the sample plane and scanned over a region of interest. The focal volume formed by a .9 NA objective extends $\sim\lambda_p$ in the axial dimension and $\sim.4\lambda_p$ in the axial direction (Potma, Boeij, and Wiersma, 2000). In the case of incoherent processes, such as multiphoton fluorescence, the signal field intensity is expected to scale with the local intensity of the excitation field. The signal intensity should then have a spatial profile similar to that of the focal volume. In contrast, CARS shows a higher degree of signal generation in the forward direction with side lobes that extend beyond the excitation volume. A coherent buildup of signal in the axial direction of the propagating beams is apparent as the signal intensity grows along the length of the focal volume and reaches a maximum just beyond the focal plane. The coherence length established is comparable to the axial length of the focal volume, allowing forward signal buildup through the sample bulk. The distinct lateral lobes of the signal are due to diffraction of the coherent

signal and carries energy away from the optical axis (Potma, Boeij, and Wiersma, 2000).

The field produced by a nonlinear polarization in a homogeneous isotropic space can be described by a vector wave equation where $\mathbf{P^{NL}}$ denotes the nonlinear sample polarization.

$$\nabla \times \nabla \times \mathbf{E}(\mathbf{r},t) + \frac{n^2}{c^2}\frac{\partial \mathbf{E}(\mathbf{r},t)}{\partial t^2} = -\frac{4\pi}{c^2}\frac{\partial^2 \mathbf{P^{NL}}(\mathbf{r},t)}{\partial t^2} \tag{4.1}$$

In terms of the monochromatic anti-stokes frequency, and the assumption of a slowly varying amplitude approximation, the third order CARS signal may be represented implicitly in the following way.

$$\nabla \times \nabla \times \mathbf{E}_{as}(\mathbf{r}) - k_{as}^2 \mathbf{E}_{as}(\mathbf{r}) = \frac{4\pi\omega_{as}^2}{c^2}\mathbf{P^3}(\mathbf{r}) \tag{4.2}$$

An explicit expression for the CARS anti-stokes electric field can be determined through knowledge of an appropriate Greens function. Considering a homogeneous isotropic space, the scalar response of the electrical vector potential to a point source of current can be derived, the scalar Greens function G_0. The response has the form of a spherical wave that propagates outward from the source. To account for the non-scalar nature of the induced electrical fields, the full dyadic Greens function is required.

$$\mathbf{E}_{as}(\mathbf{r}) = -\frac{4\pi\omega_{as}}{c^2}\int_V dV \left(\hat{I} + \frac{\nabla\nabla}{k_{as}^2}\right) G_0\left(\mathbf{r},\mathbf{r}'\right)\mathbf{P}^{(3)}(\mathbf{r}') \tag{4.3}$$

The CARS radiation field induced by the oscillating third order polarization may be expressed in the form of equation 1.3, where the term $\left(\hat{I} + \frac{\nabla\nabla}{k_{as}^2}\right) G_0$ represents

the dyadic Green's function. By integrating field contributions over a discrete set of dipoles at locations $\mathbf{r}'$ to a given observation point $\mathbf{r}$, coherent interference effects from an arbitrary sample geometry can be modeled.(Cheng, Volkmer, and Xie, 2002)

Green's function analysis has shown that sample size and geometry must be taken into consideration when determining the amount of signal scattered into the forward vs backward direction(Cheng, Volkmer, and Xie, 2002). For spherical sample volumes with diameters much less than the excitation wavelength, the emission pattern resembles that of a Hertzian dipole with a minimum along the polarization axis of the incident fields. As the sample grows in volume, the coherent nature of the signal becomes clear as the forward CARS signal grows drastically relative to the epi-CARS signal. This is due to the phase matching conditions in each direction, allowing constructive interference in the forward direction and destructive in the backward direction. Thin rod structures parallel to the optical axis and thin disks of the same volume can show very different emission patterns as rods scatter almost entirely in the forward direction while disks show strong scattering in the backward direction, comparable to the forward intensity. The thin dimension of the disk reduces the degree of interference effects along the propagation axis and allows for greater epi-directed signal.

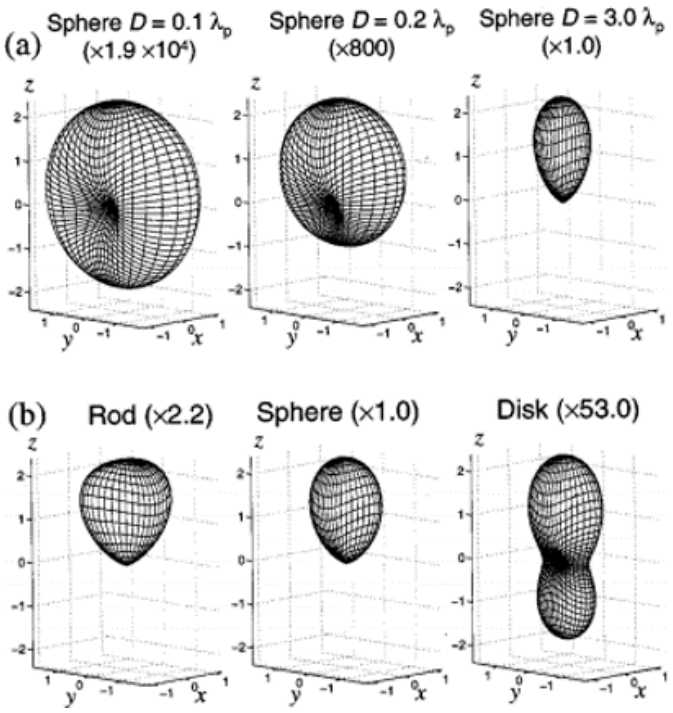

FIGURE 4.1: a) Far-field CARS radiation pattern from spherical scatterers centered at the focus with different diameters. b) Far-field CARS radiation pattern from scatterers centered at focus with the same volume but different shapes (rod, sphere, and disk). The rod has diameter of .2 λ_{pump} and an axial length of 2 λ_{pump}. The sphere has a diameter of .78 λ_{pump}. The disk has a diameter of .89 λ_{pump} and a thickness of .1 λ_{pump}. Shown in parentheses are the intensity ratios between samples of different sizes and different shapes. The radiation field is polarized along the x-axis. The signals were calculated with the assumption of tightly focused (NA = 1.4) incident beams copropagating along the +z axis and polarized along the x axis. Adapted from (Cheng, Volkmer, and Xie, 2002) Copyright 2002 by OSA

Epi-detection has the appeal of overcoming the issue of nonresonant contributions from solvents in the focal volume which may contribute strongly in the forward direction. Small sample volumes generate nearly isotropic signals which contribute equally to each path, but appear against a reduced background in epi-detection.

Another contrast mechanism illuminated through a dipole model is signal generation at interfaces (Cheng, Volkmer, and Xie, 2002) which may result from the geometry of the interface itself, or from back scatter of the forward CARS signal due to an index mismatch in the sample.

A similar description of coherent nonlinear signal generation is desired for SPP enhanced CARS signals. The drastic difference in excitation fields requires new consideration of phase matching conditions for a signal propagating on the surface. Also, the addition of a gold thin film to the focal volume complicates the optical response of emitters which may interact non-trivially with the film before propagating to a far field detector.

4.2 Methods

4.2.1 Angular spectrum representation

Exciting a dipole with surface plasmon polaritons near a gold interface enhances the role of near fields in the detected far field signal generated by the sample. While evanescent contributions are not expected to be a factor in traditional CARS emission, they may play a very tangible role in surface enhanced implementations. An angular spectrum representation for the fields in terms of evanescent and plane waves provides a convenient basis for examining the coupling of near fields to propagating modes in the far field.

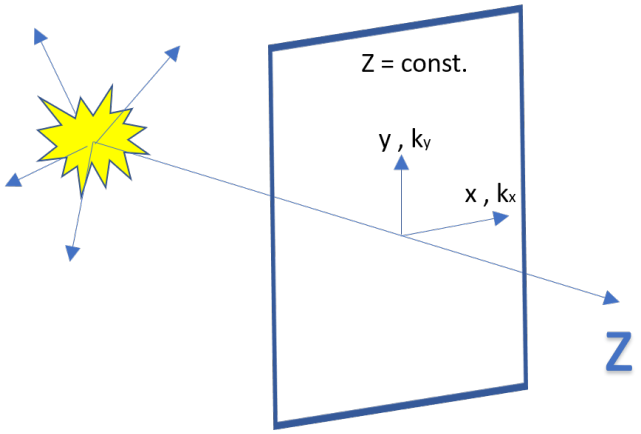

FIGURE 4.2: Coordinate system used to describe fields propagating away from a source along the optical axis z. For a given z-value, the fields may be described by a real space or momentum space representation.

We define the optical axis of a propagating plane wave as the z-axis. For any propagation distance from the source along the optical axis, we can decompose the field in the plane perpendicular to the axis. We can relate the spatial amplitudes and spatial frequencies of the electric field on this plane through a Fourier transform.

$$\mathbf{E}(x,y,z) = \int\int_{-\infty}^{\infty} \hat{\mathbf{E}}(k_X,k_y;z)e^{i[k_x x+k_y y]}dk_x dk_y \tag{4.4}$$

Defining $k_z = \sqrt{k^2 - k_x^2 - k_y^2}$, the evolution of the spectral content of the fields along the optical axis is represented by the propagation factor $e^{\pm ik_z z}$ allowing an expression of $\mathbf{E}$ in terms of the FT at z=0.

$$\mathbf{E}(x,y,z) = \int\int_{-\infty}^{\infty} \hat{\mathbf{E}}(k_x,k_y;0)e^{i[k_x x+k_y y\pm k_z z]}dk_x dk_y \tag{4.5}$$

Conveniently, in any given plane along the given optical axis, we may use the momentum space representation to distinguish freely propagating and evanescent components of the field. Wave vectors with an inplane magnitude less than or equal to the free space wave vector k correspond to plane waves while evanescent waves have an inplane magnitude greater than k. Without evanescent contributions, far field points corresponding to distinct emission angles of a homogeneous space establish a direct correspondence with plane waves from the source spectrum. To convey near field information to the far field a spectral shift of the source spectrum is required and may be achieved in an inhomogeneous space.

If the source is near an interface, we may characterize its interaction with the source fields through a transmission function T across the boundary representing the inhomogeneity. The far fields resulting from the product of the source fields with T represent a convolution in Fourier space. As a result, large spatial frequencies of the source and transmitted fields form linear combinations that correspond to plane waves in the far field. The contribution of evanescent fields to the angular emission spectrum is demonstrated visually below.

4.2.2 Green's functions for layered planar media

Dyadic Green's functions are determined by the linear relation between an electric field due to a point source of current and the corresponding oscillating dipole $\vec{\mu}$ generating the field. Theoretically, knowledge of the appropriate Green's function allows a simple expression for the response of a system at point r to a given source containing r' by integrating the product of the Green's function and source over the source volume.

$$\mathbf{E}(r) = \omega^2 \mu \mu_0 \overline{\mathbf{G}}\left(\mathbf{r}, \mathbf{r}'\right) \vec{\mu} \tag{4.6}$$

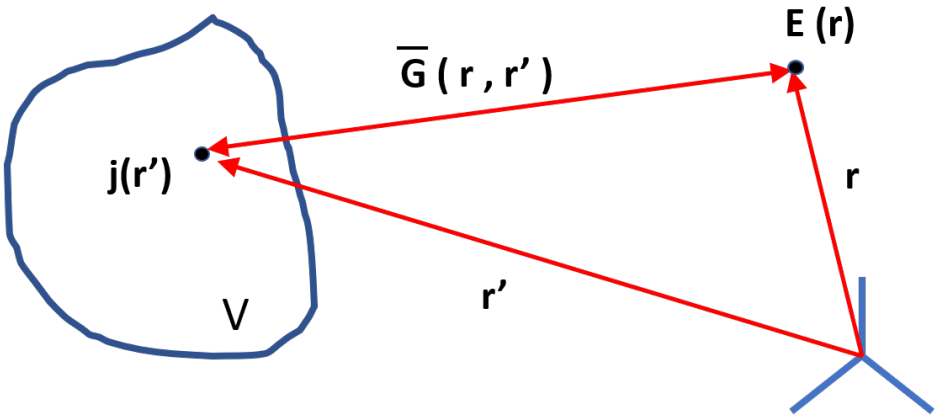

FIGURE 4.3: Notation used for Green's function calculations. A point source component of a volume source V is located at the coordinate r'. The Greens function $\overline{G}$ relates the electrical response of the system at the field point r due the point source at r'.

While the electric field response to a point source requires a tensor expression, the vector potentials, $\mathbf{A}(\mathbf{r})$, are proportional to the scalar Greens function which takes on the form of a propagating spherical wave.

$$\mathbf{A}(\mathbf{r}) = -\frac{k_1^2}{i\omega\epsilon_0\epsilon_1}\frac{e^{ik|\mathbf{r}-\mathbf{r}'|}}{4\pi|\mathbf{r}-\mathbf{r}'|} = -\frac{k_1^2}{i\omega\epsilon_0\epsilon_1}\mathbf{G_0}(\mathbf{r},\mathbf{r}') \tag{4.7}$$

$$\mathbf{G}_0(\mathbf{r},\mathbf{r}') = \frac{e^{ik|\mathbf{r}-\mathbf{r}'|}}{4\pi|\mathbf{r}-\mathbf{r}'|} \tag{4.8}$$

The vector potential can be expressed in an angular spectrum representation by applying the Weyl identity, eq. 4.9, where k_{z_1} is the longitudinal component of wave vector k_1 along the chosen optical axis.

$$\left(\frac{e^{ik\sqrt{x^2+y^2+z^2}}}{\sqrt{x^2+y^2+z^2}} = \frac{i}{2\pi} \int \int_{-\infty}^{\infty} \frac{e^{ik_x x + ik_y y + ik_z |z|}}{k_z} dk_x dk_y \right) \tag{4.9}$$

$$\mathbf{A}(\mathbf{r}) = \text{-} \frac{k_1^2}{8\pi^2 \omega \epsilon_0 \epsilon_1} \int \int_{-\infty}^{\infty} \frac{e^{ik_x(x-x_0)+ik_y(y-y_0)+k_{z_1}|z-z_0|}}{k_{z_1}} dk_x dk_y \tag{4.10}$$

The task remains to establish a linear relationship between the electric fields and the source dipole in an angular spectrum representation. Under a Lorentz gauge, expressions for the electric field may be obtained from $\mathbf{A}(\mathbf{r})$ as;

$$\mathbf{E} = i\omega[1 + \frac{1}{k_1^2} \nabla\nabla\cdot]\mathbf{A} \tag{4.11}$$

Comparison with equation 4.6 then identifies the dyadic Green's function for an isotropic homogeneous space. The signs of the entries in the matrix M correspond to propagating waves in the upper halfspace and lower halfspace of the chosen coordinate system.

$$\overline{\mathbf{G}}(\mathbf{r}, \mathbf{r}') = \frac{i}{8\pi^2} \int \int_{-\infty}^{\infty} \overline{\mathbf{M}} \frac{e^{ik_x(x-x_0)+ik_y(y-y_0)+k_{z_1}|z-z_0|}}{k_1^2 k_{z_1}} dk_x dk_y \tag{4.12}$$

$$\overline{\mathbf{M}} = \begin{bmatrix} k_1^2 - k_x^2 & -k_x k_y & \mp k_x k_{z_1} \\ -k_x k_y & k_1^2 - k_y^2 & \mp k_y k_{z_1} \\ \mp k_x k_{z_1} & \mp k_y k_{z_1} & k_1^2 - k_y^2 \end{bmatrix} \tag{4.13}$$

To extend to the case of a nonhomogeneous, multi-layered space, each plane wave must be multiplied by the corresponding Fresnel coefficient to incorporate the reflection and transmission through different index layers. Here we consider two

dielectric halfspaces that sandwich a thin metallic layer of thickness d. To simplify this procedure it is beneficial to separate the Green's function into p and s polarization components. This can be accomplished through a partition of the matrix $\overline{\mathbf{M}}$, where $\overline{\mathbf{M}}^s$, and $\overline{\mathbf{M}}^p$ denote the s and p polarization components of the Green's function respectively.

$$\overline{\mathbf{M}}^s = \begin{bmatrix} k_y^2 & -k_x k_y & 0 \\ -k_x k_y & k_x^2 & 0 \\ 0 & 0 & 0 \end{bmatrix} \tag{4.14}$$

$$\overline{\mathbf{M}}^p = \begin{bmatrix} k_x^2 k_{z_1} & k_x k_y k_{z_1} & \mp k_x (k_x^2 + k_x^2) \\ k_x k_y k_{z_1} & k_y^2 k_{z_1} & \mp k_y (k_x^2 + k_x^2) \\ \mp k_x (k_x^2 + k_x^2) & \mp k_y (k_x^2 + k_x^2) & (k_x^2 + k_x^2)/k_{z_1} \end{bmatrix} \tag{4.15}$$

For an epi-detected signal we are interested in modeling the emission in to the lower halfspace from a dipole located in the upper halfspace. The far-field Green's function that relates a wave emitted at point $\mathbf{r}'$ in the upper halfspace through a layered medium to a far-field point $\mathbf{r}$ in the lower halfspace, is given in the angular spectrum representation as Novotny and Hecht, 2012:

$$\overline{\mathbf{G}}(\mathbf{r}, \mathbf{r}') = \frac{e^{ik_n(r+dz/r)}}{4\pi r} \times e^{\left\{-ik_1\left(\frac{x'x}{r} + \frac{y'y}{r} - z'\sqrt{1 - \frac{n_3^2}{n_1^2}\frac{\rho^2}{r^2}}\right)\right\}} \times \overline{\mathbf{M}} \tag{4.16}$$

where the matrix $\overline{\mathbf{M}}$ is given as:

$$\overline{\mathbf{M}} = \begin{bmatrix} \frac{x^2}{\rho^2}\frac{z^2}{r^2}\Phi_3^{(2)} + \frac{y^2}{\rho^2}\Phi_3^{(3)} & \frac{xy}{\rho^2}\frac{z^2}{r^2}\Phi_3^{(2)} - \frac{xy}{\rho^2}\Phi_3^{(3)} & \frac{-xz}{r^2}\Phi_3^{(1)} \\ \frac{xy}{\rho^2}\frac{z^2}{r^2}\Phi_3^{(2)} - \frac{xy}{\rho^2}\Phi_3^{(3)} & \frac{y^2}{\rho^2}\frac{z^2}{r^2}\Phi_3^{(2)} + \frac{x^2}{\rho^2}\Phi_3^{(3)} & \frac{-yz}{r^2}\Phi_3^{(1)} \\ \frac{-xz}{r^2}\Phi_3^{(2)} & \frac{-yz}{r^2}\Phi_3^{(2)} & (1 - \frac{z^2}{r^2})\Phi_3^{(1)} \end{bmatrix} \tag{4.17}$$

Here $\rho = \sqrt{x^2 + y^2}$ and the functions $\Phi_3^{(i)}$ with $i = (1, 2, 3)$ are written as:

$$\Phi_3^{(1)} = t^p(k_\rho)\frac{n_3}{n_1}\frac{k_3 z/r}{\sqrt{k_1^2 - k_\rho^2}} \tag{4.18}$$

$$\Phi_3^{(2)} = -t^p(k_\rho)\frac{n_3}{n_1} \tag{4.19}$$

$$\Phi_3^{(3)} = t^s(k_\rho)\frac{k_3 z/r}{\sqrt{k_1^2 - k_\rho^2}} \tag{4.20}$$

where $k_\rho = k_1\rho/r$ and t^p and t^s are the generalized Fresnel coefficients for s and p polarized light, respectively. The generalized transmission and reflection coefficient for the water-gold-glass stratified medium considered here are:

$$t^{(p,s)} = \frac{t_{1,2}^{(p,s)} t_{2,3}^{(p,s)} e^{(ik_{2z}d)}}{1 + r_{1,2}^{(p,s)} r_{2,3}^{(p,s)} e^{(2ik_{2z}d)}} \tag{4.21}$$

$$r^{(p,s)} = \frac{r_{1,2}^{(p,s)} + r_{2,3}^{(p,s)} e^{(2ik_{2z}d)}}{1 + r_{1,2}^{(p,s)} r_{2,3}^{(p,s)} e^{(2ik_{2z}d)}} \tag{4.22}$$

where d is the thickness of the gold layer. The expressions in Eqs. 4.21–4.22 depend on the Fresnel coefficients at each of the interfaces as:

$$r_{i,j}^s(k_\rho) = \frac{\mu_j k_{z_i} - \mu_i k_{z_j}}{\mu_j k_{z_i} + \mu_i k_{z_j}} \tag{4.23}$$

$$r_{i,j}^p(k_\rho) = \frac{\varepsilon_j k_{z_i} - \varepsilon_i k_{z_j}}{\varepsilon_j k_{z_i} + \varepsilon_i k_{z_j}} \tag{4.24}$$

and

$$t_{i,j}^s(k_\rho) = \frac{2\mu_j k_{z_i}}{\mu_j k_{z_i} + \mu_i k_{z_j}} \tag{4.25}$$

$$t_{i,j}^p(k_\rho) = \frac{2\varepsilon_j k_{z_i}}{\varepsilon_j k_{z_i} + \varepsilon_i k_{z_j}}\sqrt{\frac{\mu_j \varepsilon_i}{\mu_i \varepsilon_j}} \tag{4.26}$$

4.3 Results

A point dipole model provides insight in to the mechanisms involved in the SPP excited dipole emission process. The presence of an interface significantly alters the familiar dipole radiation pattern observed in a homogeneous space. Emission into the lower halfspace is concentrated in to specific angles at or above the critical angle for total internal reflection. The resulting emission cone also displays the coupling of near field radiation to the far field.

In free space, evanescent fields are unable to propagate away from their source. The addition of a thin layer between to halfspaces allows the conversion of evanescent fields to propagating waves in the opposing halfspace via an optical tunneling effect through the thin layer. In the special case of an SPP supporting thin layer, another outcoupling mechanism becomes possible for evanescent fields near the interface. The large k vectors of radiating dipoles near the interface have the ability to couple to SPP modes at the surface and propagate radially away from the source, leaking radiation at the Kretschmann angle as they propagate. In Figure 4.5a), emission into the lower halfspace are shown for a dipole in air, 1 nm above a 30 nm gold film with a glass lower halfspace. In the case of a glass/gold/air interface, the critical angle and Kretschmann angle are very near one another and appear as a single emission cone in Fig. 4.5. The evanescent contribution decreases as the dipole is placed further from the interface due to a reduced intensity of the SPP excitation fields as well as a greater barrier for the dipole field to interact with the gold surface.

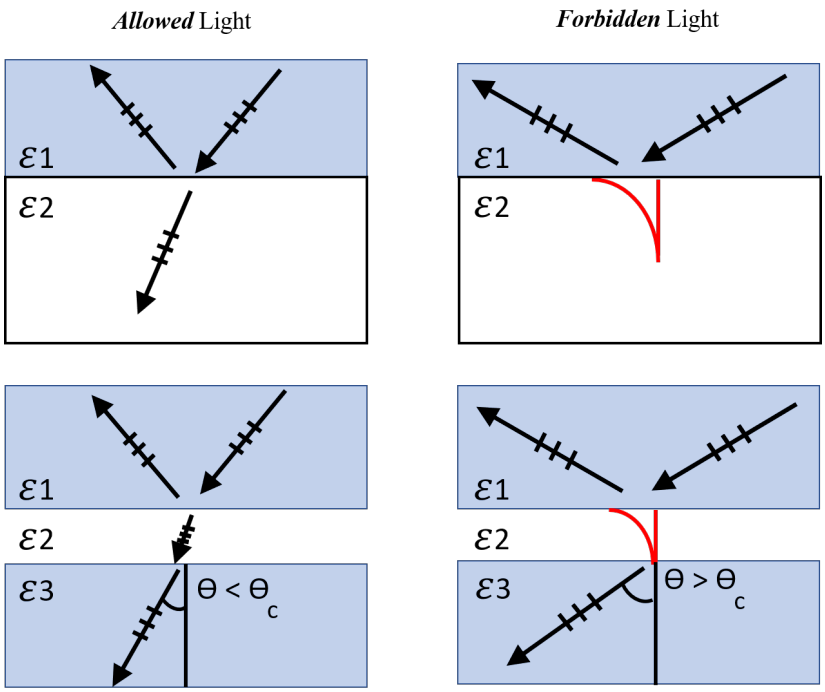

FIGURE 4.4: On the left, "allowed" light is displayed for an interface between two halfspaces and two halfspaces seperated by a thin layer. In both cases, incident fields emerge as propagating waves in the lower halfspace at emission angles less than the critical angle for total internal reflection. On the right, incident rays are beyond the critical angle. In the case of a single interface the resulting evanescent field is confined to the near field. With a thin layer, evanescent fields are able to tunnel through the layer and emerge as propagating waves ,"forbidden" light, in the lower halfspace at angles beyond the critical angle. This figure is adapted from (Novotny and Hecht, 2012) Copyright Cambridge University Press

We expect plane waves emanating from the dipole source to penetrate the thin film layer in accordance with generalized Fresnel coefficients. Having a smaller wave vector than evanescent fields at the source, their emission angle is correspondingly less. In Fig. 4.5, transmitted plane waves are registered as non-zero intensity values at angles within the critical cone angle. A zero in intensity is seen directly at the center of the cone, corresponding to plane waves that encounter the interface

at normal incidence. The absence of such a contribution to the detected radiation is expected from the familiar donut shape of a Hertzian dipole in a homogeneous space, where a zero in emission is seen along the oscillation axis of the dipole. It is clear from the figure that the greatest detected intensity is expected near the critical angle and that freely propagating "allowed" light represents a less intense contribution spread over a larger range of emission angles. With a 1 nm spacing between the dipole and the metallic layer, evanescent fields are able to penetrate the film and reemerge as propagating waves. This contribution to the total emission can be seen as the small hump on the top of the emission cone above the critical angle. For surface bound samples, "forbidden" light contributions from evanescent fields must be taken into account.

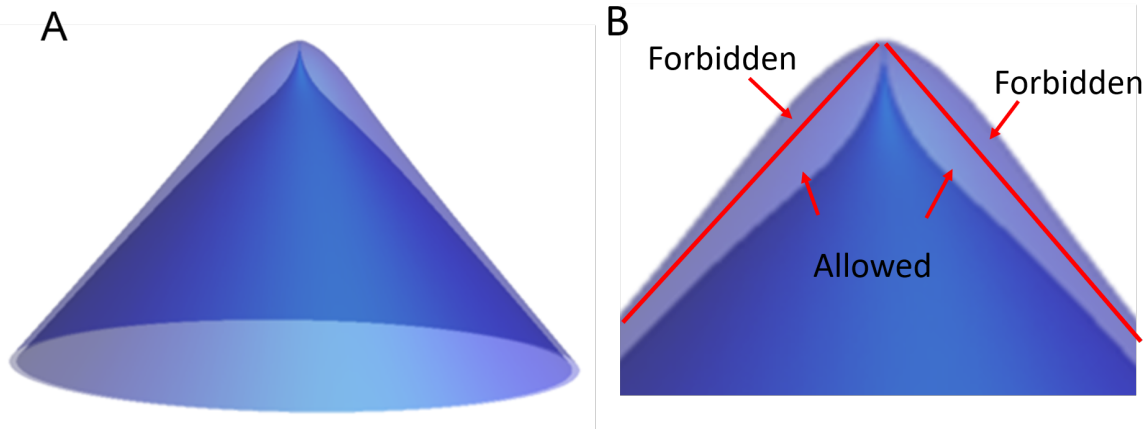

FIGURE 4.5: a) Angular intensity distribution of emission into the lower halfspace for a dipole 1 nm above a 30 nm gold layer which separates air and glass halfspaces. b) Light above the critical angle for total internal reflection correspond to evanescent fields generated by the dipole

A useful way to visualize the distribution of emitted photon momentum is through back focal plane images. A collimated laser beam entering the back aperture of a

high NA objective will be focused to a point on the sample plane. Conversely, a dipole at the sample plane emitting a cone of light into the objective will result in a collimated beam emerging from the back aperture of the objective. A horizontal cross section through this beam produces a back focal plane image of the signal. The spatial distribution of light intensity on this two dimensional plane can be mapped to a momentum space distribution by simply projecting the x,y-axes on to the k_x, k_y-axes.

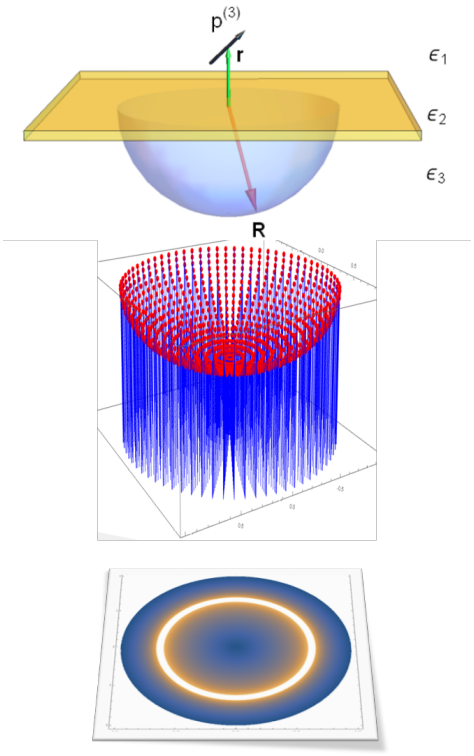

FIGURE 4.6: Back focal plane images are formed by recording emission intensity at a distance R from the origin in the glass lower halfspace. The recorded field values are then projected to a plane parallel to the gold film.

In a wide field imaging mode, the illuminating beam is focused on to the back focal plane of the objective, resulting in a collimated beam emerging from the objective

onto the sample plane. Dipole emission cones are then collected by the objective and focused to an image plane on a CCD camera. To produce a back focal plane image on the camera, a Bertrand lens must be placed in the detection path to re-collimate the dipole emission. Computationally, we may reproduce the back focal plane image by first recording field values on a glass hemisphere in the lower half-space as is done for the emission patterns in 4.5 and 4.7. The field values may then be projected to a plane parallel to the interface with intensity values plotted on the plane. The momentum distribution of emitted photons are clearly mapped and the nature of the dipole oscillation can be inferred. Dipole oscillations perpendicular to the interface result in a solid ring as is the case for a gold thin film excited at near-IR wavelengths. If the gold film is replaced with a silver film, the surface fields have a relatively large field component in the plane of the film relative to the out of plane component. The resulting emission pattern displays a clear angular node which aligns with the orientation of the horizontally oscillating dipole.

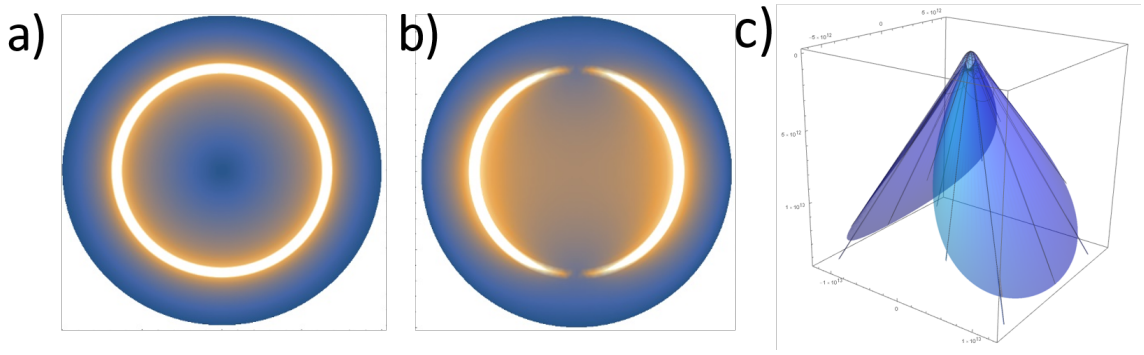

FIGURE 4.7: Comparison of the back focal plane images that result for a dipole above a (a) gold or (b) silver SPP supporting layer. (c)Angular intensity distribution of emission into the lower halfspace for a dipole 1 nm above a 30 nm silver layer which separates air and glass halfspaces. The dipole oscillation is largely in-plane and the prominent lobes are perpendicular to the oscillation direction.

Coherent emission from multiple dipoles at the surface results in interference effects in the back focal plane and image plane. To model interference between two dipoles, Electric field values for each dipole individually can be added and recorded at each far field detection point. The intensity distribution obtained by squaring this sum at each detection point clearly shows interference between distinct emitters in the back focal plane image, shown as an inset in 4.8a). A benefit of an angular spectrum representation is the simple relation between momentum space, and real space representations of the fields. By applying a Fourier transform to the momentum space distribution, a real space image of the fields is obtained.

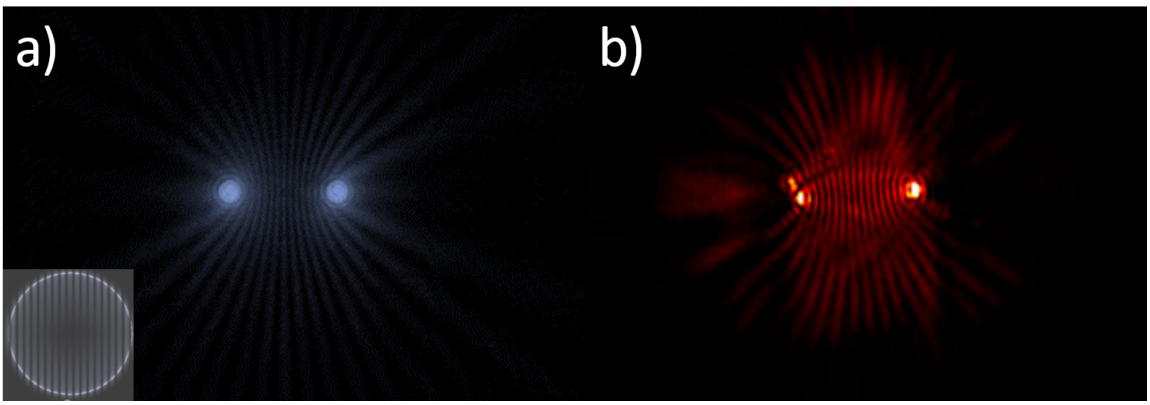

FIGURE 4.8: a) Interference pattern observed from two Si particles that act as coherent sources of a 4WM signal.b) Simulated interference between two point dipoles separated by 5 microns. The inset displays the corresponding interference pattern expected in a back focal plane image. Figure b) is adapted from (Liu, Wang, and Potma, 2011) Copyright 2011 OSA

In Fig. 4.8 b) an image by Liu et al. displays interference fringes between two neighboring emitters. Two (200 nm) Si particles on a gold film were used to mediate a coherent 4WM signal induced by two incident SPP fields. The generated mixing signal at the particles then couples to SPP modes, propagating radially from each emitter. The interaction of these coherent fields is monitored through leakage radiation through the metallic film. Fig. 4.8 a) shows a simulated real space image of the

interference pattern expected for two dipoles above the gold film using the Green's function formalism above. The ability of the simulated image to faithfully capture the experimentally observed coherence effects offers motivation for the modeling of extended samples with a dense set of discrete dipoles.

4.4 Conclusion

Dipole models provide useful insights into coherent signal generation in continuous samples. In a tightly focused CARS configuration, dipole models reveal several underlying contrast mechanisms for epi-detected CARS (Cheng, Volkmer, and Xie, 2002). Dipole arrangements with overall spatial dimensions that are small relative to the incident wavelength behave much like Hertzian dipoles in a homogeneous space and can display coherent artifacts within the focal volume in traditional CARS. To develop an analogous model for dipoles excited by SPP fields, the role of the gold film must be considered. Not only does the film support the excitation fields, but it also acts as an emission antenna with a drastically different angular profile than a free space dipole. Strong emission at the Kretschmann angle suggests that dipoles near the film are able to excite SPP modes at the gold surface. Previous observations (Liu, Wang, and Potma, 2011) point to a coherent interaction among distinct emitters, resulting in interference effects which can be simulated with a point dipole model that incorporates the optical properties of the film through generalized Fresnel coefficients.

Excitation by SPP fields in a Krestchmann configuration presents different phase matching conditions than in the tight focusing case. The momentum of the incident fields is converted to surface modes propagating orthogonal to the optical axis of the objective. In this case, momentum conservation can be achieved with a signal

which also propagates along the interface. Reciprocity arguments suggest that this propagating surface mode may also take on the form of an SPP. To detect the signal in the far field, a portion of it must be redirected back into the objective. Momentum matching requires that this portion of the signal emerges at the Kretschmann angle in the lower halfspace and is associated with SPP leakage radiation. As the signal is generated along the interface, we expect a coherent buildup of signal for extended samples along the propagation direction of the SPP fields.

The dependence of far field intensity on emission angle can be coarsely predicted by phase matching conditions, but it does not provide information on the imaging properties of the coherent signal. With a discrete set of dipoles, interference phenomenon are easily explored over different dipole configurations in real space and momentum space by summing their field contributions on a simulated detection grid. In this manner, it is straight forward to simulate the imaging properties of SPP mediated 4WM experiments.

Chapter 5

SECARS

5.1 Introduction

The success of laser-scanning CRS on the one hand, and surface-enhanced CRS on the other, suggests the feasibility of SPP-based coherent Raman microscopy. Indeed, recent studies have shown that SE-CARS images of lipid droplets can be generated in the wide-field imaging mode using a gold film as the plasmonic material (Fast et al., 2016). The amplifying properties of the gold film were found to be sufficient to produce images at rates that are comparable to laser-scanning CRS microscopy. These developments insinuate that surface-enhanced CARS microscopy of cells is possible, offering a route to examine the cortical regions of cells that are within the evanescent reach of the gold substrate. However, compared to the incoherent SPP-Raman microscope, the imaging properties of the SPP-CARS microscope are markedly more complex. For instance, the gold substrate exhibits strong nonlinear properties itself, including an electronic four-wave mixing response, that may overwhelm the Raman resonant signal from the sample. In addition, the coherent radiation from the driven Raman oscillators in the sample plane produces interferences in the image plane that may complicate the image analysis. Before SPP-based

CARS microscopy can be applied to study biological samples, a better understanding of the imaging properties of the wide-field SE-CARS microscope is required.

In this work, we present a theoretical and experimental analysis of a wide-field, SPP-based CARS imaging system. To better understand the different contributions to the nonlinear signal, we study the signal in the image plane as well as in the back focal plane of the microscope objective. We identify signal contributions from both the sample and the gold substrate, and show that multiphoton fluorescence can be conveniently distinguished from the coherent nonlinear signal in the back focal plane. Using a simple dipole radiation model, we rationalize the origin of the observed artifacts in the SE-CARS images. Finally, we discuss the merits of the SPP-CARS microscopy technique and point to future applications of this method in biological imaging.

5.2 Materials and Methods

A schematic of the wide-field SE-CARS microscope is shown in Fig. 5.1. The system uses two input beams–a pump and a Stokes beam–to drive the CARS process. Both beams are derived from a light source that consists of a pump laser and a synchronously-pumped optical parametric oscillator (OPO). The pump laser is a Nd:vanadate oscillator (PicoTrain, High-Q) which produces 7 ps pulses at a center wavelength of 1064 nm. A portion of the laser output is used as the Stokes beam in the CARS process. Another portion of the output is frequency doubled and used to synchronously pump the OPO (Levante Emerald, APE-Berlin). The OPO delivers tunable radiation in the 780 to 920 nm range. For the CARS experiments discussed here, the OPO wavelength is set in the range from 800 to 825 nm producing the pump radiation for the CARS process. The Raman shift in this study is tuned to the

2700-3000 cm^{-1} spectral range corresponding to the energy of the the C-H vibrational stretching modes.

The pump and Stokes beams are separately conditioned with spatial filters and expanded to a $\sim$7 mm beam diameter. Both beams exhibit linearly-polarized Gaussian transverse profiles. The beams are independently focused onto the back focal plane (BFP) of a 60x 1.49 NA oil immersion objective (APON60XOTIRF, Olympus) to achieve wide-field illumination. The alignment allows for an angular difference between the beams as dictated by the different plasmon coupling angles of the pump ($\theta_{pump} = 65.1^o$) and Stokes ($\theta_{Stokes} = 63.1^o$) beams.

For each beam, a 25mm effective focal length (EFL) plano-concave and 75mm EFL plano-convex lens expands and then focuses the radiation onto the back focal plane of the objective. Each lens combination is mounted to a translation stage allowing independent adjustment of the lateral position of the focused spots on the BFP. The beams are quasi-collinearly overlapped in time and space with a 50/50 beam splitter thats is placed after the focusing lenses of the beams. Coupling efficiency to propagating SPP modes is determined experimentally by monitoring reflectivity changes from the gold film. Lower reflectivity from the gold layer corresponds to greater energy coupling into the SPP mode. The CARS radiation is detected in the epi-direction and separated from the incident light by a dichroic mirror (Semrock SWP 700 nm). Radiation from the sample plane is projected onto an imaging EM-CCD (Andor iXon) camera using two bandpass filters (Chroma ET660/40) to isolate the CARS signal. In case of BFP imaging, a Bertrand lens is inserted in the detection path to project the BFP onto the EM-CCD camera sensor.

Average power at the sample is $\sim$60 mW per beam for the entire field of view (FOV),

corresponding to less than 10 μW per μm^2. Images are taken with a 1 second integration time in the electron multiplication acquisition mode.

5.2.1 Sample Preparation

Sample substrates consist of borosilicate glass coverslips (BK-7, VWR) coated with gold. The coverslips are first pre-treated with a 2nm Cr adhesion layer. Then, Gold thin films are evaporated to a thickness of 30 nm on the coverslips. For patterned Au films, lithographic masks are used for depositing S1808 photoresist (Shipley) onto the surface, followed by chemical etching.

The lipid samples used in the experiments are droplets and crystals of cholesteryl oleate (Sigma Aldrich). The droplets are formed by preparing an emulsion of cholesteryl oleate with phosphatidylcholine in phosphate-buffered saline (PBS). Using $\sim$50 μL of a stock solution, the emulsion is subsequently spin-coated on the Au-covered microscope coverslips, resulting in air-dried droplets and micrometer-sized polymorphous crystals of cholesteryl oleate on the surface. We use a coumarin dye (coumarin 521T, TCI) as a generic two-photon excitable fluorophore. The dye is prepared as a 1 mM solution in water. Giant unilamellar vesciles (GUVs) are prepared from 1,2-dioleoyl-sn-glycero-3-phosphocholine (DOPC) and 10% 1,2-dioleoyl-3- trimethylammon propane (DOTAP), and are suspended in water.

5.2.2 Simulation Details

The simulated configuration consists of an upper halfspace filled with water, characterized by a permittivity ε_1, and a lower halfspace of glass with permittivity ε_3. We assume that the permeabilities of each of the halfspaces can be set to $\mu = 1$. The

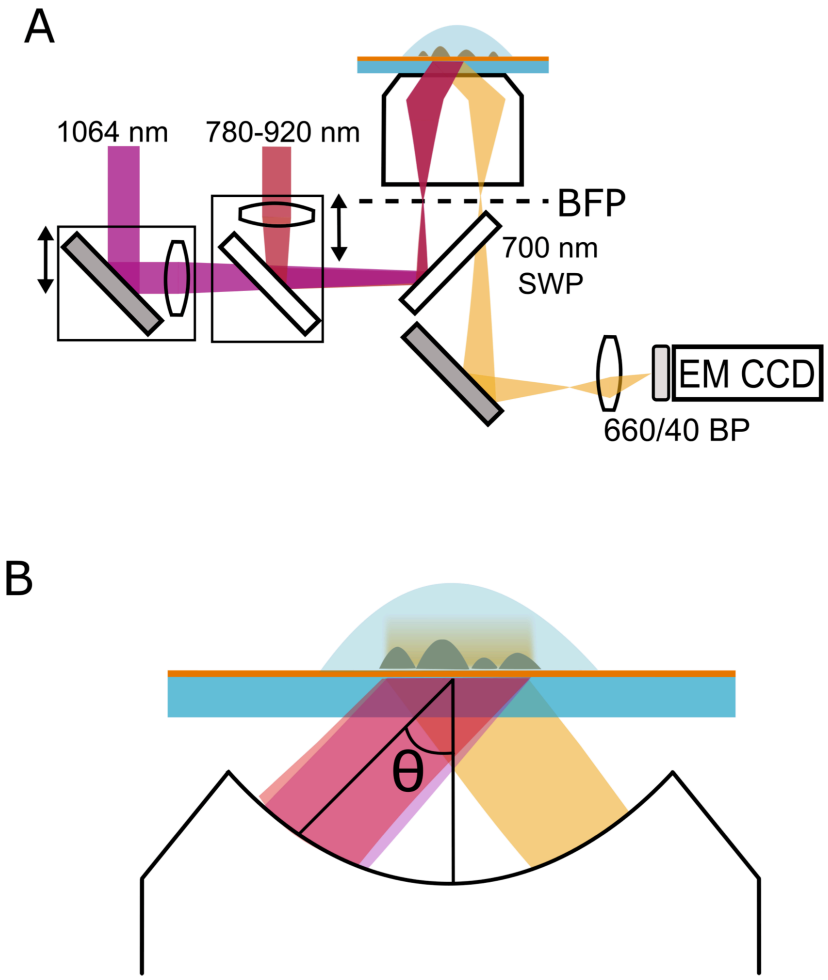

FIGURE 5.1: Sketch of the wide-field surface-enhanced CARS microscope. a) The Stokes (1064 nm) and pump (tunable) beams are independently focused onto the back focal plane (BFP) of the objective lens. Radiation from the sample plane is projected onto an imaging EM-CCD camera. b) The collimated Stokes and pump beam are incident onto the gold coated coverslip at their respective Kretchmann angles.

two hemispheres are separated by a thin gold layer (30 nm), with permittivity ε_2, as shown in Fig. 5.2. Excitation fields are simulated as monochromatic SPP surface waves at the pump (p) and Stokes (s) frequencies (Novotny and Hecht, 2012):

$$\mathbf{E}(\omega_u) = \begin{bmatrix} 1 \\ 0 \\ -k_{u,x}/k_{u,z} \end{bmatrix} e^{i(k_{u,x}x + k_{u,z}z)} \tag{5.1}$$

where $u = p, s$. The field is evanescent in the z-direction, and propagation of the SPP mode is along the x direction with a wavevector $k_{u,x}$. We will indicate the propagating mode with the wavevector k^{spp}, which is related to the free space excitation field (vacuum) wavevector k_0 as:

$$k^{spp} = k_0 n_3 \sin\theta_{spp} \tag{5.2}$$

where

$$\theta_{spp} = \sin^{-1}\left\{\frac{1}{n_3}\sqrt{\frac{\varepsilon_1\varepsilon_2}{\varepsilon_1+\varepsilon_2}}\right\} \tag{5.3}$$

The angle θ_{spp} is referred to as the plasmon coupling angle, which in this configuration is also known as the Kretschmann angle for the incident field. The surface fields $\mathbf{E}(\omega_p)$ and $\mathbf{E}(\omega_s)$ induce a third-order polarization in the material in the upper halfspace. In this work, we use a dipole model to describe the material response, which assumes that the material can be modeled as a collection of nonlinearly induced dipoles (Cheng et al., 2002a; Krishnamachari and Potma, 2007). The components of the nonlinear polarization $\mathbf{p}^{(3)}(\omega_{as})$ of a dipole oscillator placed at position $\mathbf{r}$ in the upper halfspace is given as:

$$p_i^{(3)}(\omega_{as}, \mathbf{r}) = \gamma_{ijkl}(\omega_{as}, \mathbf{r}) E_j(\omega_p, \mathbf{r}) E_k(\omega_p, \mathbf{r}) E_l^*(\omega_s, \mathbf{r}) \tag{5.4}$$

where $\omega_{as} = 2\omega_p - \omega_s$ is the anti-Stokes frequency and γ_{ijkl} is the third-order hyperpolarizability of the dipole at location $\mathbf{r}$. The hyperpolarizability is a tensor, but for simplicity we assume that it only has non-zero diagonal elements and that the response is isotropic. For clarity, we assume that the nonresonant response from the water medium can be ignored ($\chi^{(3)}_{water} \approx 0$), so that the radiative properties of the CARS-active dipoles that make up the target structure can be studied in detail. Using an 817 nm pump beam and a 1064 nm Stokes beam, the anti-Stokes radiation is found at 663 nm, where the permittivity of gold is $\varepsilon_2 = 13.883 + 1.038i$ (Johnson and Christy, 1972b).

The far-field radiation at ω_{as} is collected in the lower halfspace at the points R on a hemispherical surface. The transmission through the gold layer requires modeling of a planar, layered medium. For this purpose, we use an asymptotic far-field Green's function for layered media, where the gold layer is described by generalized Fresnel coefficients. The far-field contribution of a dipole radiator at point $\mathbf{r}$ to the field detected at point $\mathbf{R}$ is (Novotny and Hecht, 2012):

$$\mathbf{E}_d(\mathbf{R}) = \frac{\omega^2}{\epsilon_0 c^2} \overline{\mathbf{G}}(\mathbf{R}, \mathbf{r}) \mathbf{P}^{(3)} \tag{5.5}$$

here $\overline{\mathbf{G}}$ is the far-field Green's function. Details on the Green's function are found in the Appendix. The total CARS field in point $\mathbf{R}$ is the sum of the contributions from each of the dipole emitters in the upper halfspace:

$$\mathbf{E}(\mathbf{R}) = \frac{\omega^2}{\epsilon_0 c^2} \int dV \overline{\mathbf{G}}(\mathbf{R}, \mathbf{r}) \mathbf{P}^{(3)} \tag{5.6}$$

where the integration is over the volume V of the upper halfspace. For the CARS process, which is coherent, the intensity at point $\mathbf{R}$ is directly proportional to the

square modulus of the summed field, i.e. $I(\mathbf{R}) \propto |\mathbf{E}(\mathbf{R})|^2$. If the radiation is incoherent, as is the case for the multi-photon excited fluorescence background, the intensity is written as $I(\mathbf{R}) \propto \int dV\, |\mathbf{E}_d(\mathbf{R})|^2$, where the dipole radiation now results from a nonlinearly excited fluorescence process. For better visualization, the field distribution on the hemisphere is projected to a planar two dimensional surface, which represents the image in the back focal plane (BFP). A Fourier transform of the BFP image provides a representation of the sample plane image in the far-field.

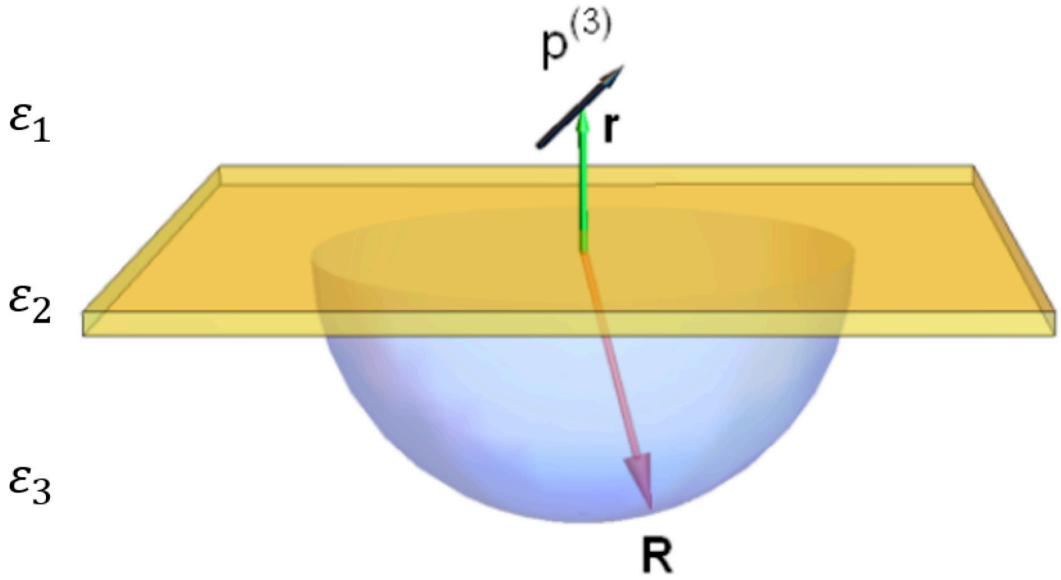

FIGURE 5.2: Schematic of the simulated configuration. A dipole positioned at **r** is located in the space above the gold layer. Radiation of the dipole is collected through the gold layer in the glass medium on the surface of the lower far-field hemisphere (radius = 1m).

5.3 Results

5.3.1 Incoherent contributions: two-photon excited fluorescence

We first study the contributions from fluorescent species that are tentatively excited in a typical wide-field SE-CARS experiment through a two-photon excitation

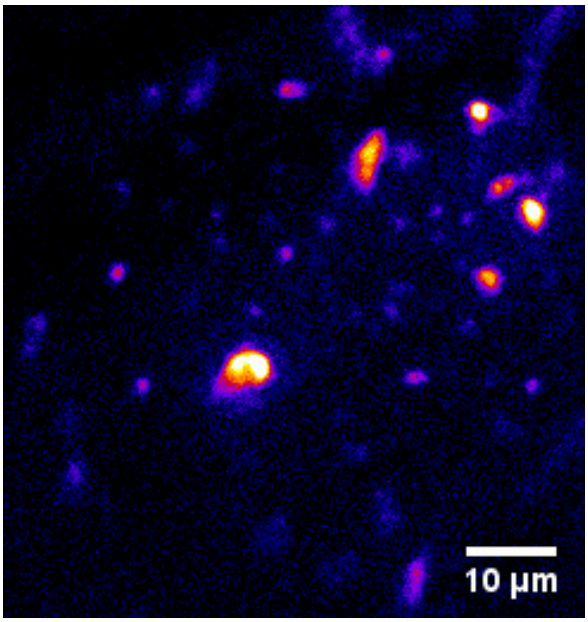

FIGURE 5.3: Wide-field TPEF image obtained from clusters of coumarin dye on the gold layer in water. Fluorescence is induced by the 817 nm pump beam.

process and thus give rise to a incoherent background signal. While we observe induced two-photon excited fluorescence (TPEF) from both the pump and Stokes beams, the strongest contribution is observed from the pump beam. For this reason, we focus here on TPEF generated by the pump beam set to 817 nm, while blocking the Stokes beam. Under these conditions, no SE-CARS signal is observed, and the signal that is detected through the CARS bandpass filter originates from the pump-induced TPEF process.

There are two main contributions to the TPEF background: 1) emission from fluorescent compounds that are present in the sample, and 2) TPEF from the gold layer. If the sample contains fluorophores with high quantum yield at high concentration, then the observed image on the CCD camera is dominated by sample fluorescence. An example is shown in Fig. 5.3, where clusters of coumarin dye close to the surface are visualized. This imaging mode shares similarity with total internal reflection

fluorescence (TIRF) microscopy (Axelrod, Burghardt, and Thompson, 1984; Trache and Meininger, 2005), with the important difference that here the evanescent field is provided by the SPP mode. Surface-enhanced TPEF with SPP modes has been suggested as a tool to enhance the efficiency of TIRF (He et al., 2009), however, suitable spacers are required to suppress quenching of the fluorophores that are proximal to the metal film (Lin et al., 2010).

In Fig. 5.4(a), we examine the TPEF in the back focal plane of the objective lens. The incoherent fluorescence appears as a thin, symmetric ring corresponding to the Kretschmann coupling angle of the emitted radiation. This pattern is expected for surface plasmon mediated emission of dipoles in the upper half sphere (Gryczynski et al., 2004). In Fig. 5.4(b), a simulation of the incoherent dipole emission is shown, confirming the pattern that is observed experimentally.

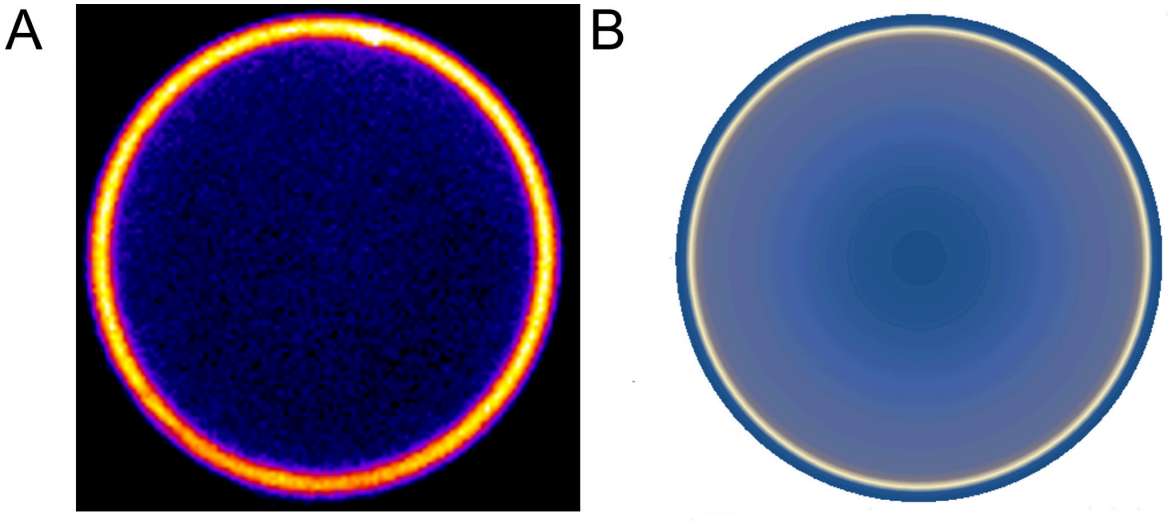

FIGURE 5.4: TPEF observed in the BFP. a) Experiment using coumarin in water. b) Simulation based on a random distribution of incoherent dipole emitters placed in the sample plane, 1 nm above the gold film. The BFP pattern in this case is independent of dipole placement and resembles that of a single coherent dipole emitter.

If the sample is devoid of fluorophores, a weak emission can sometimes still be observed. For instance, when non-fluorescent lipid droplets or polystyrene beads are

placed on the gold surface, TPEF can be seen from the location of the object. This fluorescence results from the two-photon induced inter-band transition in gold, followed by radiative emission upon electron-hole recombination (Boyd, Lu, and Shen, 1986). This contribution is virtually undetectable in case of the bare gold film, but is enhanced when objects are placed on the surface, suggesting that local field effects may enhance the coupling of radiation to the far-field. Hence, enhanced local fields at the nanoscopic junctions between dielectric particles and the gold film provide imaging contrast through locally enhanced gold TPEF at the particle's location. Much higher contrast is observed for dry-mounted objects compared to the case when sample is immersed in water. The gold-related TPEF also appears as a ring-like structure in the BFP, identical to sample fluorescence. In some cases, the TPEF from gold rivals the SE-CARS signal, forming an unwanted background. A straightforward way to suppress the fluorescence is to collect images with (I_{Total}) and without (I_{TPEF}) the Stokes beam, and retrieving the CARS image by computing the normalized difference:

$$I_{CARS} = \frac{I_{Total} - I_{TPEF}}{I_{TPEF}} \tag{5.7}$$

Alternatively, the unique distribution of the TPEF in the BFP also offers an opportunity to discriminate the incoherent fluorescence from the CARS signal, as the emission characteristics are different. In the next sections, we discuss the characteristics of coherent radiation in the image plane and in the BFP.

5.3.2 Coherent contributions: surface-enhanced CARS

We next examine the SE-CARS signal by coupling both the pump and Stokes beams to SPP modes. Without a Raman active sample, the signal from the bare gold film is negligible. This indicates that intrinsic four-wave mixing (FWM) in the gold or at the gold interfaces is not contributing to a noticeable background in the absence of a sample. Strong coherent radiation can be clearly observed, however, if lipid droplets are placed on the surface. The detected signal scales quadratically with the pump beam and linearly with the Stokes beam, as shown in Fig. 5.5(a). The signal peaks whenever the pump and Stokes beams overlap in time, as is evident in Fig. 5.5(b). At longer time delays, no coherent signal is observed, and the detected signal at these settings is governed by TPEF induced by the individual excitation beams.

These observations confirm that the coherent signal originates from a four-wave mixing process, producing a signal at ω_{as}. This signal can have both vibrational and electronic contributions. In Fig. 5.6 we investigate the dependence of the signal on the Raman shift in the 2800–2950 cm^{-1} vibrational energy range. The sample consists of a giant unilamellar vesicle (GUV) of DOPC, shown in the SE-CARS image in panel 5.6(c). The spectrum of the vesicle is derived from the single bilayer that contacts the surface. This spectrum is represented by the red squares in Fig. 5.6, yielding a CARS lineshape that is typical for phospholipids (Cheng et al., 2002b; Potma and Xie, 2003). For comparison, we collected a CARS spectrum in laser scanning mode (i.e. regular CARS microscopy) from a multilamellar particle of the same DOPC material, indicated by the black circles in Fig. 5.6(a). Note that unlike the GUV in the SE-CARS image, this particle is composed of multiple membranes folded into an amorphous structure. The spectra appear very similar,

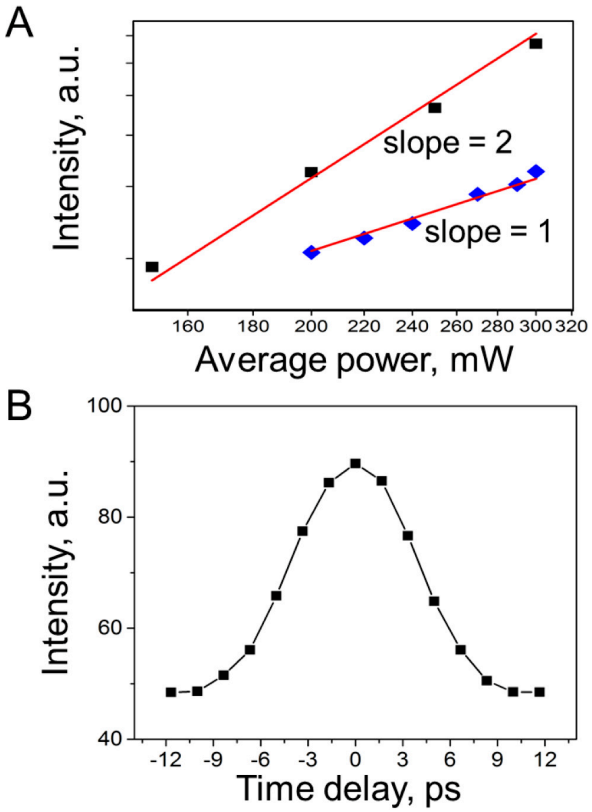

FIGURE 5.5: Characteristics of observed signal. a) Power dependence of pump (black squares) and Stokes (blue diamonds) beams. b) Dependence of the observed signal as a function of pulse overlap in time.

thus confirming the presence of a vibrational CARS contribution in SE-CARS. However, the spectra are not exactly identical. This suggests that mixing contributions from electronic FWM are somewhat different between the two imaging modes. Indeed, similar to enhanced TPEF from gold in areas where the samples contact the metal surface, there is enhanced FWM from the gold near the contact regions (Fast et al., 2016). Therefore, the nonresonant contributions in wide-field SE-CARS are generally higher than what is commonly seen in laser scanning CARS microscopy. Moreover, the magnitude of the gold FWM contribution is dependent on sample material, the morphology of the object, and the structural details in the contact region. These factors introduce small variations in the amount of electronic FWM

signal that is mixed in with the vibrational CARS signal. Nonetheless, as is evident from Fig. 5.6, the vibrational contrast is clearly seen, thus allowing vibrational imaging in SE-CARS mode with confidence. We note that, for the power levels used in the experiments described here, the observed CARS signal is only visible when the gold layer is present. When a bare glass surface is used, no CARS signal is detected (Fast et al., 2016).

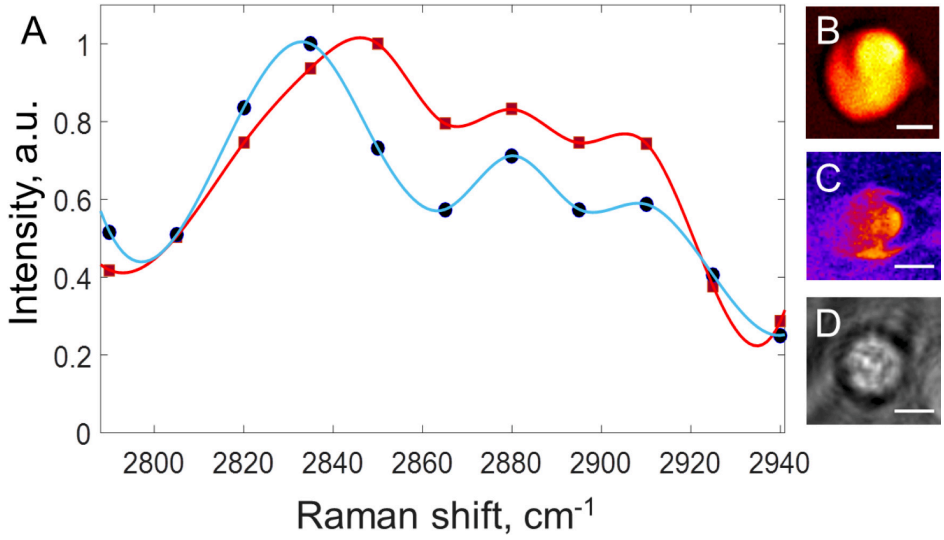

FIGURE 5.6: Spectral dependence of the surface-enhanced CARS signal. a) Comparison of the CARS spectrum of lipid collected in the wide-field, surface-enhanced configuration (red squares) and in the laser-scanning configuration (blue circles). b) Multilamellar vesicle of DOPC on glass visualized at 2845 cm^{-1} in the laser-scanning imaging mode. c) Giant unilamellar vesicle (GUV) on the gold surface recorded at 2845 cm^{-1} in wide-field SE-CARS mode. d) Transmission image of the GUV shown in panel c). Scale bar is 5 μm.

5.3.3 Characteristics of coherent radiation

In the previous sections, we established that the detected signal in SPP-based CARS imaging contains a clear vibrational CARS signal in addition to weak contributions from enhanced FWM and TPEF from gold/sample contact regions. In this Section,

we study the radiation characteristics of the coherent CARS contributions and how the radiating field produces certain image features in the far-field. We have already seen in Section 35.3.1 that the incoherent TPEF is distributed in a ring-like distribution in the BFP due to the radiative coupling through gold film. Here we discuss the coherent radiation of dipoles placed near the gold surface using the Green's function formalism outlined in Section 25.2.2, followed by a comparison with experiment.

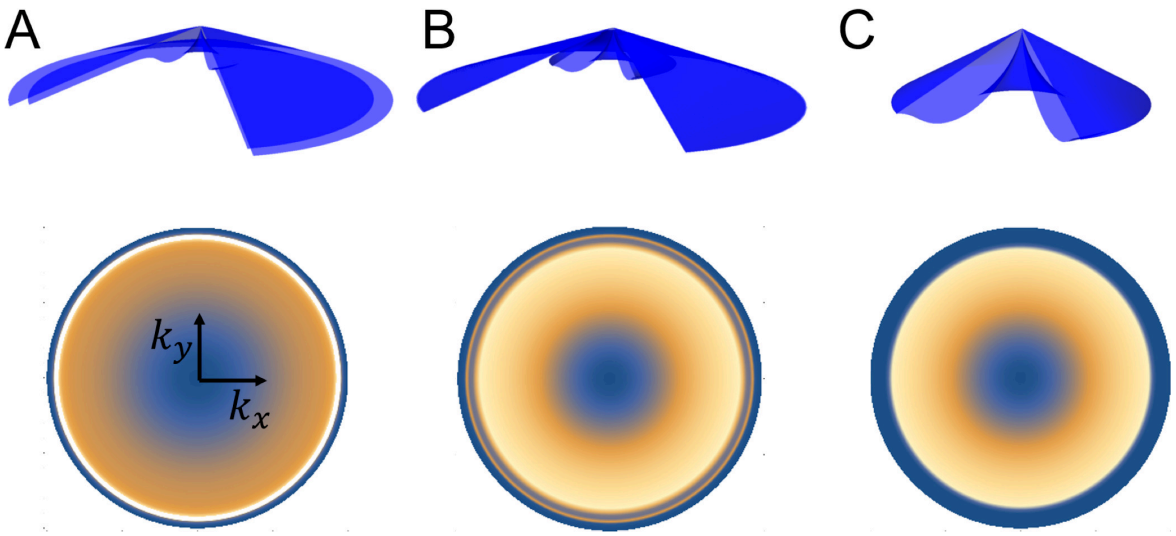

FIGURE 5.7: Simulated CARS radiation of driven dipole emitter into the lower halfspace as a function of height above the interface. Intensities are rescaled in each case to highlight features in the emission pattern. a) Dipole placed 1 nm above gold surface b) Dipole placed 250 nm above gold surface. c) Dipole placed 1000 nm above gold surface.

The evanescent SPP excitation fields given in Eq. 5.1 contain both x and z polarization components. Since there is a $\pi/2$ phase shift between E^x and E^z, the dipole is effectively driven by an elliptical excitation field. In our example of an isotropic induced-dipole, radiative components of both x and z can be expected. Since $E^z > E^x$, the z-polarized component is expected to be the dominant contribution at the far-field detector, and the sample effectively behaves as a collection of vertically oriented dipole emitters.

Figure 5.7 shows the angularly resolved CARS radiation from a dipole near the gold film, as observed in the lower halfspace. In Fig. 5.7(a), the dipole is positioned close to the gold surface at a distance of 1 nm. At this proximal distance, coupling through the film is very efficient, resulting in a ring-like distribution of the radiation in the BFP. This situation is very similar to linearly excited dipoles close to the surface (Lieb, Zavislan, and Novotny, 2004; Gryczynski et al., 2004; Shegai et al., 2011), where the radiation is highly confined to angular components close to the plasmon coupling angle, resulting in an azimuthally symmetric radiation pattern. The angle of maximum emission intensity, $\theta_{sp} = 69.6^o$, lies above the critical angle, $\theta_c = 61^o$, which partitions the signal into contributions from plane waves below, θ_c, and coupled evanescent light above θ_c (Novotny, 1997; Hecht et al., 1996; Smolyaninov et al., 1997). The former being associated with direct dipole emission through the film and the latter coming from optical tunneling and leakage radiation of the evanescent fields originating from excited SPP fields at ω_{as}. For the geometry relevant here, the propagation length of the SPP mode excited at the anti-Stokes frequency is $L_{spp} = 13\ \mu m$ Drezet and Genet, 2013,foley:15. These propagating surface wave contributions to the signal give rise to distinct imaging artifacts, as will be discussed below.

In Fig. 5.7(b), the dipole is placed farther away from the gold surface, at a distance of 250 nm. The radiation pattern shows some markedly different features in the back focal plane. Portions of evanescent contributions can still be seen beyond θ_c, but the narrow ring of k-vector components that originated from SPP-coupled radiation is now absent, resulting in a dark ring at θ_{sp}. In Fig. 5.7(c), the dipole is placed 1 μm away from the surface. At these distances, no evanescent contributions are passed through the film and the remaining radiation originates from direct

(far-field) dipole-emission through the film. This example underlines that depending on the distance of the dipole from the surface, different radiative contributions can be expected. In particular, for dipoles within a few nm from the surface, the SPP-coupled radiation is strong, a contribution that disappears for dipoles that are situated farther from the surface.

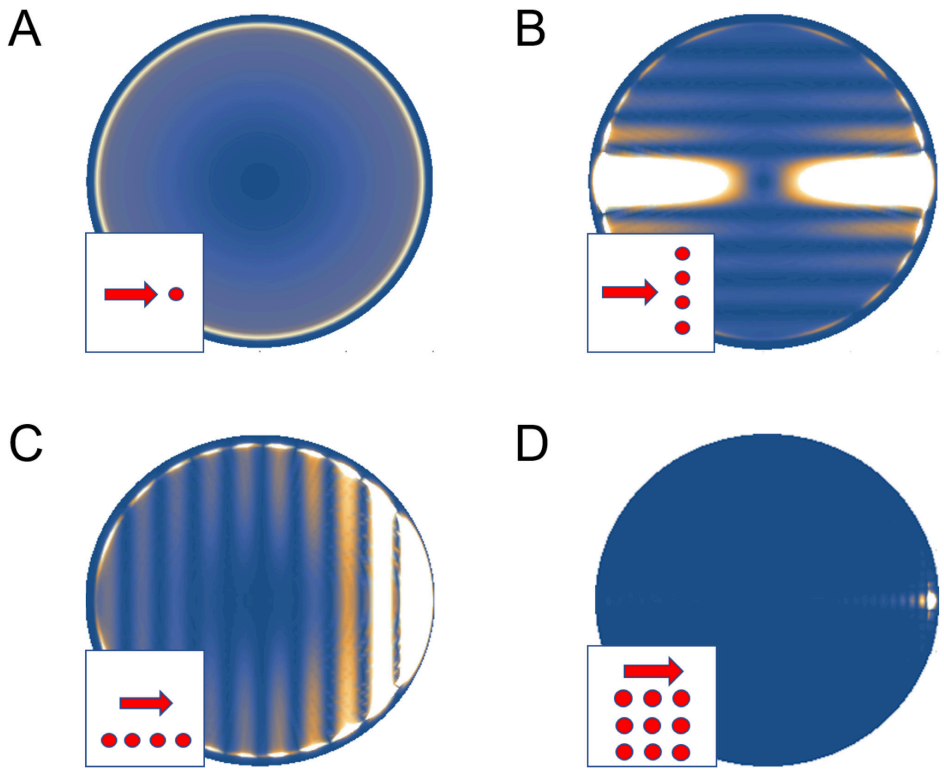

FIGURE 5.8: CARS radiation patterns from dipole emitters in the BFP. a) Single dipole 1 nm above the gold interface b) Dipole chain of 16 dipoles spaced 150 nm apart at a height of 1 nm above the gold layer, aligned perpendicular to the propagation direction. c) Dipole chain of 16 dipoles spaced 150 nm apart at a height of 1 nm above the gold layer, aligned in the direction of propagation. d) A 50x50 square array of dipoles 1 nm above the gold layer. Arrow indicates the direction of propagation of the surface excitation fields.

The dipole radiation pattern is shown again in Fig. 5.8(a), as seen in the BFP. Figure 5.8(b) shows the radiation pattern resulting from a collection of dipoles that are aligned in the y-direction, perpendicular to the direction of propagation of the surface excitation fields. Whereas the ring-like structure can still be recognized, there

are clear interferences observed between the ω_{as} radiation of the individual dipoles. The pattern reflects the destructive and constructive interference of the dipole radiators in the y-direction, while their contributions remain in-phase along the x-axis, producing bright portions of radiation in this direction The pattern changes dramatically when the point dipoles are arranged along x, as depicted in Fig. 5.8(c). No interferences are observed in the y-direction, while the mutual spacing between the emitters along x gives rise to maxima and minima. In addition, the signal is significantly stronger on one side of the radiation cone. The stronger signal reflects the fact that the dipoles radiate in phase in this direction, due to phase matching between the excitation fields and the anti-Stokes emitted field. The coherence length, given as $L = \pi/(2k_p^{spp} - k_s^{spp} - k_{as}^{spp})$, is longer than 10 μm. Since L is of the order of the SPP propagation length, the SPP wave has the opportunity to grow during its propagation due to constructive interference along the x direction.

In Fig. 5.8(d) we show the CARS radiation pattern from a collection of dipoles that are organized in a square array. The size of the square exceeds the wavelength λ_{as}^{spp} of the anti-Stokes radiation by several times, and we may thus expect a highly directional signal that is in phase predominantly along the direction of k_x^{spp} (Shegai et al., 2011). Indeed, because of phase-matching, the azimuthal distribution in the BFP is broken and the signal now peaks exclusively in one direction. The amount of light coming from the phase-matched direction is over an order of magnitude higher than from a similar area on the ring. Note that such a radiation pattern is radically different from the BFP signal distribution for incoherent emission. In the latter case, the signal always exhibits azimuthal symmetry, independent of the positioning of the emitting dipoles in the sample plane.

The discussion above suggests that CARS and TPEF radiation appear differently in the BFP. Figure 5.9 shows an experimental realization of this notion. In panel (a),

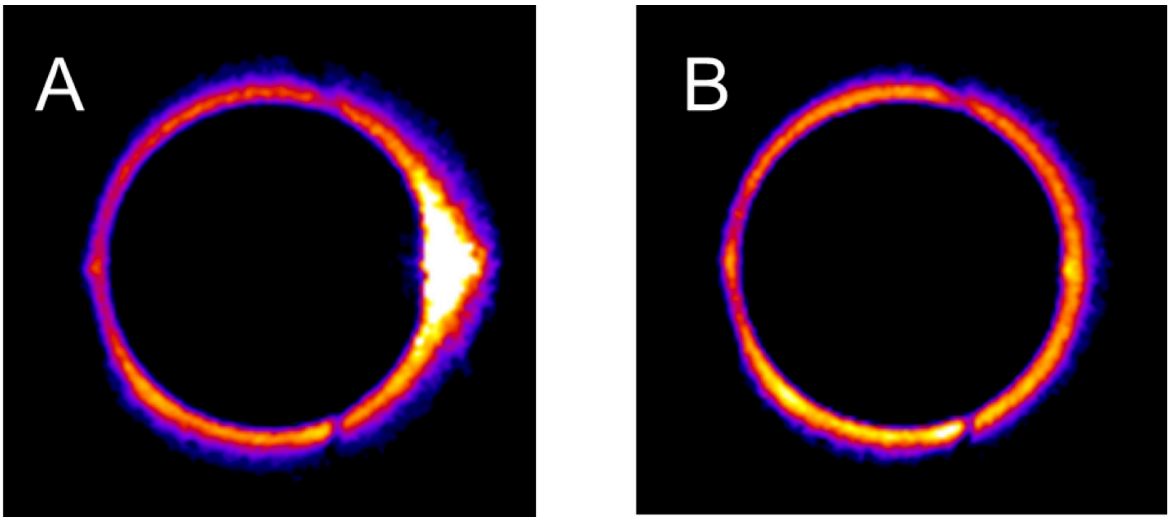

FIGURE 5.9: SE-CARS imaging in the BFP. a) BFP image of clusters of cholesteryl oleate on the gold surface at 2845 cm^{-1}. b) BFP image of the same sample when the pump and Stokes pulses are temporally detuned.

several clusters of cholesterol oleate deposited on the gold surface form a CARS signal at 2845 cm^{-1} which is visualized in the BFP. The image shows the familiar azimuthal pattern of the signal in addition to a clear bright spot near the k_x^{spp} location. Note that the intensity of the phase-matched radiation spot is saturated in the Figure to make the annular incoherent contribution visible. The image in panel (b) is observed when the pump and Stokes beam are temporally detuned. This generates an image similar to (a) but without the bright spot. We may thus conclude that the signal along the ring shown in (b) is due to TPEF of the gold film, whereas the additional bright spot is due exclusively to phase-matched CARS signal. This comparison also underlines the feasibility of using masks in the BFP to suppress the TPEF contributions while passing the CARS portion of the signal.

We next study the SE-CARS signal from two structures in the image plane. Figure 5.10(a) depicts the simulated SE-CARS image of an array of point dipoles arranged along the x direction. The linear alignment of the dipoles is clearly distinguished in

the image. However, the excitation of SPP waves by each of the dipoles gives rise to SPP leakage radiation at ω_{as} over a length scale corresponding to L_{spp}. As discussed above, efficient excitation of SPP waves is expected when the point dipoles are within several nm of the gold surface. Because the individual SPP contributions are in-phase in the positive x-direction, the image contains a directional, flare-like feature that appears to emanate from the dipole chain. In the negative x-direction, the SPP waves are not in phase, resulting in a depleted signal at the other end of the chain structure. A similar observation is made in Fig. 5.10(b), which depicts the SE-CARS image of dipoles organized in a 3 μm diameter ring. The ring structure is reproduced in the CARS image, along with the directional SPP leakage radiation. The positions of the radiating dipoles is such that additional interferences can be seen in the flare that stretches along the positive x-direction. We note that the flaring effect is suppressed for point dipoles that are spaced farther away from the surface. These examples show that SE-CARS images contain coherent features that are absent in incoherent TPEF images.

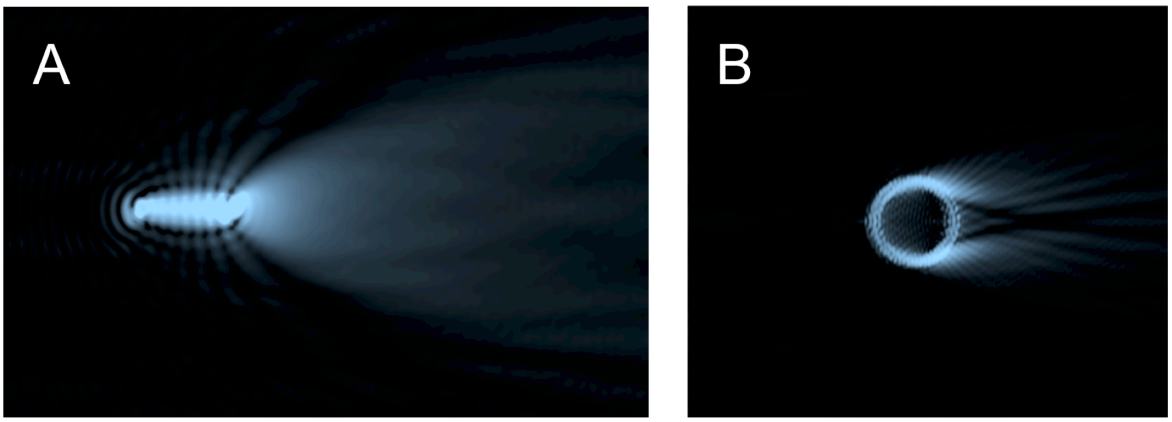

FIGURE 5.10: a) Simulated chain of 32 dipoles spaced 150 nm apart. b) Simulated image of a 3 μm diameter ring made up of dipoles spaced 150 nm apart. In both cases, the dipoles are placed 1 nm away from the gold surface. The field values are recorded on a 1 meter radius glass hemisphere in the lower half-space and Fourier transformed to produce a real-space image.

5.3.4 SE-CARS imaging examples

Figure 5.11(a) shows a SE-CARS image of cholesteryl oleate droplets deposited on the gold surface. Because the thickness of the droplets exceeds the penetration depth of the CARS excitation field ($\sim$ 100 nm), the signal originates only from cholesteryl oleate that falls within the evanescent excitation volume Fast et al., 2016. The image is not affected by interferences from SPP-related flares, because the ω_{as} radiation of only a relatively small portion of the driven molecules is efficiently coupled to the SPP mode. When the Stokes beam is blocked, the SE-CARS signal disappears and the remaining TPEF signal becomes clearly visible, as shown in Fig. 5.11(b). Recall that the TPEF emission results from the gold and is thus not necessarily sensitive to the chemical composition of the objects themselves.

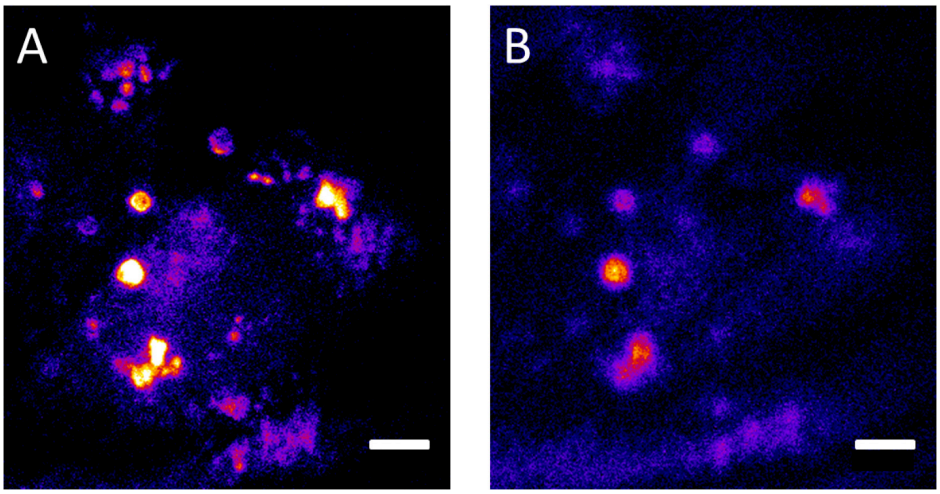

FIGURE 5.11: Cholesteryl oleate lipid droplets in water. a) SE-CARS image at 2845 cm^{-1}. b) TPEF image obtained by blocking the Stokes beam. Scale bars are 20 μm.

The SE-CARS images from thinner structures look noticeably different. An example of a thin-structure is found in the GUV image in Fig. 5.6(c). Because the phospholipid molecules are close to the gold surface, coupling to a SPP mode at ω_{as} is efficient, producing clear streaks in the image. The dark spot found on one end

of the structure is reproduced in the simulation of Fig. 5.10(b). This example confirms that the morphology of the structure plays an important role in the amount of flaring observed in the SE-CARS image.

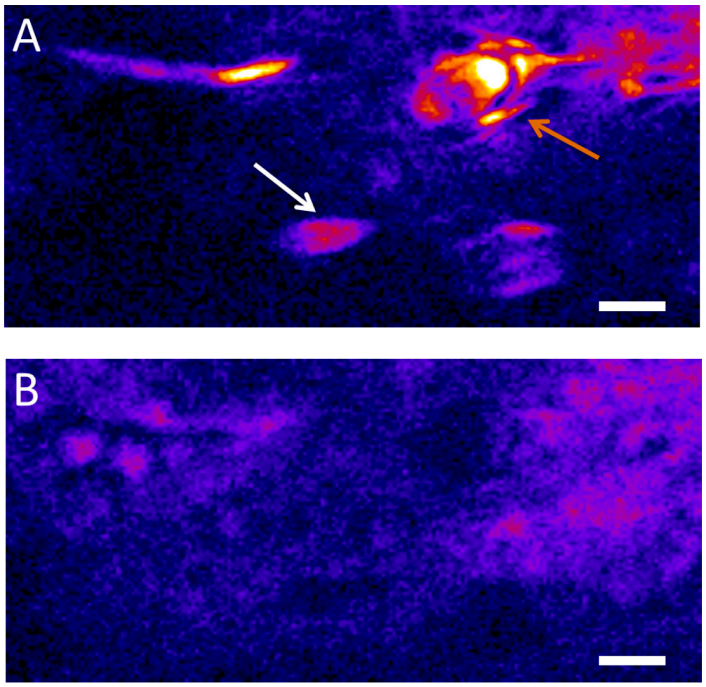

FIGURE 5.12: Polystyrene structures in water. a) SE-CARS image at 2845 cm^{-1}. b) SE-CARS image at 2960 cm^{-1}. Scale bars are 5 μm.

In Fig. 5.12(a), we visualized several polystyrene structures of various shapes and thicknesses, obtained by melting 3 μm polystyrene spheres on the gold. The image is recorded at 2845 cm^{-1}, near the CH_2 symmetric stretching mode of polystyrene. The difference between spherical scatterers and more planar shapes is apparent. Spherical beads, indicated by the white arrow, tend to leave small streaking jets that move away from the sample in the direction of SPP propagation. This appears to be consistent with the small penetration depth of the SPP field in z which excites a only small portion of the sphere's bottom. The orange arrow points to a thin and flat layer of polystyrene that provides another good example of flaring. The coherent nature of the radiation is evident from the interferences that can be distinguished

in the flares. Note that a weak signal can be seen in areas where no structures are present. This signal results from the non-resonant SE-CARS signal from the medium (water). This is made clearer in Fig. 5.12(b), where the same structures are imaged at 2960 cm^{-1}, a vibrational energy at which the resonant SE-CARS signal interferes destructively with the non-resonant signal from water. The polystyrene structures now appear dark against a background of predominantly non-resonant SE-CARS signal.

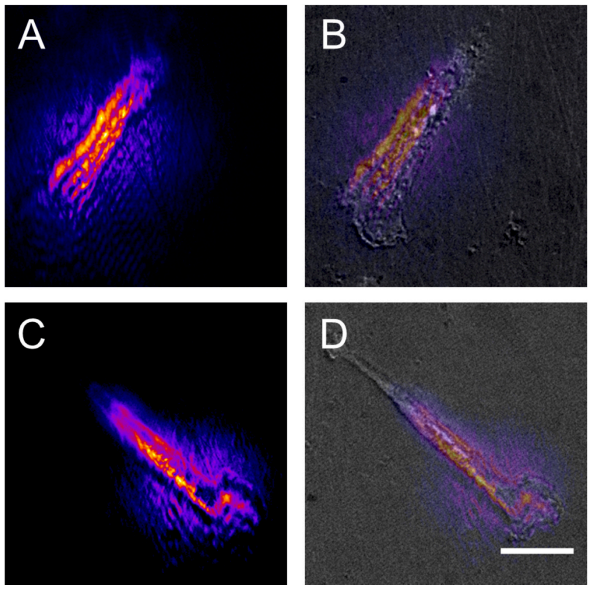

FIGURE 5.13: MCF7 Breast cancer cells. a,c) CARS image at 2845 cm^{-1}. b,d) overlay of cars and transmission images. Scale bar is 20 μm

Finally, in Fig. **??**, we provide images of cells adhered to the gold surface. To improve the image contrast, we have dried the cells in air, resulting in a higher concentration of cellular material close to the surface. Under these conditions, strong SE-CARS signals are obtained, which co-localize with the transmission image of the cells. These signals are reduced when the Raman shift is tuned off resonance. Although this example is not representative of typical cellular imaging conditions, it does illustrate that (vibrationally resonant) SE-CARS signals can be generated from

cellular materials. At the same time, improvements are needed to bring cells in aqueous media into sharper view.

5.4 Discussion

In this work, we discussed the imaging properties of wide-field SE-CARS in detail. Although the SPP-based CARS microscope shares its spectroscopic sensitivity with conventional CARS microscopy, its imaging properties are radically different. Whereas in regular CARS imaging, the phase-matched coherent radiation from molecules in the focal volume is integrated on a single pixel, far-field detector (Cheng et al., 2002a); in wide-field SE-CARS the radiation is collected on a detector array in directions that are mutual to the propagation direction of the SPP excitation fields. Therefore, image features seen in SE-CARS imaging cannot be directly compared with features known from conventional CARS microscopy. Rather, in terms of excitation and detection geometry, the SPP-based CARS microscope has more in common with surface plasmon resonance imaging (SPRi) (Boozer et al., 2006; Huang, Yu, and Zare, 2007; Halpern et al., 2014) and surface plasmon coupled emission microscopy (SPCEM) (**borejdo06**; Lakowicz et al., 2003; Stefani et al., 2005). Similar to SPRi and SPCEM, the radiation from the sample is strongly influenced by the metal film.

The signals detected in the wide-field SE-CARS microscope originate from different mechanisms. First, there are incoherent emission contributions. These contributions come from excited fluorophores that might be in the sample, in addition to the two-photon-excited luminescence from the gold layer itself. These fluorescence contributions always manifest themselves as a ring-like radiation pattern in

the back focal plane, irrespective of the distribution of the fluorosphores in the sample plane.

Second, there are coherent radiation contributions in the SE-CARS microscope. The coherent radiation originates from driven dipoles in the upper halfspace, derived from a vibrational or electronic CARS process, thus producing radiation at ω_{as}. Importantly, the radiation pattern depends on the distance of the dipole oscillator from the surface. For the closest dipoles, SPP waves at ω_{as} are excited and coupling is at the plasmon coupling angle, resulting in a ring-like pattern in the back focal plane. Constructive interference between the radiation from different dipoles produces stronger signals and preferred propagating of the excited SPP waves in the phase-matched direction, leading to flares and streaks in the SE-CARS image. The SPP contribution is suppressed for dipole radiators farther away from the surface, thus producing CARS images that are devoid of streaks. Generally, we observe streaks for very thin samples such as phospholipid bilayers, whereas flare-free images are observed for thicker samples such as droplets of neutral lipids. Hence, our dipole-based model explains the differences in the appearance of the images depending on the object being imaged.

Like the conventional CARS microscope, the SE-CARS instrument is capable of generating images with vibrational contrast. However, the SE-CARS images are affected by a stronger two-photon excited fluorescence background, in addition to the appearance of streaks and flares due to SPP propagation. These features affect the interpretation of the SE-CARS images, which are generally more difficult to interpret than the images generated in a point-scanning CARS microscope. A better understanding of the origins of SE-CARS image features, such as presented here, can help guide the image interpretation and thus improve the utility of the SE-CARS microscope.

Despite the more complex image properties of the wide-field SE-CARS microscope, the efficiency of CARS signal generation is many orders of magnitude higher than in a point scanning microscope. For instance, assuming an image acquisition time of 1 second, the integrated signal level for a GUV bilayer is about the same as seen in the SE-CARS and the conventional CARS microscope. At the same time, the incident pulse energy per μm^2 in the SE-CARS microscope is more than four orders of magnitude lower Fast et al., 2016. Part of this higher efficiency is due to the fact that the pixel dwell time is much higher in the wide-field detection, amounting to 1 second per pixel for SE-CARS versus $\sim$ 1 μs per pixel for the point-scanning microscope. Even so, bringing down the pulse energy in a regular CARS microscope to $\sim$70 fJ/μm^2, as it is the SE-CARS measurement, and integrating for 1 second would still yield signals that are lower by more than 10^7. This enormous increase in SE-CARS signal generation efficiency is due to the surface-enhancement effect facilitated by the flat gold film. The effective field enhancement provided by the surface is much smaller than what is common for the 'hotspots' in SERS, typically less than a factor of 10. Yet, the nonlinearity of the CARS process combined with the enhancement of the radiative rate at ω_{as} afforded by the film still produces an effective signal enhancement of more than seven orders of magnitude. Unlike in SERS, this enhancement is not localized to specific spots, but is *uniform* across the entire field of view instead. In effect, the surface enhancement in wide-field SE-CARS allows the amplification of an *entire image* with a factor of $\sim 10^7$. The latter is the true merit of this type of microscope.

5.5 Conclusion

In this work we have experimentally and theoretically analyzed the imaging properties of the wide-field SE-CARS microscope. Using a dipole model to describe the sample, we have found that for thin samples such as lipid bilayers, SPP waves are efficiently excited at the anti-Stokes frequency, producing strong CARS signals with incident pulse energies as low as 70 fJ/μm^2. However, the coherent SPP waves at the signal frequency give rise to flares and interfering streaks in the image. For thicker samples, such as lipid droplets, the SPP contribution is relatively small, producing SE-CARS images free of propagation artifacts. The use of a thin gold film gives rise to a signal enhancement of more than seven orders of magnitude relative to CARS generation with freely propagating light. With a better understanding of the imaging properties of the wide-field SE-CARS microscope, this imaging method may prove useful for imaging and sensing applications in which low light levels per unit area are required.

Chapter 6

Conclusion

Coupling pulsed near-IR lasers to SPP modes on thin gold films results in pulsed evanescent fields permeating the metallic surface and the adjacent dielectric. Dissipation of this energy is partially due to Ohmic heating in the film, but the remainder may be partially redirected and coupled to radiative channels that are detectable in the far field with a CCD camera. The experiments conducted here demonstrate that SPP fields excited over a wide-field of view have sufficiently large peak fields to drive nonlinear light-matter interactions at the interface where field intensity is greatest.

In Cofefe, a two photon fluorescence from the gold film can be generated by spatial confinement of SPP fields. At visible wavelengths, gold films themselves have a well documented incoherent luminescence attributed to interband transitions that subsequently radiate through electron-hole recombination. In the near-IR range, the optical response of smooth gold can be modeled reasonably well by a free electron gas with a correspondingly weak visible luminescence. The strength, however, changes dramatically in the presence of nanostructures which produce confined enhancement of the surface fields. In these confined spaces, photon momenta become

large enough to enhance rates of interband transitions in the gold film. Observations of luminescence emanating from locations of non-fluorescent particles signifies that the gold itself is the source of the signal and that the incoherent signal produced can serve as a method of localizing positions of analytes at the surface. One promising application of this sensing mechanism revolves around the intense emission seen from gold nanospheres. While the emission displays intensity variations in time, signals from 30 nm gold spheres can be easily detected in DNA binding experiments where particles coated with single DNA strands are adhered to the surface by binding with a complementary strand functionalized on the film surface. Presently, the observed binding rates can vary greatly between trials due to convection currents induced by heating over the illumination area. Incorporation of a fluidic channel is one potential method of creating a more controlled environment by establishing a laminar flow over the sensor surface. Forming a connection between reproducible binding rates and the properties of the solution and fluid flow would establish an attractive bio-sensing tool. One appeal of Cofefe is that it is based on incoherent emission generated at the location of particles at the surface, free from interference effects observed in similar techniques. SPRI, in contrast, is a technique based on the interference between leakage radiation and the reflected laser field that leads to the diffraction patterns observed at locations of refractive inhomogeneities. Signals generated at the surface have the added benefit of being able to couple to SPP modes themselves, providing a radiative channel for the near field components of the signal in the form of leakage radiation.

The well defined wave vectors of SPP modes leads to intuitive multi-beam geometries capable of exploiting the coherent nature of CARS to produce a detectable signal in a phase matched direction along the film surface. In the SECARS microscope, chemically sensitive wide field images have been produced for organic

samples rich in C-H bonds. Imaging artifacts are observed for extended structures and can be simulated by the coherent addition of far-field emission from a collection of point dipoles. The detailed emission properties can be described by Green's functions which incorporate the optical properties of the gold film through generalized Fresnel coefficients. Aberrations limit the imaging capabilities of the SECARS microscope and yet are a clear sign that the gold film serves as an effective 4WM platform.

Intuitively, coherent imaging artifacts should decrease as the dimensions of the sample decrease. CARS signals from lipids and cells benefit from surface enhancement and multiplicity but are relatively weak or undetectable from samples that are smaller than the excitation wavelength. One potential method of boosting the CARS signal is to employ recently developed Raman dyes that operate in an electronic pre-resonance regime to enhance the vibrational signal without drastically reducing spectral resolution (Wei et al., 2017). The attractive multiplexing ability achievable with a vibrational dye pallet has been demonstrated in a conventional point scanning CARS microscope. The sensitivity and detection limits of these dyes in an SECARS configuration have yet to be determined and may allow a simplified imaging scheme for Raman dye labeled samples.

Future applications of both SECARS and Cofefe will certainly rely on the multifunctional nature of gold thin films. Correspondingly, improvements in the surface quality of gold films will be critical to fully realizing the potential of these methods.

Bibliography

Axelrod, Daniel (1981). "Cell-substrate Contacts Illuminated by Total-Internal Reflection Fluorescence". In: *Journal of Cell Biology* 89.9, pp. 141–145.

Axelrod, Daniel, Thomas P Burghardt, and Nancy L Thompson (1984). "Total internal reflection fluorescence". In: *Ann. Rev. Biophys. Bioeng.* 13, pp. 764–774.

Benninger, Richard K. P. and David W. Piston (2013). *Two-Photon Excitation Microscopy for the Study of Living Cells and Tissues*. Vol. Unit 4.11, pp. 1–36.

Beversluis, Michael, Alexandre Bouhelier, and Lukas Novotny (2003). "Continuum generation from single gold nanostructures through near-field mediated intraband transitions". In: *Physical Review B - Condensed Matter and Materials Physics* 68.11, pp. 1–10.

Bharadwaj, Palash, Alexandre Bouhelier, and Lukas Novotny (2011). "Electrical excitation of surface plasmons". In: *Physical Review Letters* 106.22, pp. 1–4.

Boozer, Christina et al. (2006). "Looking towards label-free biomolecular interaction analysis in a high-throughput format: a review of new surface plasmon resonance technologies". In: *Curr. Opin. Biotechnol.* 17.4, pp. 400–405.

Borejdo, J et al. (2006). "Fluorescence correlation spectroscopy in surface plasmon coupled emission microscope". In: *Opt. Express* 14.17, pp. 7878–7888.

Boyd, G T, Z H Lu, and Y R Shen (1986). "Photoinduced luminescence from the noble metals and its enhancement on roughened surfaces". In: *Phys. Rev. B* 33, pp. 7923–7936.

Brockman, Jennifer M, Bryce P Nelson, and Robert M Corn (2000). "Surface plasmon resonance imaging measurements of ultrathin organic films". In: *Annual review of physical chemistry* 51.1, pp. 41–63.

Cao, S et al. (2012). "Surface plasmon-coupled emission: what can directional fluorescence bring to the analytical sciences?" In: *Annu. Rev. Phys. Chem.* 5, pp. 317–336.

Cao, S H et al. (2014). "Label-free aptasensor based on ultrathin-linker-mediated hot-spot assembly to induce strong directional fluorescence". In: *J. Am. Chem. Soc.* 136.(19), pp. 6802–6805.

Cao, S.-H. et al. (2017). "Surface Plasmon-Coupled Emission". In: *Surface Plasmon Enhanced, Coupled and Controlled Fluorescence*. Ed. by C D Geddes. John & Sons: Wiley.

Chen, C K et al. (1979). "Surface coherent anti-Stokes Raman spectroscopy". In: *Phys. Rev. Lett.* 43, pp. 946–949.

Cheng, J.-X. and X. S. Xie (2015). "Vibrational spectroscopic imaging of living systems: An emerging platform for biology and medicine". In: *Science* 350.6264, aaa8870–aaa8870.

Cheng, Ji-Xin, Andreas Volkmer, and X Sunney Xie (2002). "Theoretical and experimental characterization of coherent anti-Stokes Raman scattering microscopy". In: *JOSA B* 19.6, pp. 1363–1375.

Cheng, Ji-Xin et al. (2002a). "Laser-sanning coherent anti-Stokes Raman scattering microscopy and applications to cell biology". In: *Biophys. J.* 83, pp. 502–509.

Cheng, Ji-xin et al. (2002b). "Multiplex Coherent Anti-Stokes Raman Scattering Microspectroscopy and Study of Lipid Vesicles". In: *J. Phys. Chem. B* 106.34, pp. 8493–8498.

Chiu, Kuo-Chih et al. (2011). "Optimizing silver film for surface plasmon-coupled emission induced two-photon excited fluorescence imaging". In: *Optics Express* 19.6, p. 5386.

Cullis, A G and L T Canham (1991). "Visible light emission due to quantum size effects in highly porous crystalline silicon". In: *Nature* 353, pp. 335–338.

Dieringer, Jon A et al. (2007). "A Frequency Domain Existence Proof of Single-Molecule Surface-Enhanced Raman Spectroscopy". In: *J. Am. Chem. Soc.* 129.51, pp. 16249–16256.

Doremus, Robert H. (1964). "Optical properties of small gold particles". In: *The Journal of Chemical Physics* 40.8, pp. 2389–2396.

Drezet, A. et al. (2008). "Leakage radiation microscopy of surface plasmon polaritons". In: *Materials Science and Engineering B: Solid-State Materials for Advanced Technology* 149.3, pp. 220–229.

Drezet, Aurélien and Cyriaque Genet (2013). "Imaging surface plasmons: from leaky waves to far-field radiation". In: *Physical review letters* 110.21, p. 213901.

Dubertret, B et al. (2002). ""In vivo imaging of quantum dots encapsulated in phospholipid micelles,"" in: *Science* 298, pp. 1759–1762.

Evans, Conor L et al. (2005). "Chemical imaging of tissue in vivo with video-rate coherent anti-Stokes Raman scattering microscopy." In: *Proceedings of the National Academy of Sciences of the United States of America* 102.46, pp. 16807–16812.

Fast, Alexander et al. (2016). "Surface-enhanced coherent anti-Stokes Raman imaging of lipids". In: *Appl. Opt.* 55.22, pp. 5994–6000.

Fontana, Eduardo (2006). "Thickness optimization of metal films for the development of surface-plasmon-based sensors for nonabsorbing media". In: *Applied optics* 45.29, pp. 7632–7642.

Giergiel, J et al. (1988). “Surface plasmon polariton enhancement of Raman scattering in a Kretschmann geometry”. In: *J. Phys. Chem.* 92.19, pp. 5357–5365.

Green, R J et al. (2000). “Surface plasmon resonance analysis of dynamic biological interactions with biomaterials”. In: *Biomaterials* 21.18, pp. 1823–1835.

Gryczynski, Ignacy et al. (2004). “Surface plasmon-coupled emission with gold films”. In: *J. Phys. Chem. B* 108.33, pp. 12568–12574.

Gryczynski, Ignacy et al. (2005). “Directional two-photon induced surface plasmon-coupled emission”. In: *Thin Solid Films* 491.1, pp. 173–176.

Gustafsson, N et al. (2016). “Fast live-cell conventional fluorophore nanoscopy with ImageJ through super-resolution radial fluctuations”. In: *Nat Comm.* 7, p. 12471.

Halpern, Aaron R et al. (2014). “Single-nanoparticle near-infrared surface plasmon resonance microscopy for real-time measurements of DNA hybridization adsorption”. In: *ACS Nano* 8, pp. 1022–1030.

He, Ruei-Yu et al. (2009). “Surface plasmon-enhanced two-photon fluorescence microscopy for live cell membrane imaging”. In: *Opt. Express* 17.8, pp. 5987–5997.

Hecht, B et al. (1996). “Local excitation, scattering, and interference of surface plasmons”. In: *Phys. Rev. Lett.* 77.9, p. 1889.

Hohenau, A. et al. (2011). “Surface plasmon leakage radiation microscopy at the diffraction limit”. In: *Optics Express* 19.25, p. 25749.

Homola, J. (2008). “Surface plasmon resonance sensors for detection of chemical and biological species”. In: *Chemical reviews* 108.2, pp. 462–493.

Homola, Jiřı′, Sinclair S Yee, and Günter Gauglitz (1999). “Surface plasmon resonance sensors”. In: *Sensors and Actuators B: Chemical* 54.1-2, pp. 3–15.

Hu, Chun-Rui et al. (2013). “Stimulated Raman scattering imaging by continuous-wave laser excitation”. In: *Optics Letters* 38.9, p. 1479.

Huang, Bo, Fang Yu, and Richard N Zare (2007). "Surface Plasmon Resonance Imaging Using a High Numerical Aperture Microscope Objective". In: *Anal. Chem.* 79.7, pp. 2979–2983.

Inoue', Shinya (1953). "Polarization optical studies of the mitotic spindle". In: *Chromosoma* 5.1, pp. 487–500.

Jacques, Steven L. (2013). "Optical properties of biological tissues: A review". In: *Physics in Medicine and Biology* 58.11.

Jeanmaire, David L and Richard P Van Duyne (1977). "Surface raman spectroelectrochemistry". In: *J. Electroanal. Chem. Interfacial Electrochem.* 84.1, pp. 1–20.

Johnson, P. B. and R. W. Christy (1972a). "Optical constants of the noble metals". In: *Physical Review B* 6.12, pp. 4370–4379.

Johnson, Peter B and R-$W_{Christy}$ (1972b). "Optical constants of the noble metals". In: *Phys. Rev. B* 6.12, p. 4370.

Jordan, Claire E et al. (1997). "Surface plasmon resonance imaging measurements of DNA hybridization adsorption and streptavidin/DNA multilayer formation at chemically modified gold surfaces". In: *Analytical Chemistry* 69.24, pp. 4939–4947.

Kano, Hiroshi and Wolfgang Knoll (2000). "A scanning microscope employing localized surface-plasmon-polaritons as a sensing probe". In: *Optics Communications* 182.1-3, pp. 11–15.

Kenison, J P et al. (2017). "Imaging properties of surface-enhanced coherent anti-Stokes Raman scattering microscopy on thin gold films". In: *J. Opt Soc. Am. B* 34.(10), pp. 2104–2114.

Kneipp, Katrin et al. (1997). "Single Molecule Detection Using Surface-Enhanced Raman Scattering (SERS)". In: *Phys. Rev. Lett.* 78.9, pp. 1667–1670.

Kooyman, R P H et al. (1988). “Surface plasmon resonance immunosensors: sensitivity considerations”. In: *Anal. Chim. Acta* 213, pp. 35–45.

Kossoy, Anna et al. (2014). “Optical and structural properties of ultra-thin gold films”. In: *Advanced Optical Materials* 3.1, pp. 71–77.

Kreibig, U. (1977). “Anomalous Frequency and Temperature Dependence of the Optical Absorption of Small Gold Particles”. In: *J. Phys. Colloques* 38.C2, pp. 97–103.

Krishnamachari, Vishnu Vardhan and Eric Olaf Potma (2007). “Focus-engineered coherent anti-Stokes Raman scattering microscopy: a numerical investigation”. In: *J. Opt. Soc. Am. A* 24.4, pp. 1138–1147.

Kuhlicke, Alexander et al. (2013). “In situ observation of plasmon tuning in a single gold nanoparticle during controlled melting”. In: *Nano Letters* 13.5, pp. 2041–2046.

Lakowicz, Joseph R et al. (2003). “Directional surface plasmon-coupled emission: a new method for high sensitivity detection”. In: *Biochem. Biophys. Res. Commun.* 307.3, pp. 435–439.

Le Ru, E. C. et al. (2007). “Surface enhanced raman scattering enhancement factors: A comprehensive study”. In: *Journal of Physical Chemistry C* 37, pp. 13794–13803.

Li, Haibo et al. (2012). “Directional emission of surface-enhanced Raman scattering based on a planar-film plasmonic antenna”. In: *Thin Solid Films* 520.18, pp. 6001–6006.

Li, Tao et al. (2017). “Revealing the Mechanism of Photoluminescence from Single Gold Nanospheres by Defocused Imaging”. In: *ACS Photonics* 8, pp. 2003–2010.

Lieb, M Andreas, James M Zavislan, and Lukas Novotny (2004). “Single-molecule orientations determined by direct emission pattern imaging”. In: *J. Opt. Soc. Am. B* 21.6, pp. 1210–1215.

Lin, Chun-Yu et al. (2010). “Surface plasmon-enhanced and quenched two-photon excited fluorescence”. In: *Opt. Express* 18.12, pp. 12807–12817.

Link, Stephan and Mostafa A. El-Sayed (1999). "Size and Temperature Dependence of the Plasmon Absorption of Colloidal Gold Nanoparticles". In: *The Journal of Physical Chemistry B* 103.21, pp. 4212–4217.

Liu, Xuejun, Yong Wang, and Eric Olaf Potma (2011). "Surface-mediated four-wave mixing of nanostructures with counterpropagating surface plasmon polaritons". In: *Optics letters* 36.12, pp. 2348–2350.

Loebich, Otto (1972). "The optical properties of gold". In: *Gold Bulletin* 5, pp. 2–10.

Maley, Adam M et al. (2017). "Characterizing single polymeric and protein nanoparticles with surface plasmon resonance imaging measurements". In: *ACS nano* 11.7, pp. 7447–7456.

Matsubara, K, S Kawata, and S Minami (1988). "A compact surface plasmon resonance sensor for measurement of water in process". In: *Applied spectroscopy* 42.8, pp. 1375–1379.

Meyer, Stefan A, Eric C Le Ru, and Pablo G Etchegoin (2011). "Combining Surface Plasmon Resonance (SPR) Spectroscopy with Surface-Enhanced Raman Scattering (SERS)". In: *Anal. Chem.* 83.6, pp. 2337–2344.

Meyer, Stefan A et al. (2012). "Combined SPR and SERS Microscopy in the Kretschmann Configuration". In: *J. Phys. Chem. A* 116.3, pp. 1000–1007.

Mooradian, A. (1969). "Photoluminescence of metals". In: *Physical Review Letters* 22.5, pp. 185–187.

Nie, Shuming and Steven R Emory (1997). "Probing Single Molecules and Single Nanoparticles by Surface-Enhanced Raman Scattering". In: *Science* 275.5303, pp. 1102–1106.

Novotny, Lukas (1997). "Allowed and forbidden light in near-field optics. I. A single dipolar light source". In: *J. Opt. Soc. Am. A* 14.1, pp. 91–104.

Novotny, Lukas and Bert Hecht (2012). *Principles of nano-optics*. Cambridge university press.

Olmon, Robert L. et al. (2012). "Optical dielectric function of gold". In: *Physical Review B - Condensed Matter and Materials Physics* 86.23, pp. 1–9.

Owyoung, Adelbert and Eric D. Jones (1977). "Stimulated Raman spectroscopy using low-power cw lasers". In: *Optics Letters* 1.5, p. 152.

Phillips, K Scott and Quan Cheng (2007). "Recent advances in surface plasmon resonance based techniques for bioanalysis". In: *Analytical and bioanalytical chemistry* 387.5, pp. 1831–1840.

Potma, Eric and X Sunney Xie (2003). "Detection of single lipid bilayers with coherent anti-Stokes Raman scattering (CARS) microscopy". In: *J. Raman Spectrosc.* 34, pp. 642–650.

Potma, Eric O, Wim P De Boeij, and Douwe A Wiersma (2000). "Nonlinear coherent four-wave mixing in optical microscopy". In: *J. Opt. Soc. Am. B* 17.10, pp. 1678–1684.

Raether, H (1977). "Surface plasma oscillations and their applications". In: *Physics of Thin Films*. Ed. by G Hass, M Francombe, and R Hoffman. Academic.

Saar, Brian G et al. (2010). "Video-Rate Molecular Imaging in Vivo with Stimulated Raman Scattering". In: *Science* 330.6009, pp. 1368–1370.

Schatz, G C (1984). "Theoretical studies of surface enhanced Raman scattering". In: *Acc. Chem. Res.* 17, pp. 370–376.

Schmidt, W. J. (1939). "Doppelbrechung der Kernspindel und Zugfasertheorie der Chromosomenbewegung". In: *Chromosoma* 1.1, pp. 253–264.

Shegai, Timur et al. (2011). "Unidirectional broadband light emission from supported plasmonic nanowires". In: *Nano Lett.* 11.2, pp. 706–711.

Smolyaninov, Igor I et al. (1997). "Experimental study of surface-plasmon scattering by individual surface defects". In: *Phys. Rev. B* 56.3, p. 1601.

Stefani, F D et al. (2005). "Surface-Plasmon-Mediated Single-Molecule Fluorescence Through a Thin Metallic Film". In: *Phys. Rev. Lett.* 94.2, p. 23005.

Steuwe, Christian et al. (2011). "Surface enhanced coherent anti-Stokes Raman scattering on nanostructured gold surfaces". In: *Nano Lett.* 11, pp. 5339–5343.

Su, Yen Hsun et al. (2010). "Influence of surface plasmon resonance on the emission intermittency of photoluminescence from gold nano-sea-urchins". In: *Nanoscale* 2.12, pp. 2639–2646.

Syal, Karan et al. (2015). "Antimicrobial susceptibility test with plasmonic imaging and tracking of single bacterial motions on nanometer scale". In: *ACS nano* 10.1, pp. 845–852.

Tang, Wanyi et al. (2018). "Investigation on the optimal wavelength for two-photon microscopy in brain tissue". In: *AIP Advances* 8.6.

Trache, Andreea and Gerald A Meininger (2005). "Total Internal Reflection Fluorescence (TIRF) Microscopy". In: *Current Protocols in Microbiology*. John Wiley & Sons, Inc.

Wang, Shaopeng et al. (2010). "Label-free imaging, detection, and mass measurement of single viruses by surface plasmon resonance". In: *Proceedings of the National Academy of Sciences* 107.37, pp. 16028–16032.

Wang, Yong et al. (2012). "Wide-field, surface-sensitive four-wave mixing microscopy of nanostructures". In: *Appl. Opt.* 51, pp. 3305–3312.

Wei, Lu et al. (2017). "Super-multiplex vibrational imaging". In: *Nature* 544.7651, p. 465.

Weichert, F et al. (2010). “Signal analysis and classification for surface plasmon assisted microscopy of nanoobjects”. In: *Sensors and Actuators B: Chemical* 151.1, pp. 281–290.

Wilson, W L, P F Szajowski, and L E Brus (1993). “Quantum confinement in size-selected, surface-oxidized silicon nanocrystals”. In: *Science* 262, pp. 1242–1244.

Yoo, Hae-Wook et al. (2012). “Surface plasmon polariton Raman microscopy”. In: *Vib. Spectrosc.* 60, pp. 85–91.

Yu, Hui et al. (2014). “Plasmonic imaging and detection of single DNA molecules”. In: *ACS nano* 8.4, pp. 3427–3433.

Yu, Hui et al. (2017). “Achieving high spatial resolution surface plasmon resonance microscopy with image reconstruction”. In: *Analytical chemistry* 89.5, pp. 2704–2707.

Yuan, C T et al. (2016). “Single fluorescent gold nanoclusters”. In: 17.18, pp. 747–749.

Zayats, Anatoly V., Igor I. Smolyaninov, and Alexei A. Maradudin (2005). “Nano-optics of surface plasmon polaritons”. In: *Physics Reports* 408.3-4, pp. 131–314.

Zerulla, D et al. (2003). “Sensing molecular properties by ATR-SPP Raman spectroscopy on electrochemically structured sensor chips”. In: *Electrochim. Acta* 48.20, pp. 2943–2947.

Zhang, L M and D Uttamchandani (1988). “Optical chemical sensing employing surface plasmon resonance”. In: *Electronics Letters* 24.23, pp. 1469–1470.